THE DEVELOPMENT AND TEST OF A DEFORMABLE DIFFRACTION GRATING FOR A STIGMATIC EUV SPECTROHELIOMETER

J. Gethyn Timothy
Principal Investigator
Center for Space Science and Astrophysics
Stanfor University, ERL 314
Stanford, CA 94305-4055

Co-Investigator:

Prof. A.B.C. Walker, Jr.
Center for Space Science and Astrophysics

Associate Investigator:

Dr. J. S. Morgan
Center for Space Science and Astrophysics

Collaborating Investigators:

Prof. M.C.E. Huber
Space Science Department ESA

Prof. G. Tondello
University of Padua

TABLE OF CONTENTS

Page

I. Introduction

In 1981 a proposal was submitted to the NASA Solar Physics Office for a study of the dynamics of the fine-scale structure of the solar outer atmosphere using a high-resolution stigmatic extreme-ultraviolet (EUV) spectroheliometer. The scientific objectives of the program are to address currently unanswered fundamental questions concerning the fine-scale structure of the chromosphere, transition region, and corona. The unique characteristics of the spectroheliometer will be utilized in combination with plasma-diagnostic techniques to study the temperature, density, and velocity structures of specific features in the solar outer atmosphere. The goal is to seek a unified understanding of the interplay between the time-dependent geometry of the magnetic field structure and the associated flows of mass and energy, the key to which lies in the smallest spatial scales that are unobservable with current EUV instruments (see, for example, the review by Parker, 1985 and references therein, and papers by Doschek and others in NASA Conference Publication 2483, 1986).

In order to study these phenomena, we proposed to construct a high-resolution stigmatic EUV spectroheliometer employing a toroidal diffraction grating fabricated using deformable optics, and a state-of-the art pulse-counting imaging photoelectric detector system. The EUV spectroheliometer is designed to provide images and high-resolution spectra over the wavelength range from 300 to 1200 Å with a spatial resolution of better than 1 arcsec, a spectral resolution of the order of 0.08 Å, and the capability to centroid spectral features to an accuracy of better than 0.002 Å (0.04 pixels). A spatial field of the order of 0.4×180 (arcsec)^2 and a spectral range of 110 Å can be monitored simultaneously with these spatial and spectral resolutions.

The proposal to construct the EUV spectroheliometer was not accepted by NASA until 1989 because of funding limitations. However, funding was provided under the NASA Supporting Research and Technology (SRT) program to initiate the fabrication of the toroidal diffraction grating using the elastically-deformable substrate technique. This final report describes the results of the toroidal grating development program which was funded initially at the University of Colorado under NASA SRT Grant NAGW-396 and, following the transfer of the Principal Investigator to Stanford University, under NASA SRT Grant NAGW-540. The evaluations of the toroidal gratings and the construction of the EUV spectroheliometer are continuing under NASA Grant NAG5-664.

II. Results of the Development Program

The SRT funding to support the detailed evaluation of the imaging characteristics of the toroidal diffraction grating enabled a number of tasks to be undertaken as the key initial steps in the fabrication of the EUV spectroheliometer.

A 3600 grooves mm^{-1} spherical master grating with a radius-of-curvature of 1 m was procured from Hyperfine Inc., Boulder, CO by the investigator at the Federal Technical University (ETH), Zürich, Switzerland. This grating was successfully replicated onto a deformable concave blank, and a fixed toroidal grating was replicated using the deformable sub-master grating. Two additional replica gratings were procured under this grant. A laboratory spectrograph designed to accommodate these toroidal replica gratings was fabricated at the University of Padua. In parallel with this activity, a number of sealed and open-structure Multi-Anode Microchannel Array (MAMA) detector systems were fabricated at Stanford University (see Timothy, 1991 and 1992 attached to this report).

The initial photographic tests of the first toroidal replica grating were completed in 1984. Densitometer measurements of these photographic images showed that the spatial variation of the blur dimensions was essentially in agreement with that predicted from the ray trace analyses (Huber and Tondello, 1979). In order to provide more accurate data on the imaging properties of the toroidal grating, a (256 x 1024)-pixel visible-light MAMA detector system was shipped to the University of Padua in July 1985 for the first photoelectric tests of the grating. In a successful one-week test program images were recorded at the wavelength of the He I resonance line at 584 Å. The results of these tests and descriptions of the spectrometer configuration and the grating fabrication technique are given in the publications (Huber *et al.*, 1986 and 1988a) attached to this report.

A second two-week test program was undertaken at the University of Padua in September 1988 utilizing a new laboratory spectrograph and, for the first time, an open-structure (256 x 1024)-pixel MAMA detector system. The configuration of the laboratory system is shown in Figure 1. The light source was a DC hollow-cathode discharge which produced emission-line spectra; He, Ne and Ar were used as the source gases for the initial tests. A set of ten pinholes spaced along the entrance slit was used to provide spatial information at right angles to the plane of dispersion. The (256 x 1024)-pixel open-structure MAMA detector had pixel dimensions of 25 x 25 microns^2 and the MCP glass was used as the EUV photocathode.
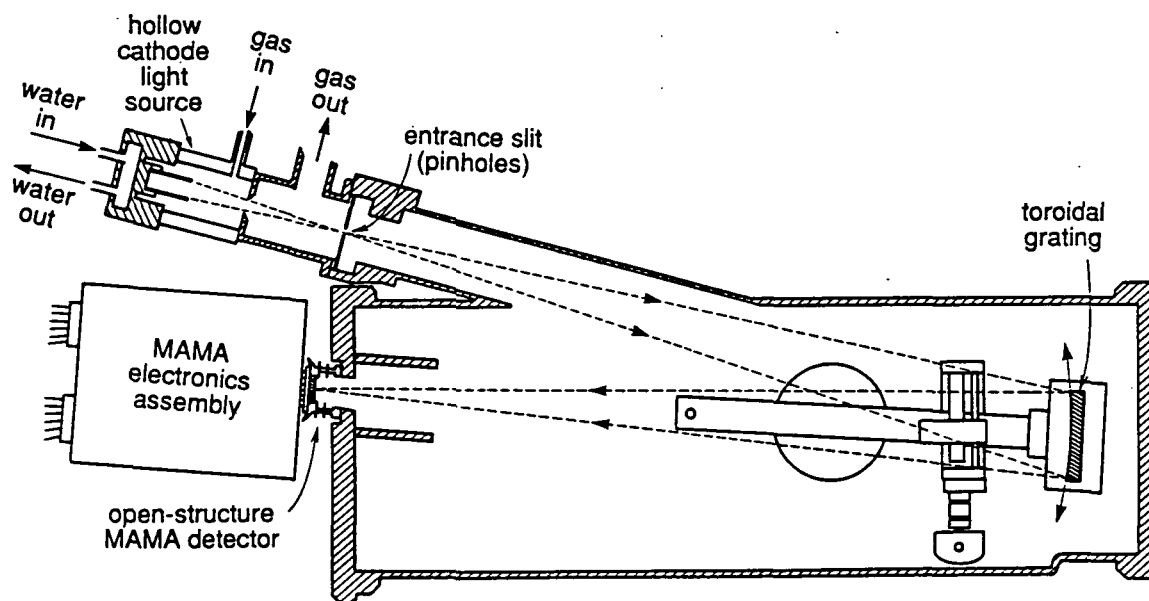

Figure 1. Configuration of the laboratory system for tests of the imaging properties of the toroidal grating at EUV wavelengths.

The data from these tests were analyzed in detail and a summary of the results is given in the paper (Morgan *et al.*, 1991) attached to this report. As an example of the type of data recorded during these tests, a spatially resolved spectrum of Ne at wavelengths near 600 Å is shown in Figure 2. A spatial cut through the pinholes at the wavelength of a single

emission line is shown in Figure 3(a) and the Ne emission line spectrum is shown in Figure 3(b).
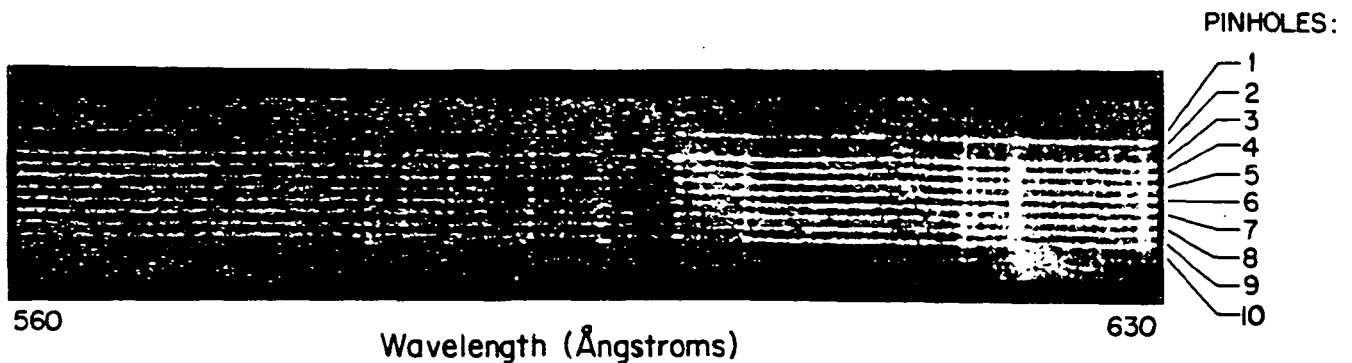

Figure 2. A 1000 second exposure of the Ne I spectrum. The spectrograph entrance aperture consisted of 10 equi-spaced pinholes. Each horizontal stripe is the Ne I spectrum imaged through a single pinhole. The dispersion runs in the horizontal direction; wavelength increases from left to right starting at about 560 Å and ending near 630 Å. The second pinhole from the top was blocked at the time of this exposure. The intensity function table has been set to enhance the faint scattered-light continuum.

Further measurements of the 3600 grooves mm^{-1} grating with an intensified CCD detector system were undertaken in Padua in 1990 in an attempt to arrive more closely at the exact stigmatic focus. The elegant results of these tests are described in the paper by Huber et al., 1991, attached to this report.

In order to obtain good image quality with optical systems faster than f/15, or at large angles of incidence, correction for coma is required. A more complex deformable substrate for the fabrication of aspheric gratings with coma correction has been procured. We have carried out initial laboratory tests of this substrate and have shown that it can be deformed into a toroidal form and also to induce coma. The substrate is now at Hyperfine, Inc., Boulder, CO., where the fabrication of the first aspheric grating is about to start. As discussed in the paper (Huber et al., 1988b) attached to this report, the elastic-deformation technique offers the potential for significant advantages over other techniques for fabricating aspheric surfaces in that slope errors are kept to a minimum. This technique is thus not only of major interest for solar instruments but also for instruments on other space astrophysics missions such as the Far Ultraviolet Spectroscopic Explorer (FUSE).

The initial evaluations of a toroidal replica grating with a focal ratio of f/8 fabricated using an elastically-deformable substrate were started at Padua in 1991 as the first stage of a program to develop fast coma-corrected toroidal gratings for use in space astrophysics experiments. The results of these tests, described in Huber et al., 1991, showed that the effects of coma appeared to be significantly less than predicted by the ray trace results. The reasons for this are still not clear, and these investigations are still in progress.
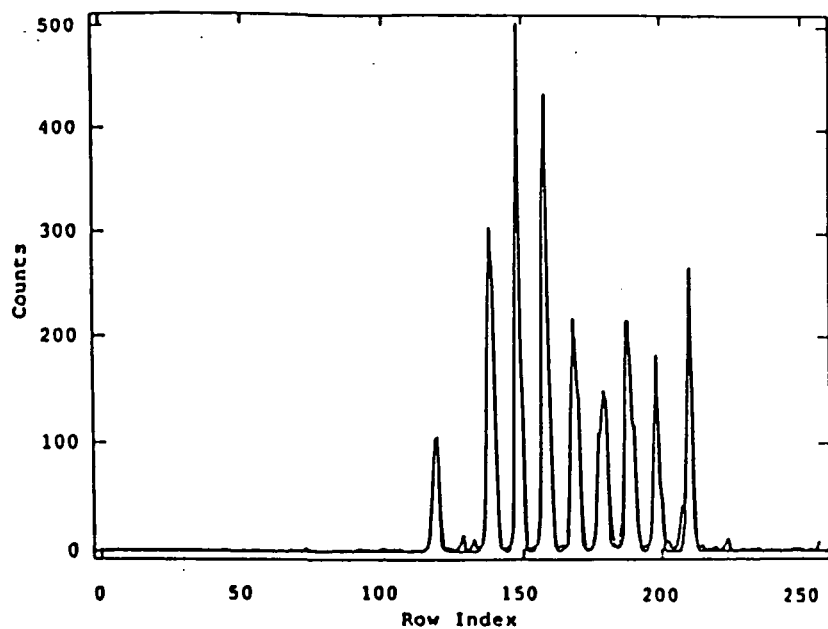
(a)
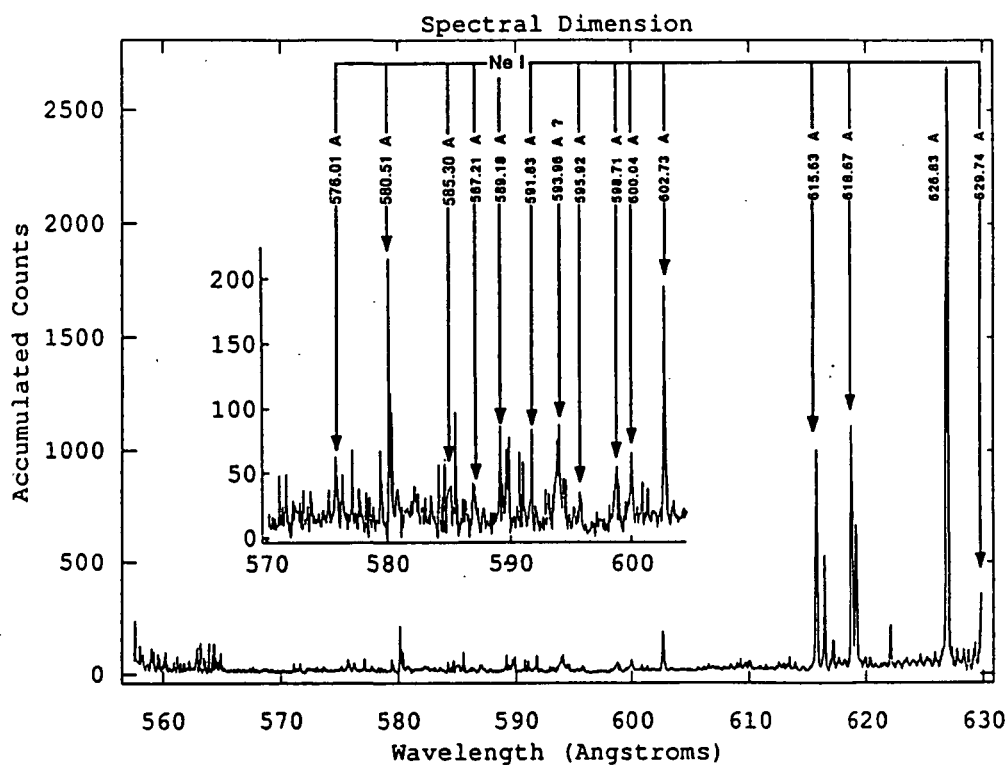
(b)

Figure 3(a). A spatial cut through the pinholes at the wavelengths of the emission line at 626.83 Å. Pinhole 1, which is seen as the top-most horizontal stripe in Figure 2, is seen as the left-most peak in this plot. The dark line shows the data and the thin line shows the result of a least-squares Gaussian fit to the data.

(b). The spectrum obtained by averaging the bottom 4 pinholes shown in Figure 2. The inset shows the weak emission lines between 750 and 603 Å with an expanded scale. The lines labeled are not all of those that have been identified.

In 1991 a second model of the laboratory spectrograph was delivered from Padua to Stanford in order to, first, allow an extended series of studies of the toroidal gratings, and, second, to form the basis of the characterization facility for the MAMA detectors for the Solar Ultraviolet Measurements of Emitted Radiation (SUMER) and the Ultraviolet Coronagraph Spectrometer (UVCS) instruments for the ESA/NASA Solar and Heliospheric Observatory (SOHO) mission. This toroidal grating spectrograph provides a unique capability for studies of the performance characteristics of image-recording detector systems at EUV wavelengths, since the toroidal gratings can produce monochromatic point images with diameters of less than 20 microns. Construction of a detector characterization facility is now in progress with support from our NASA SOHO Contract NAS5-30387. The immediate task to be undertaken with this facility is the characterization of the SOHO MAMA detectors, which are optimized for studies at wavelengths between 400 Å and 1600 Å and have a format of 360 x 1024 pixels with pixel dimensions of 25 x 25 microns^2. A total of eight engineering model and flight model detector systems are being fabricated for the two SOHO instruments.. The characteristics to be determined include the point spread function (PSF) and the detective quantum efficiency (DQE) as functions of wavelength, the flat field uniformity, and the geometric fidelity.

In order to support the SOHO MAMA detector characterization program, two additional toroidal gratings were ordered from Hyperfine Inc. with a ruling density of 1800 grooves mm^{-1} (see Bergamini et al., 1992 attached to this report) These gratings were also fabricated using the elastically deformable substrates. A spectrum of the hollow cathode light source operating with a He-Ne gas mixture at wavelengths around 600 Å recorded with the 3600 grooves mm^{-1} toroidal grating is shown in Figure 4. An array of ten pinholes was mounted along the spectrometer entrance slit in order to determine the spatial image quality. These data were recorded with one of the SOHO breadboard MAMA detector systems. Some geometrical distortion can be seen in the image, caused by curvature non-uniformities in the curved-channel MCP in this detector system. The upper part of the image is attenuated by a 10% transmission mesh, designed to limit the signal from the strong H Ly α emission line during observations of solar active regions by the SUMER instrument. As the first step in the characterization program for the SOHO MAMA detector systems, both the 3600 grooves mm^{-1} and the 1800 grooves mm^{-1} toroidal gratings have been used to test the quality of the images recorded through the mesh, as shown in Figure 5. The characterization of the first engineering model SOHO detector will begin in May 1992.

As the last task in the SRT program, we completed the definition and initiated the detailed design of a high-resolution stigmatic EUV spectroheliometer which is compatible with flight on a Black Brant sounding rocket, and have now started fabrication of this instrument with support from NASA Grant NAG5-664. A detailed description of the instrument and the results of some of the optical ray traces are described in the papers (Timothy et al., 1991, Berger et al., 1991, 1992) attached to this report. The test results already obtained under the SRT program have shown that the toroidal diffraction gratings fabricated with the elastically-deformable substrate can meet the imaging and spectral resolution requirements for the f/15 optical system of this instrument. The first flight of this payload is scheduled for early 1993.
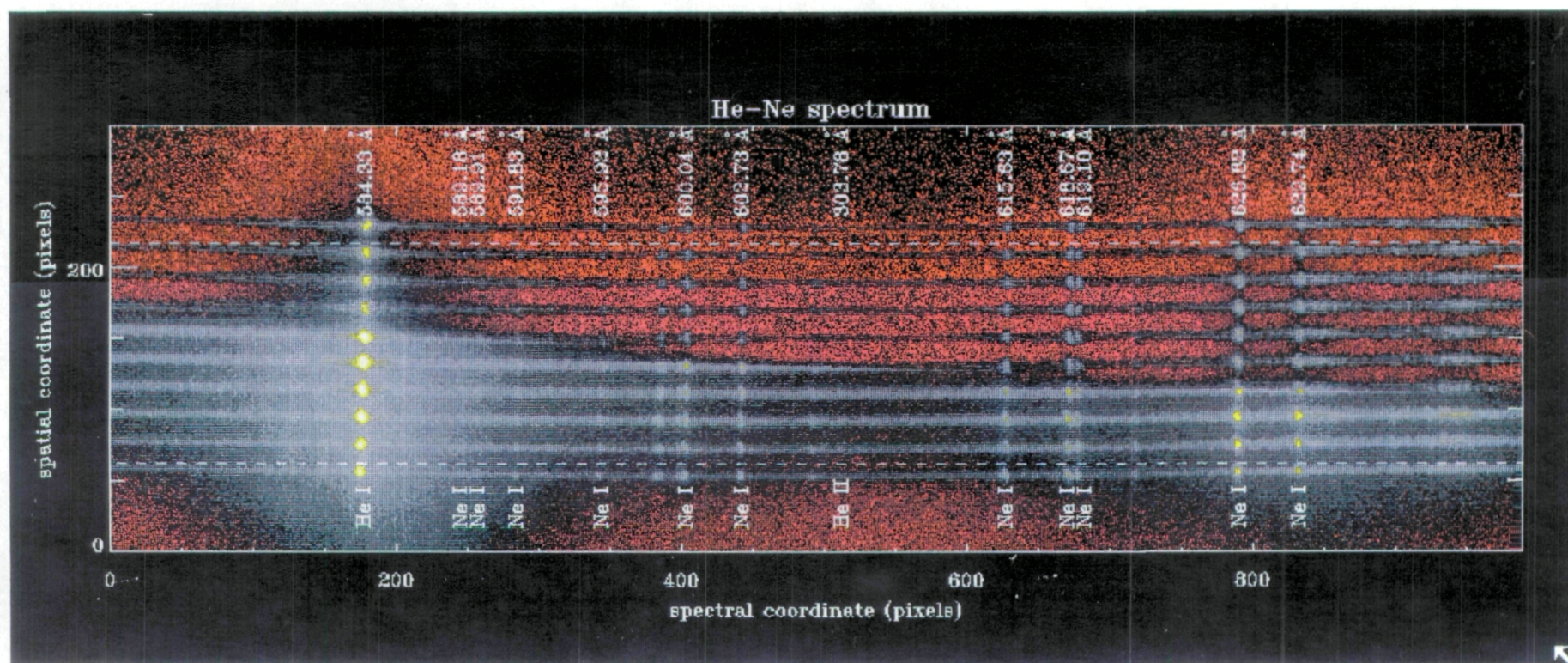
Figure 4. He-Ne spectrum recorded with 3600 grooves mm^{-1} toroidal grating and SOHO MAMA breadboard detector. A mesh with 10% transmission is over the top half of the detector. Geometrical distortion in the image is caused by the curved-channel MCP.
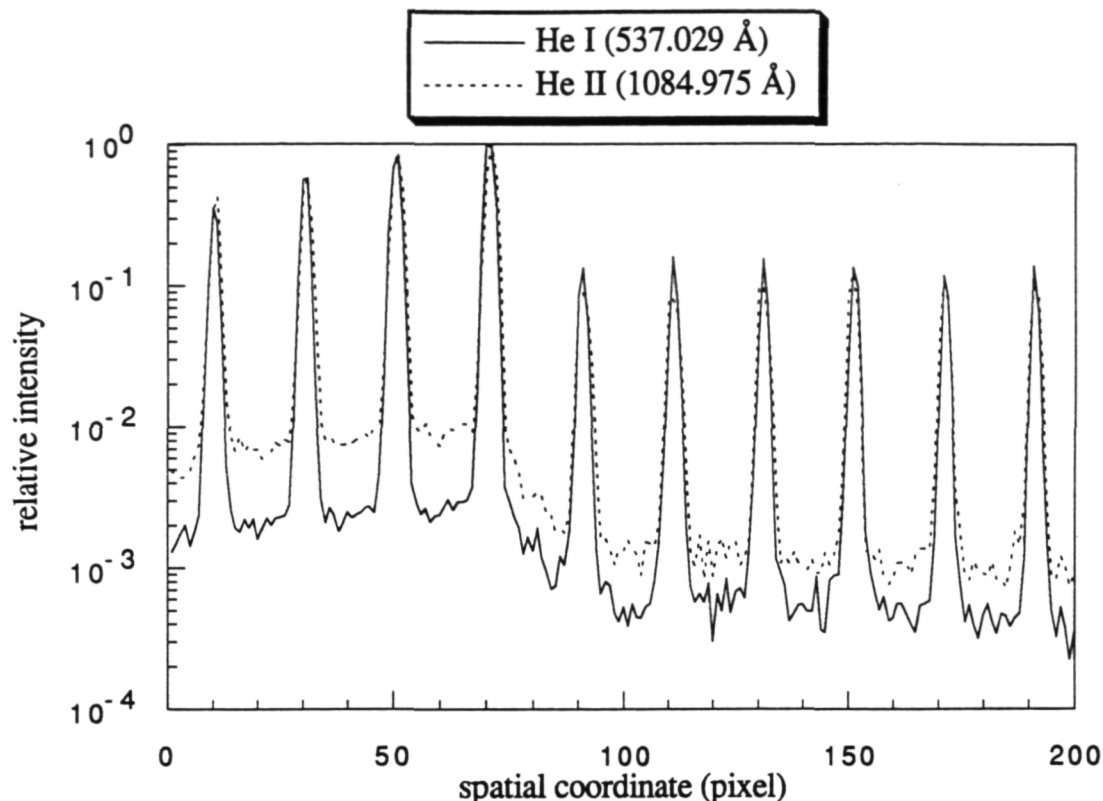
Figure 5. Images of the pinholes along the entrance slit of the toroidal grating spectrometer recorded directly and through the 10% transmission mesh to be used as an attenuator in the SUMER MAMA detector.

III. Summary

Under this grant we have successfully undertaken the following tasks:

1. Fabricated and tested toroidal diffraction gratings by a new technique employing an elastically-deformable substrate. Toroidal diffraction gratings fabricated by this method will be used in the UVCS and the Coronal Diagnostics Spectrometer (CDS) instruments on the SOHO mission.

2. Procured and tested the toroidal diffraction gratings to be used for the evaluation of the MAMA detector systems for the SUMER and UVCS instruments on the SOHO mission.

3. Initiated the fabrications of fast (f/8) toroidal, and coma-corrected toroidal diffraction gratings using elastically-deformable substrates.

4. Completed the detailed design of the High-Resolution Extreme-ultraviolet Spectroheliometer (HiRES) payload for flight on a Black Brant sounding rocket.

Further studies are continuing under NASA Grant NAG5-664 and NASA Contract NAS5-30387.

IV. References

Bergamini, P., T. E. Berger, G. Giaretta, M.C.E. Huber, G. Naletto, J. G. Timothy, and G. Tondello, An Imaging Extreme Ultraviolet Spectrometer, To be published in the proceedings of The Tenth International Colloquium of UV and X-ray Spectroscopy of Astrophysical and Laboratory Plasmas, Berkeley, CA, February 1992.

Berger, T.E., J. G. Timothy, A.B.C. Walker, Jr., H. Kirby, J. S. Morgan, S. K. Jain, A. K. Saxena, J. C. Bhattacharyya, M.C.E. Huber, G. Tondello, and G. Naletto, Design and Test of a High-Resolution EUV Spectroheliometer, SPIE Multilayer and Grazing Incidence X-Ray, Vol. 1546, pp. 446-460, 1991.

Berger, T. E., P. Bergamini, H. Kirby, J. G. Timothy, A.B.C. Walker, Jr., J. C. Bhattacharyya, S. K. Jain, A. K. Saxena, M.C.E. Huber, G. Naletto, and G. Tondello, HiRES: High Resolution Extreme Ultraviolet Spectroheliometer, To be published in the proceedings of The Tenth International Colloquium of UV and X-ray Spectroscopy of Astrophysical and Laboratory Plasmas, Berkeley, CA, February 1992.

Doschek, G. A., Theoretical Problems in High Resolution Solar Physics II, NASA, Vol. 2483, pp. 37, 1986.

Huber, M.C.E. and G. Tondello, Applied Optics, Vol. 18, pp. 3948, 1979.

Huber, M.C.E., J. G. Timothy, J. S. Morgan, G. Lemaître, G. Tondello, M. E. Puiatti and P. Scarin, An Imaging Extreme Ultraviolet Spectrometer for Astrophysical Investigations in Space, SPIE Instrumentation in Astronomy VI, Vol. 627, pp. 363-370, 1986.

Huber, M.C.E., J. G. Timothy, J. S. Morgan, G. Lemaître, G. Tondello, E. Jannitti, and P. Scarin, Imaging extreme ultraviolet spectrometer employing a single toroidal diffraction grating: the initial evaluation, Applied Optics, Vol. 27, No. 16, pp. 3503-3510, August 1988 (a).

Huber, M.C.E., G. Lemaître, G. Naletto, P. Nicolosi, G. Tondello, E. Jannitti, J. S. Morgan and J. G. Timothy, Evaluation of Toroidal gratings in the EUV, SPIE X-Ray Instrumentation in Astronomy II, Vol. 982, pp. 372-379, August 1988 (b).

Huber, M.C.E., J. G. Timothy, J. S. Morgan, G. Lemaître, G. Tondello, and G. Naletto, The fabrication of toroidal and coma-corrected toroidal diffraction gratings from spherical master gratings using elastically deformable substrates: a progress report, SPIE Space Astronomical Telescopes and Instruments, Vol. 1494, pp. 472-480, 1991.

Morgan, J. S., J. G. Timothy, D. C. Slater, M.C.E. Huber, G. Tondello, E. Jannitti, G. Naletto, P. Nicolosi, and G. Lemaître, A high efficiency imaging extreme ultraviolet spectrometer, Extreme Ultraviolet Astronomy, edited by R.F. Malina and S. Bowyer, Pergamon Press, New York, pp. 380-389, 1991.

Parker, E. N., Solar Physics, Vol. 100, pp. 599, 1985.

Timothy, J. G., Performance Characteristics of the Imaging MAMA Detector Systems for SOHO, STIS, and FUSE/Lyman, SPIE EUV, X-Ray, and Gamma-Ray Instrumentation for Astronomy II, Vol. 1549, pp. 221-233, 1991.

Timothy, J. G., T. E. Berger, J. S. Morgan, A.B.C. Walker, Jr., S. K. Jain, A. K. Saxena, J. C. Bhattacharyya, M.C.E. Huber, G. Tondello, and G. Naletto, HiRES: a high resolution stigmatic extreme ultraviolet spectroheliometer for studies of the fine-scale structure of the solar chromosphere, transition region, and corona, Optical Engineering, Vol **30**, No. 8, pp. 1142-1149, August 1991.

Timothy, J. G., Multi-anode microchannel array detector systems for space astrophysics missions, Photoelectronic Image Devices 1991, edited by B.L. Morgan, Institute of Physics Conference Series Number 121, pp. 49-56, New York, 1992.

V. Attachments

Performance Characteristics of the Imaging MAMA Detector Systems for SOHO, STIS, and FUSE/*Lyman*, J. G. Timothy, <u>SPIE EUV, X-Ray, and Gamma-Ray Instrumentation for Astronomy II</u>, Vol. **1549**, pp. 221-233, 1991.

Multi-anode microchannel array detector systems for space astrophysics missions, J. G. Timothy, <u>Photoelectronic Image Devices 1991</u>, edited by B. L. Morgan, Institute of Physics Conference Series Number 121, pp. 49-56, New York, 1992.

An Imaging Extreme Ultraviolet Spectrometer for Astrophysical Investigations in Space, M.C.E. Huber, J. G. Timothy, J. S. Morgan, G. Lemaître, G. Tondello, M. E. Puiatti and P. Scarin, <u>SPIE Instrumentation in Astronomy VI</u>, Vol. **627**, pp. 363-370, 1986.

Imaging extreme ultraviolet spectrometer employing a single toroidal diffraction grating: the initial evaluation, M.C.E. Huber, J. G. Timothy, J. S. Morgan, G. Lemaître, G. Tondello, E. Jannitti, and P. Scarin, <u>Applied Optics</u>, Vol. **27**, No. 16, pp. 3503-3510, August 1988 (b).

A high efficiency imaging extreme ultraviolet spectrometer, J. S. Morgan, J. G. Timothy, D. C. Slater, M.C.E. Huber, G. Tondello, E. Jannitti, G. Naletto, P. Nicolosi, and G. Lemaître, <u>Extreme Ultraviolet Astronomy</u>, edited by R.F. Malina and S. Bowyer, Pergamon Press, New York, pp. 380-389, 1991.

The fabrication of toroidal and coma-corrected toroidal diffraction gratings from spherical master gratings using elastically deformable substrates: a progress report, M.C.E. Huber,, J. G. Timothy, J. S. Morgan, G. Lemaître, G. Tondello, and G. Naletto, <u>SPIE Space Astronomical Telescopes and Instruments</u>, Vol. **1494**, pp. 472-480, 1991.

Evaluation of Toroidal gratings in the EUV, M.C.E. Huber, G. Lemaître, G. Naletto, P. Nicolosi, G. Tondello, E. Jannitti, J. S. Morgan and J. G. Timothy, <u>SPIE X-Ray Instrumentation in Astronomy II</u>, Vol. **982**, pp. 372-379, August 1988 (a).

HiRES: a high resolution stigmatic extreme ultraviolet spectroheliometer for studies of the fine-scale structure of the solar chromosphere, transition region, and corona, J. G. Timothy, T. E. Berger, J. S. Morgan, A.B.C. Walker, Jr., S. K. Jain, A. K. Saxena, J. C. Bhattacharyya, M.C.E. Huber, G. Tondello, and G. Naletto, <u>Optical Engineering</u>, Vol **30**, No. 8, pp. 1142-1149, August 1991.

Design and Test of a High-Resolution EUV Spectroheliometer, T. E. Berger, J. G. Timothy, A.B.C. Walker, Jr., H. Kirby, J. S. Morgan, S. K. Jain, A. K. Saxena, J. C. Bhattacharyya, M.C.E. Huber, G. Tondello, and G. Naletto, <u>SPIE Multilayer and Grazing Incidence X-Ray</u>, Vol. **1546**, pp. 446-460, 1991.

An Imaging Extreme Ultraviolet Spectrometer, P. Bergamini, T. E. Berger, G. Giaretta, M.C.E. Huber, G. Naletto, J. G. Timothy, and G. Tondello, <u>To be published in the proceedings of The Tenth International Colloquium of UV and X-ray Spectroscopy of Astrophysical and Laboratory Plasmas</u>, Berkeley, CA, February 1992.

HiRES: High Resolution Extreme Ultraviolet Spectroheliometer, T. Berger, P. Bergamini, H. Kirby, J. G. Timothy, A.B.C. Walker, Jr., J. C. Bhattacharyya, S. K. Jain, A. K. Saxena, M.C.E. Huber, G. Naletto, and G. Tondello, <u>To be published in the proceedings of The Tenth International Colloquium of UV and X-ray Spectroscopy of Astrophysical and Laboratory Plasmas</u>, Berkeley, CA, February 1992.

Performance Characteristics of the Imaging MAMA Detector Systems for SOHO, STIS, and FUSE/*Lyman*

J. Gethyn Timothy

Center for Space Science and Astrophysics
Stanford University, ERL 314
Stanford, California 94305 USA

ABSTRACT

Imaging Extreme Ultraviolet (EUV) Multi-Anode Microchannel Array (MAMA) detector systems with formats of 360 x 1024 pixels and pixel dimensions of 25 x 25 microns^2 are being fabricated and tested for flight in two instruments on the ESA/NASA Solar and Heliospheric Observatory (SOHO). In addition, very-large-format (1024 x 1024)- and (2048 x 2048)-pixel Far Ultraviolet (FUV) and EUV MAMA detectors with pixel dimensions of 25 x 25 microns^2 are being fabricated and tested for use in the NASA Goddard Space Flight Center's *Hubble* Space Telescope Imaging Spectrograph (STIS), a second-generation instrument scheduled for in-orbit installation in 1997. Finally, FUV MAMA detectors with formats of 224 x 960 pixels and pixel dimensions of 14 x 14 microns^2 are being evaluated as prototypes of the detector for the prime FUV spectrograph of the Far Ultraviolet Spectroscopic Explorer (FUSE/*Lyman*) mission. The configurations and performance characteristics of the different detector systems are described and the plans for further development of the Advanced Technology MAMA detector system discussed.

1. INTRODUCTION

We are currently fabricating and characterizing Multi-Anode Microchannel Array (MAMA) detector systems for use on a number of space ultraviolet astrophysics missions at far-ultraviolet (FUV) and extreme-ultraviolet (EUV) wavelengths between about 300 and 28 nm. Open, open with openable cover, and sealed, (360 x 1024)-pixel MAMA detector systems, with pixel dimensions of 25 x 25 microns^2 and MgF$_2$, KBr, and CsI photocathodes will be used in the Solar Ultraviolet Measurements of Emitted Radiation (SUMER)[1] and the Ultraviolet Coronagraph Spectrometer (UVCS)[2] instruments on the ESA/NASA Solar and Heliospheric Observatory (SOHO)[3], scheduled for launch in 1995. Prototype very-large-format (1024 x 1024)- and (2048 x 2048)-pixel MAMA detector systems, with pixel dimensions of 25 x 25 microns^2 and CsI and Cs$_2$Te photocathodes, are currently under test and in fabrication for the NASA Goddard Space Flight Center's *Hubble* Space Telescope Imaging Spectrograph (STIS),[4] a second-generation instrument scheduled for in-orbit installation in 1997. Proof-of-concept sealed and open (224 x 960)-pixel MAMA detector systems, with pixel dimensions of 14 x 14 microns^2, are also under test as part of the Far Ultraviolet Spectroscopic Explorer (FUSE/*Lyman*) Phase B study.[5]

The performance characteristics of these different detector systems are described in the following sections of this paper in the context of the scientific objectives of each of the instruments.

2. MAMA DETECTOR SYSTEM

Details of the construction and mode-of-operation of the MAMA detector system have recently been presented in the literature.[6,7] The components of a MAMA detector consist of, first, the tube assembly and, second, the associated analog and digital electronic circuits. The MAMA detector tube, which can be sealed with a window or used in an open-structure configuration, contains a single, high-gain, curved-channel microchannel plate (MCP) electron multiplier with the photocathode material deposited on, or mounted in proximity focus with the front surface. Electrodes are mounted in proximity focus with the output surface of the MCP to detect and measure the positions of the electron clouds generated by single photon events (see Figs. 1 and 2).
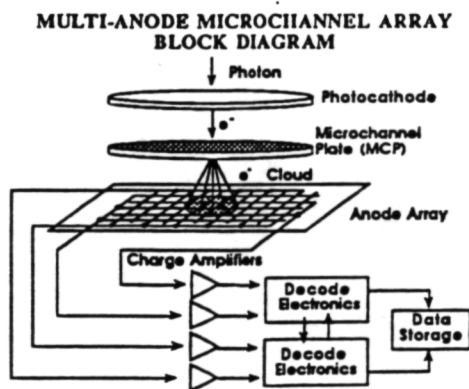

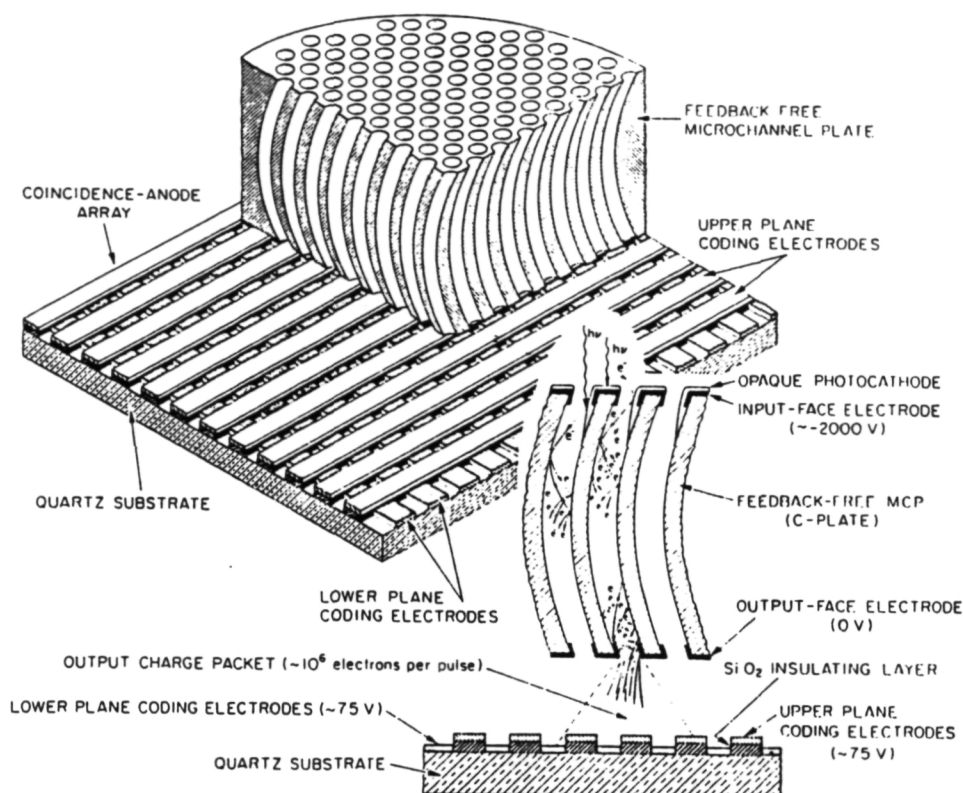Fig. 1. Schematic of the imaging MAMA detector system.

PRECEDING PAGE BLANK NOT FILMED

Fig. 2. Schematic showing details of the curved-channel MCP and the imaging multi-layer anode array used in the MAMA detector tubes.

The charge collected on the anode electrodes is amplified and shaped by high-speed amplifier and discriminator circuits.

Digital logic circuits respond to the simultaneous arrival of the shaped signals from several of these electrodes in each axis, which are arranged in groups to uniquely identify a x b pixels in one dimension with only a + b amplifier and discriminator circuits. For example, a total of 32 x 32, i.e. 1024, pixels in one dimension can be uniquely identified with 32 + 32, i.e. 64, amplifier and discriminator circuits. In the imaging MAMA detector tube, two arrays are mounted in tandem with orthogonal orientations, so that the positions of the detected photons can be sensed in two dimensions. In this configuration (a x b)^2 pixels can be uniquely identified with only 2 x (a + b) amplifier and discriminator circuits. Thus, a (1024 x 1024)-pixel array, for example, requires a total of only 128 amplifier and discriminator circuits. The two layers of anode electrodes in the imaging arrays are insulated from each other by a SiO$_2$ dielectric layer. The dielectric between the upper layer electrodes is etched away to allow the low energy (-30 eV) electrons in the charge cloud from the MCP to be collected simultaneously on both arrays. Details of the latest MAMA anode-array geometries and position-encoding algorithms can be found in the literature.[8-10]

3. SOHO MAMA DETECTOR SYSTEMS

The MAMA detectors for the SUMER and UVCS instruments on the SOHO mission have a high degree of commonality, but also significant differences dictated by the scientific needs of the two instruments. The definition of the detector systems has accordingly required a great deal of interaction between the MAMA detector development group, the SUMER instrument team at the Max-Planck-Institut für Aeronomie (MPAe), Katlenburg-Lindau, Germany, and the UVCS instrument team at the Smithsonian Astrophysical Observatory (SAO), Cambridge, MA. All of the detectors have formats of 360 x 1024 pixels and pixel dimensions of 25 x 25 microns^2. The other key parameters are listed in Table 1. The SUMER instrument is designed for spatially-resolved line-profile studies at wavelengths between about 40 and 160 nm. This instrument employs two MAMA detectors for redundancy. The prime detector is designed to be used in an open configuration and has a cover which can be opened on command after the instrument is under high vacuum in a test chamber or in the space environment. The purpose of the cover is to protect the photocathode materials and the high-gain MCP from contamination during the years of the instrument and spacecraft integration and test

Table 1. Key Parameters of the MAMA Detectors for the SUMER and UVCS Instruments on the SOHO Mission.

	SUMER		UVCS	
	Detector A	Detector B	Detector 1	Detector 2
Pixel Format	360 x 1024	360 x 1024	360 x 1024	360 x 1024
Pixel Dimensions	25 x 25 μm^2	25 x 25 μm^2	25 x 25 μm^2	25 x 25 μm^2
Anode Array Active Area	9.0 x 25.6 mm^2	9.0 x 25.6 mm^2	9.0 x 25.6 mm^2	9.0 x 25.6 mm^2
MCP Active Area	10 x 27 mm^2	10 x 27 mm^2	10 x 27 mm^2	10 x 27 mm^2
MCP Pore Size	12 microns	12 microns	12 microns	12 microns
Number of Amplifiers (including analog output)	105 (104+1)	105 (104+1)	105 (104+1)	105 (104+1)
Photocathode Material	MgF_2 and KBr	MgF_2 and KBr	CsI	KBr
Hybrid Amplifier and Discriminator	Yes	Yes	Yes	Yes
Gate Array Decode Circuits	Yes	Yes	Yes	Yes
Configuration	Openable cover	Open	Sealed	Openable cover

programs. The different subassemblies which make up the openable-cover detector system are shown in Fig. 3 and the detector system block diagram is shown in Fig. 4. The SOHO detector systems are being fabricated at our prime industrial contractor, Ball Electro-Optics and Cryogenics Division (BECD), Boulder, CO. The configuration of the photocathodes on the SUMER detector is shown in Fig. 5. Two photocathode materials are deposited on the front face of the curved-channel MCP: KBr for a high-quantum efficiency at wavelengths between 80 and 160 nm; and MgF_2 for both a high-quantum efficiency at wavelengths between 40 and 80 nm, and also to provide rejection of the strong H Ly α 121.6 nm radiation, since in SUMER the spectral lines at wavelengths below 80 nm are observed in second order. In addition, the detector has two 10% transparency nickel meshes mounted over a 30-pixel area at either end of the array to act as attenuators for the H Ly α 121.6 nm line, permitting this extremely strong emission line to be observed in active regions on the solar disk without saturating the detector system.

The back-up detector in the SUMER instrument (detector B) is open and does not have the openable cover in
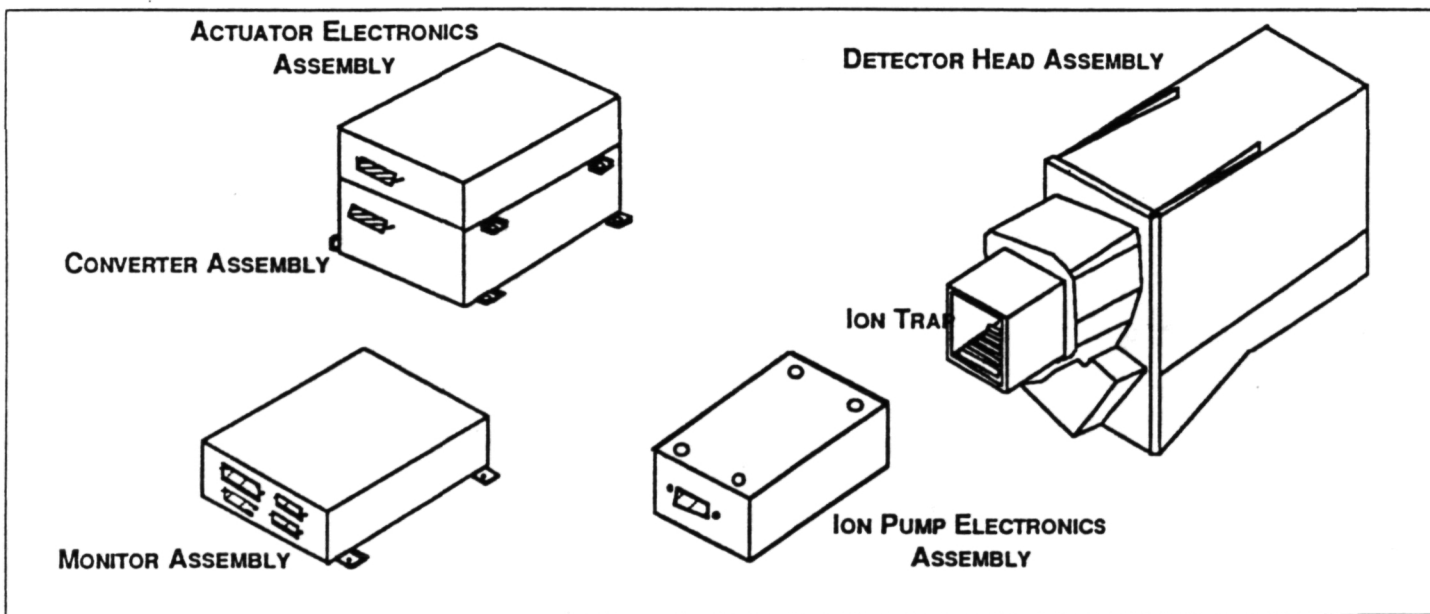

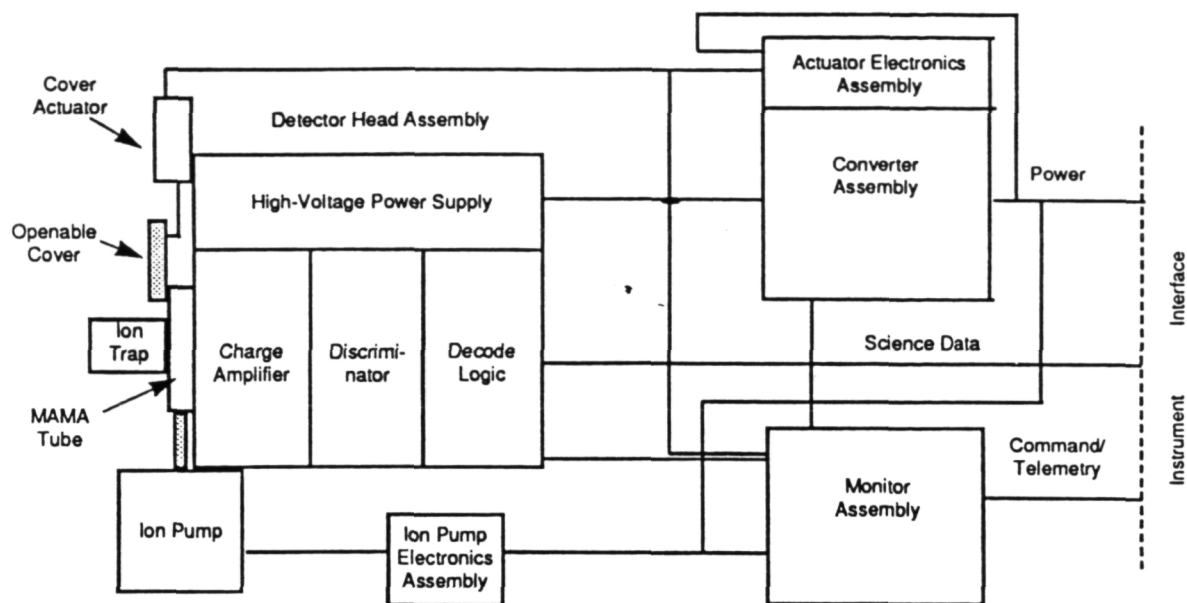**Fig. 3.** Openable-cover SOHO MAMA detector system subassemblies.

Fig. 4. Openable-cover SOHO MAMA detector system block diagram.

order to eliminate the effects of any systematic design problem in the openable-cover mechanism. The dual photocathode is again used on the back-up detector, even though some degradation of the KBr photocathode is

Fig. 5. SUMER MAMA detector system photocathode configuration.

expected during the several years that the detector must be stored under a dry N_2 purge during instrument and spacecraft integration and test. We originally planned to use solely the MgF_2 photocathode for the open detector, since this material has proved to be highly stable on exposure to dry N_2. However, a loss of sensitivity of even a factor of two in the KBr photocathode prior to launch will still yield significantly higher quantum efficiencies than MgF_2 at wavelengths longer than 80 nm, and will, accordingly, increase the scientific return in the event that the back-up detector has to be employed during the mission.

The UVCS detectors are designed primarily to observe radiation at wavelengths between 103 and 135 nm from the solar corona above the disk, and also to observe radiation at wavelengths between 61 and 135 nm on the solar disk. The sealed detector, designed to observe scattered H Ly α 121.6 nm radiation from the corona, has a MgF_2 window and a CsI photocathode deposited on the front face of the MCP. The sealed detector is sensitive to radiation in the wavelength band from 113 to >135 nm. Because of the optical configuration of the UVCS spectrometer, the UVCS tube must have a thin "wafer" configuration, with the distance from the front surface of the MgF_2 window to the CsI photocathode being no more than 7 mm.

The second detector, which is open with an openable cover and is identical in configuration to the SUMER prime detector, is used to observe radiation at shorter wavelengths. This detector has a KBr photocathode for maximum sensitivity at wavelengths between 93 and 107 nm. The detector is also used to observe radiation at wavelengths between 46 and 63 nm in second order.
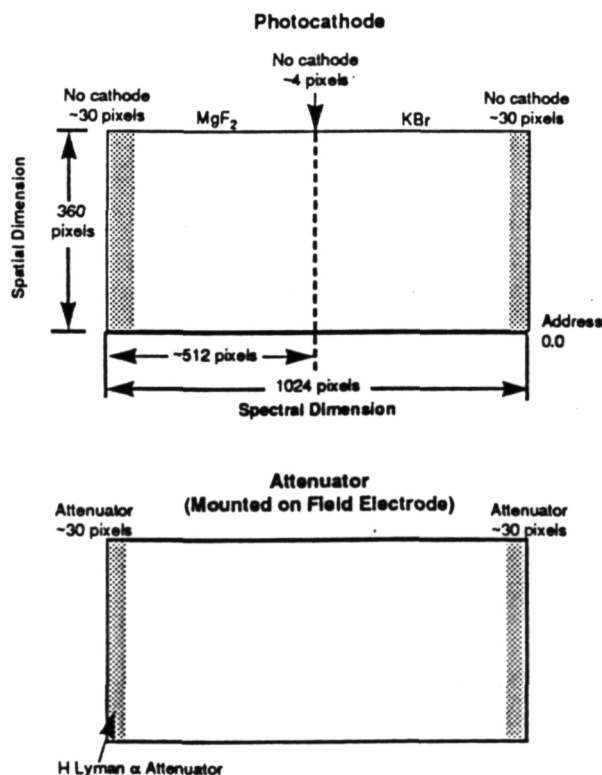
Breadboard (360 x 1024)-pixel MAMA detector systems have so far been delivered to the Astronomisches Institut Tübingen (AIT) in Germany and to the University of Padua in Italy to support the SUMER and UVCS development programs, respectively. The SUMER breadboard system has a CsI photocathode deposited on the front face of the MCP, and the Padua breadboard system has a KBr photocathode deposited on the front face of the MCP. A sealed breadboard UVCS detector system with a "wafer" tube having a MgF_2 window and a CsI photocathode deposited on the front face of the MCP will shortly be delivered to SAO. The configuration of the (360 x 1024)-pixel SOHO anode array is shown in Fig. 6a, and the configuration of the breadboard detector system, which employs discrete electronics components and is significantly larger than the flight units, is shown in Fig. 6b.

(a)
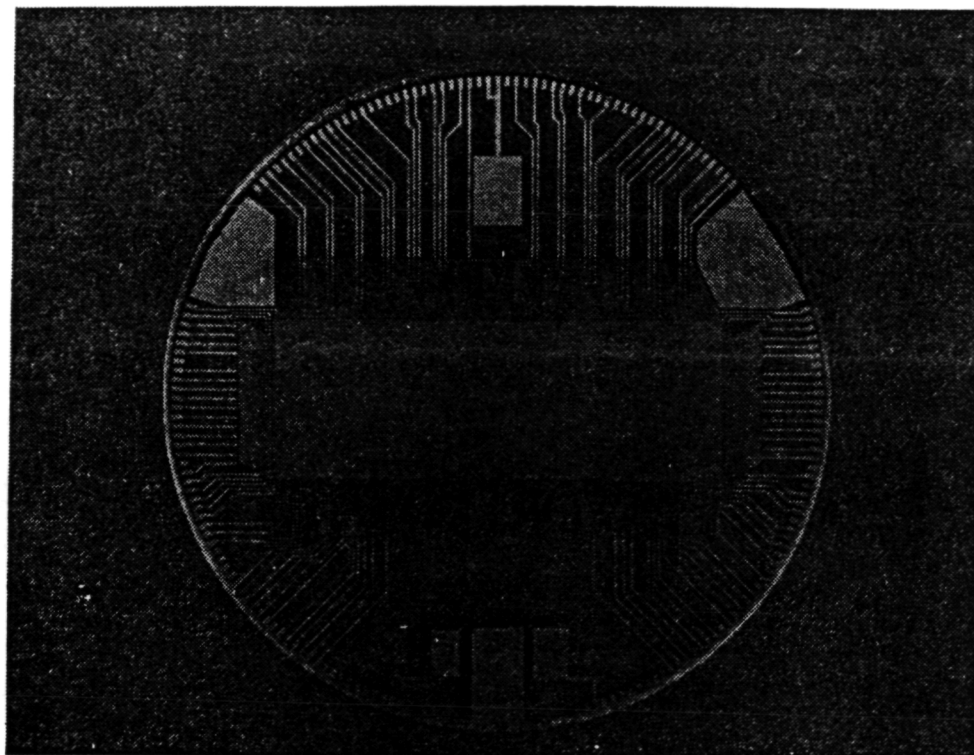
Fig. 6. SOHO MAMA Breadboard
Detector System.
(a) (360 x 1024)-pixel anode array
with 25 x 25 microns^2 pixels.
(b) Assembled breadboard
detector system with laboratory
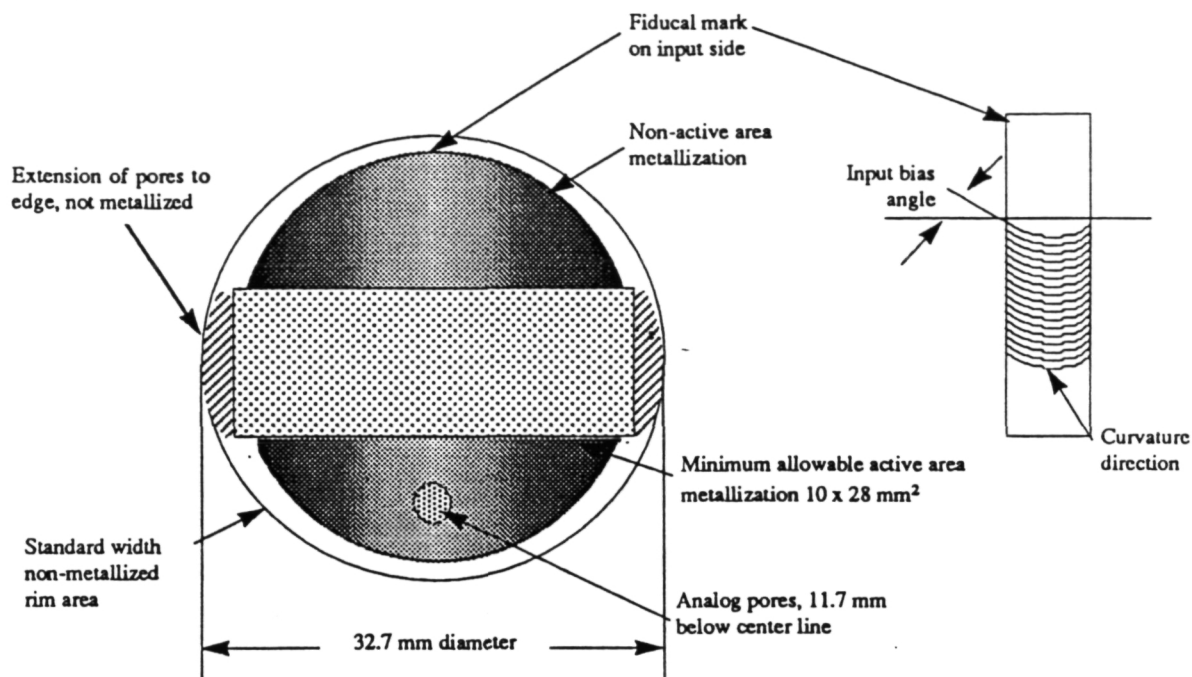evaluation tube attached.

(b)
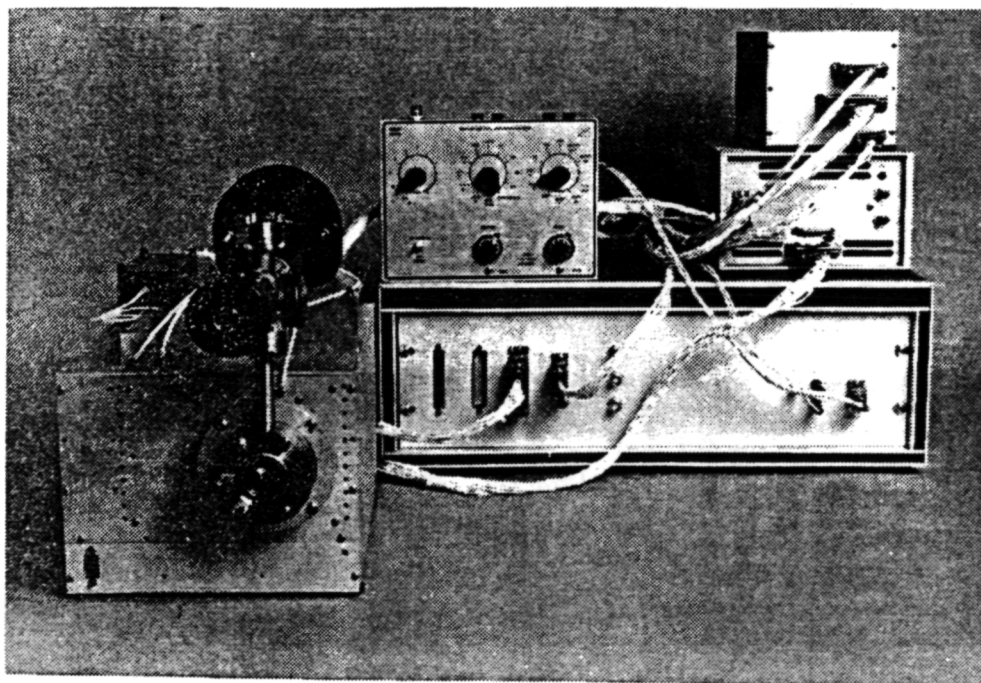
Fig. 7. Configuration of the SOHO Curved-channel MCP.

A prime consideration for the SOHO mission is that the detectors must have a very high dynamic range, both per pixel and from the total array. The optimized MCP configuration (see Fig. 7), which permits the use of a high-conductivity plate, and the new application-specific integrated circuit (ASIC) decode chip will be used in the flight detector systems and will significantly increase the maximum count rate capability from each pixel and from the total array. A 10% loss of detective quantum efficiency (DQE) at a single pixel rate in excess of 100 counts s^{-1} and a total array rate in excess of 6×10^5 counts s^{-1} are predicted on the basis of measurements to date with the breadboard detector systems. Some of the key performance characteristics for the SOHO flight detector systems are listed in Table 2. Since both instruments will employ the detectors in imaging spectrometers for high-accuracy line profile and line-shift measurements, the geometric fidelity of the detectors is of paramount importance. An image of a US Air Force test target recorded with the SUMER breadboard detector system is shown in Fig. 8. These imaging tests have
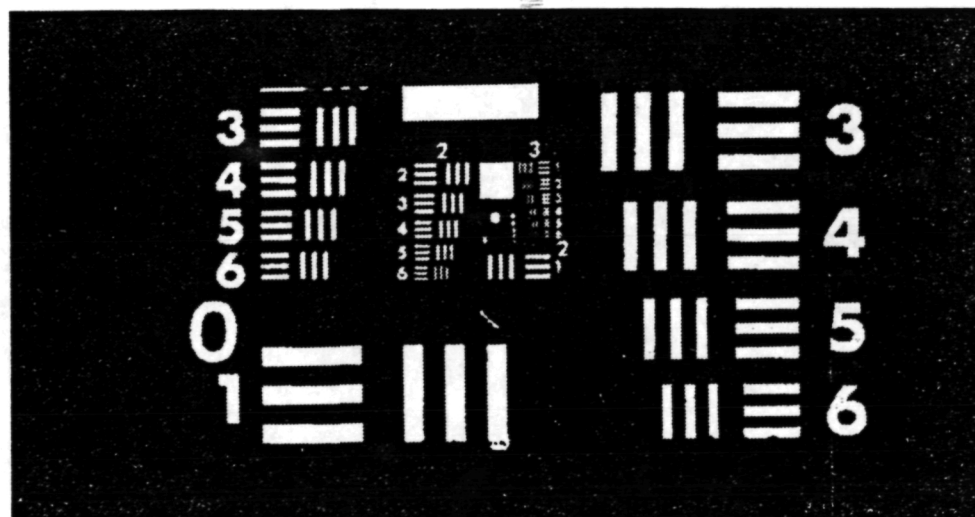
Fig. 8. Image of a test target recorded with (360 x 1024)-pixel SOHO MAMA breadboard detector system.

Table 2. Key SOHO MAMA Detector Performance Characteristics

Parameter	SUMER Detectors A & B	UVCS Sealed	UVCS Open	Units	Comments
Pixel resolution	25	25	25	Microns	FWHM
Crosstalk	< 2 (< 1 goal)	< 1	< 1	Percent / Percent	Into pixels adjacent to an illuminated pixel
	4×10^{-2} (< 10^{-2} goal)	< 10^{-2}	< 10^{-2}	Percent / Percent	Into a pixel two pixels or more from an illluminated pixel
Position sensitivity	< 2.5 (< 1.0 goal)	< 2.5	< 2.5	Microns / Microns	Ability to identify the centroid of a spectral or spatial feature with a diameter of 30 microns FWHM (S/N limited)
Spatial linearity	± 25 per 26 mm (± 5 goal)	± 5.0 per 13 mm ± 5.0 per 4 mm	± 5.0 per 13 mm ± 5.0 per 4 mm	Microns / Microns	Maximum variations dependent on curvature uniformity of C-plate MCP. C-plate is curved in 360 pixel direction.
Detective Quantum Efficiency (DQE):					Assumed to be 75 percent of photocathode quantum efficiency
Bare MCP	>7 (>10 goal)			Percent / Percent	Windowless at 584 Å
KBr	>20 (>30 goal)			Percent / Percent	Windowless at 1066 Å
MgF_2	>10 (>15 goal)			Percent / Percent	Windowless at 584 Å
CsI		>7 through MgF_2 window >10 through MgF_2 window		Percent / Percent	At 1164 Å At 1216 Å and 1304 Å
KBr			>20	Percent	Windowless at 584 Å and 1048 Å
Long wavelength cutoff: Bare MCP KBr MgF_2	1403 1700 1254			Å Å Å	Defined as wavelength where detective quantum efficiency (DQE) < 2 percent (< 1 percent goal)
CsI		< 1 at 2000 < 10^{-1} at 2500 < 10^{-2} at 3000 < 10^{-3} at 4000		Percent at Å Percent at Å Percent at Å Percent at Å	DQE
KBr			< 1 at 1700 < 10^{-1} at 2200 < 10^{-2} at 3200 < 10^{-3} at 4000	Percent at Å Percent at Å Percent at Å Percent at Å	DQE
Dark count rates: Bare MCP	< 0.02 (< 0.01 goal)			Counts $mm^{-2} s^{-1}$ Counts $mm^{-2} s^{-1}$	At < 30° C ambient temperature
KBr	< 0.2 (< 0.1 goal)			Counts $mm^{-2} s^{-1}$ Counts $mm^{-2} s^{-1}$	At < 30° C ambient temperature
MgF_2	< 0.07 (< 0.03 goal)			Counts $mm^{-2} s^{-1}$ Counts $mm^{-2} s^{-1}$	At < 30° C ambient temperature
CsI		< 0.1		Counts $mm^{-2} s^{-1}$	At < 30° C ambient temperature
KBr			< 0.1	Counts $mm^{-2} s^{-1}$	At < 30° C ambient temperature
Single pixel maximum true count rate	150	35	35	Counts s^{-1} Counts s^{-1}	At 30 percent loss of DQE At 10 percent loss of DQE
Single amplifier maximum count rate	> 2.0 x 10^5 > 6.0 x 10^5	> 2.4 x 10^4	> 2.4 x 10^4	Counts s^{-1} (random) Counts s^{-1} (random) Counts s^{-1} (random)	At 10 percent loss of DQE At 30 percent loss of DQE At 10 percent loss of DQE
Total array maximum count rate	> 3 x 10^5	> 3 x 10^5	> 3 x 10^5	Counts s^{-1} (random)	At 10 percent loss of DQE
Poisson response	5	5	5	Percent statistical significance level	Chi-square test comparing sample distribution to true Poisson distribution.

shown that the theoretical spatial resolution of 25 microns has been achieved and that the position sensitivity and spatial resolution are independent of both signal level and time. Small geometric nonuniformities are observed in the detector systems because of nonuniformities in the locations of the channels of the MCP. New techniques for manufacturing the curved-channel MCPs for the flight detector systems are expected to improve the geometric fidelity; however, the calibration of these spatial nonuniformities will be a major task in the detector characterization program.

4. STIS MAMA DETECTOR SYSTEMS

The NASA Goddard Space Flight Center's *Hubble* Space Telescope Imaging Spectrograph (STIS) is a multi-mode instrument designed for echelle spectroscopy, long-slit spectroscopy, slitless spectroscopy, photon time-tagging, and direct imaging. The instrument, as originally conceived, contains four detectors, each with formats of 2048 x 2048 pixels. Two Tektronix CCD's are used to cover the wavelength range from 300 to 1100 nm, and two MAMA detectors are used to cover the wavelength range from 300 nm down to the short wavelength limit of the MgF_2 window at 115 nm. The D-1 MAMA detector employs a CsI photocathode deposited on the front face of the MCP for optimum sensitivity in the range from 115 to 170 nm, and the D-2 MAMA detector employs a Cs_2Te photocathode which will either be deposited on the MgF_2 window of the detector tube, or on the front face of the MCP, to cover efficiently the wavelength range from 115 to 300 nm. The format of the STIS detector is 2048 x 2048 pixels, with pixel dimensions of 25 x 25 microns^2, fabricated from four contiguous (1024 x 1024)-pixel arrays with a 3-pixel dead space, as shown in Fig. 9. This arrangement provides redundancy, because an electronics failure in one quadrant will not affect the performance of the remaining three quadrants, and also increases the dynamic range of the detector by a factor of 4, since each quadrant works as an independent detector system. The characteristics of the STIS detector are listed in Table 3.

The "bake and scrub" of the first 75-mm-format "chevron" MCP stack received from Philips Components, Inc. is now in progress in preparation for the first imaging tests with this detector system.

As a precursor to the work with the (2048 x 2048)-pixel detector, we have constructed a number of (1024 x 1024)-pixel detectors in the 40-mm-format MAMA detector tubes, with the anode array configuration shown in Fig. 10. A rectified image recorded with one of these detector systems is shown in Fig. 11.

Recently, the STIS instrument has been forced to descope, and the (1024 x 1024)-pixel MAMA detector system is now baselined for this instrument. As shown in
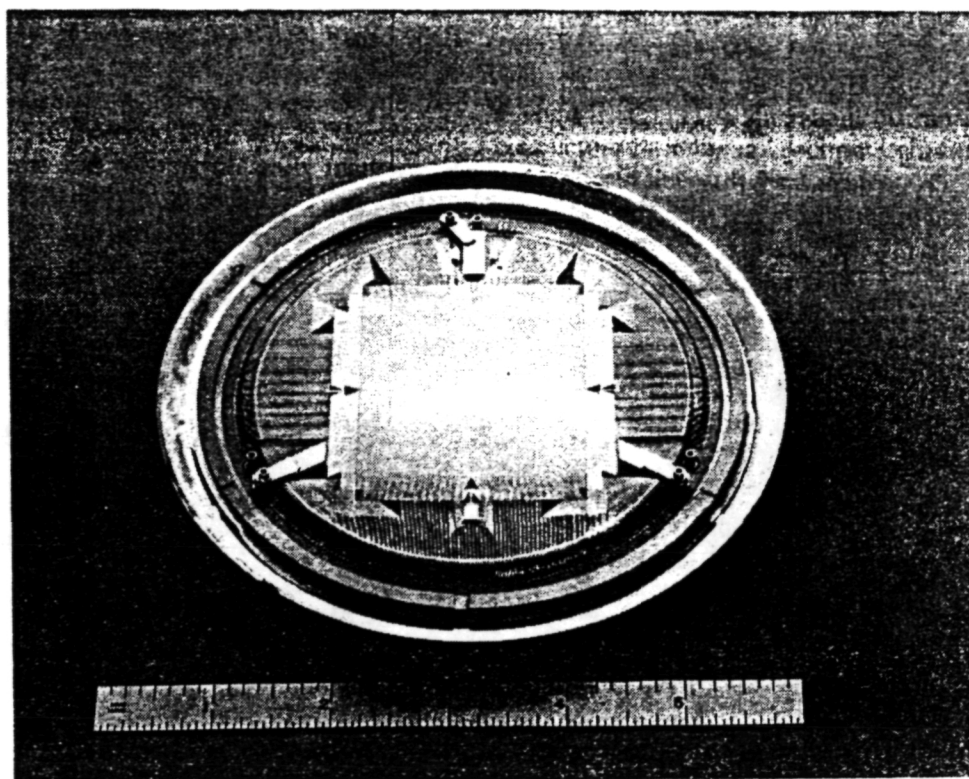

Fig. 9. STIS MAMA (2048 x 2048)-pixel anode array mounted on the 75-mm-format ceramic header. Pixel dimensions are 25 x 25 microns^2 and the dead space between the four (1024 x 1024)-pixel arrays is 3 pixels wide.

Table 3. Key Characteristics of the MAMA Detectors for STIS and FUSE/Lyman.

	STIS	FUSE
Pixel Format:	2048 x 2048 (4 x 1024 x 1024)	728 x 8096 (4 x 728 x 2024)
Pixel Dimensions:	25 x 25 microns^2	22 x 16 microns^2
Anode Array Active Area:	51.2 x 51.2 mm^2	16.0 x 32.4 mm^2 (x 4)
MCP Active Area:	52 x 52 mm^2	17 x 33 mm^2 (x 4)
MCP Pore Size:	10 microns	8 microns
Number of Amplifiers: (including analog output)	529 ([4 x 132] + 1)	577 ([4 x 144] + 1)
Photocathode Material:	CsI and Cs$_2$Te	KBr
Hybrid Amplifier and Discriminator	Yes	Yes
Gate Array Decode Circuits:	Yes	Yes
Openable Cover:	No	Yes

Fig. 10, the encoding electrode structures in the present (1024 x 1024)-pixel array have been located on only two sides of the active area to provide the capability for butting the four arrays together to form the (2048 x 2048)-pixel array. For the demonstration (1024 x 1024)-pixel MAMA detector now being fabricated for STIS, the encoding electrodes will be located on all four sides of the array, as for the SOHO array, in order to provide an optimized (1024 x 1024)-pixel structure for a very-long-duration flight mission.

5. FUSE/*LYMAN* MAMA DETECTOR SYSTEM

The prime EUV spectrograph of the FUSE instrument employs an aspheric concave diffraction grating in a Rowland circle mounting. Accordingly, the detector for this spectrograph must have a long rectangular format to cover the spectral range from 90 to 120 nm, with a spectral resolution ($\lambda/\delta\lambda$) of 30,000. In addition, the pixel size must

ORIGINAL PAGE IS
OF POOR QUALITY
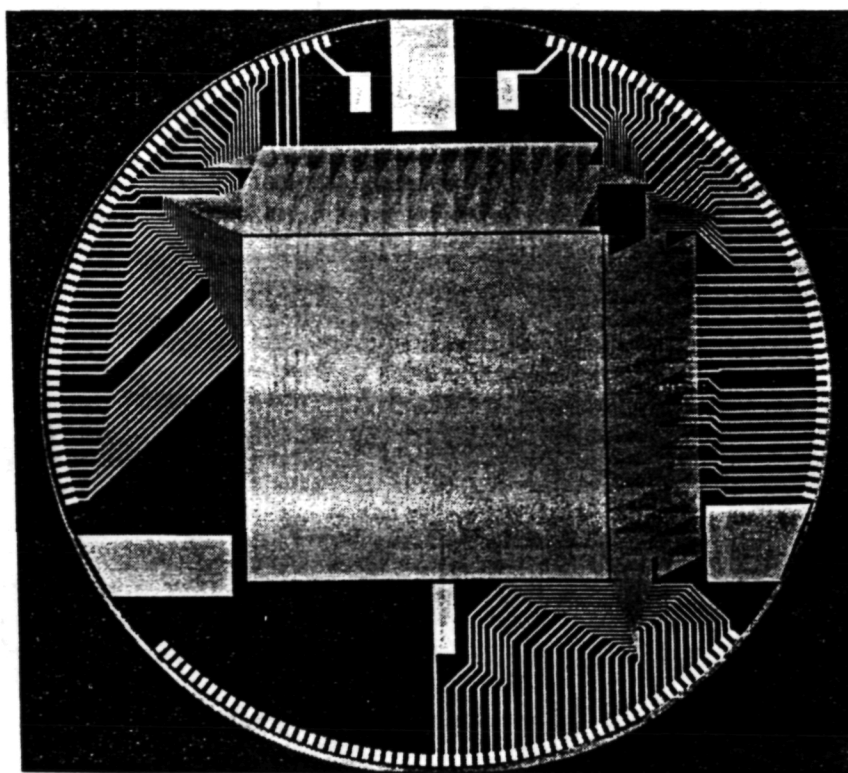
Fig. 10. STIS MAMA (1024 x 1024)-pixel anode array with 25 x 25 microns^2 pixels.
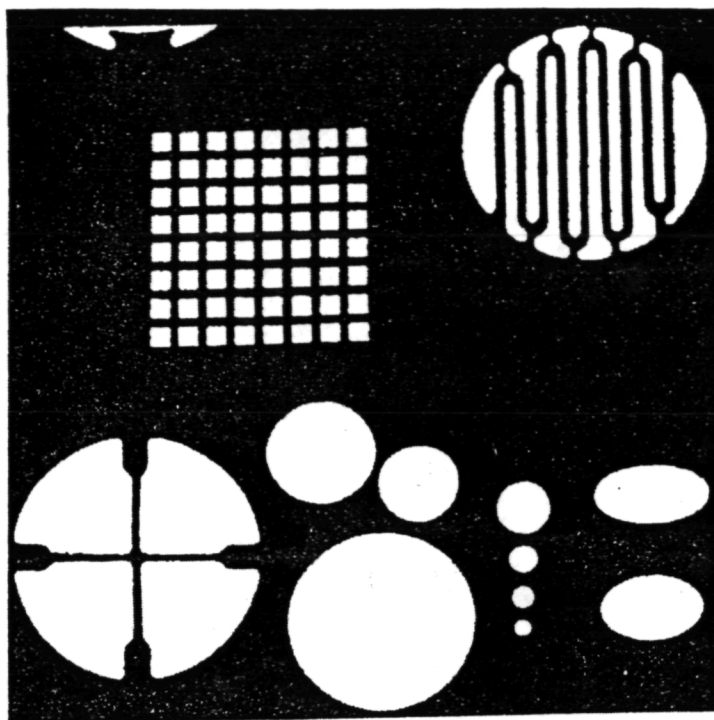
Fig. 11. Image recorded with STIS MAMA (1024 x 1024)-pixel detector system.

be smaller than 25 microns in order to obtain the required spectral resolution in a spectrograph with a size compatible with the limitations of the Explorer-class FUSE payload. The Phase A concept for the MAMA detector system is a (728 x 8096)-pixel detector composed of four contiguous (728 x 2024)-pixel arrays, each with 22 x 16 microns^2 pixels. The proposed configuration is shown in Fig. 12, and the key characteristics of the detector are listed in Table 3.

In order to validate the smaller pixel size in the MAMA detector system, as part of the FUSE Phase A study two (224 x 960)-pixel MAMA detector tubes with array pixel dimensions of 14 x 14 microns^2 were fabricated (see Fig. 13). One is a sealed tube with a bialkali visible light photocathode, and the other is an open, demountable tube which will be used for high-resolution studies at EUV wavelengths. The high-gain curved-channel MCP used with this array employs 8-micron-diameter channels on 10-micron centers, as shown in Fig. 13. Images of test targets taken with this detector system are shown in Fig. 14, and as shown in Fig. 15, it can be seen that the theoretical resolution of 14 microns is being achieved. Further evaluations of these detector systems in the open-structure mode at wavelengths below 120 nm will be undertaken later this year, using our toroidal grating imaging EUV spectrograph. High-resolution images will also be recorded using the new decode ASIC chip in order to determine if the resolution can be further improved to the theoretical limit of 10 microns set by the channel spacing of the MCP.
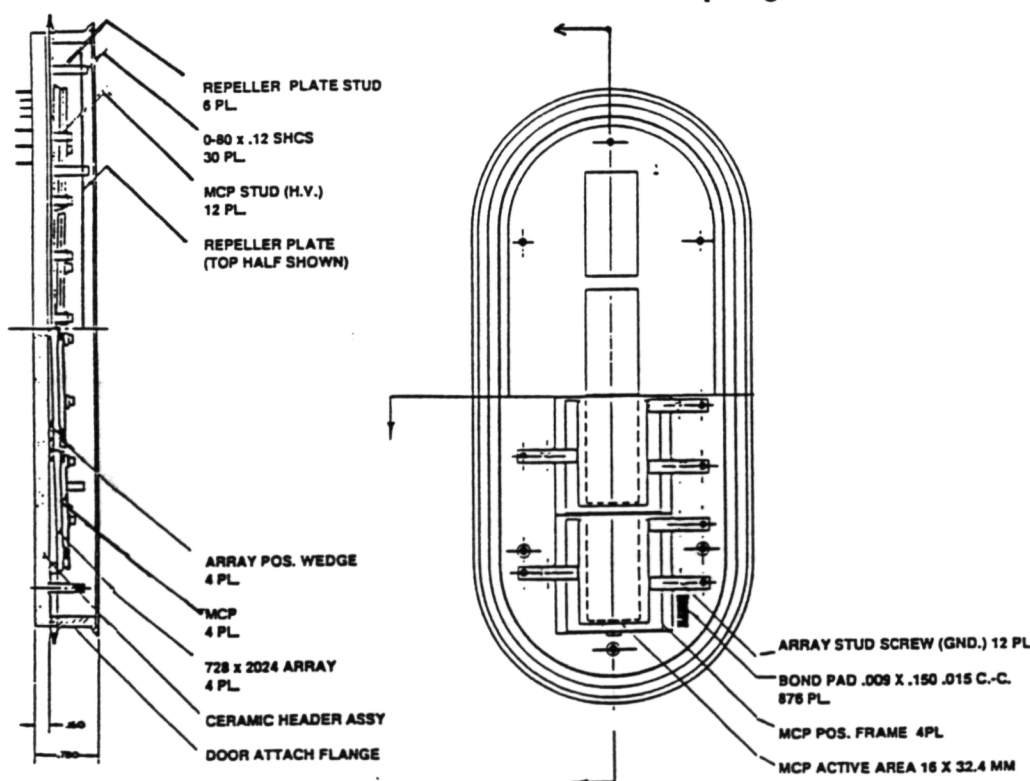

Fig. 12. Schematic of proposed FUSE MAMA detector composed of four contiguous (728 x 2024)-pixel arrays with 22 x 16 microns^2 pixels.
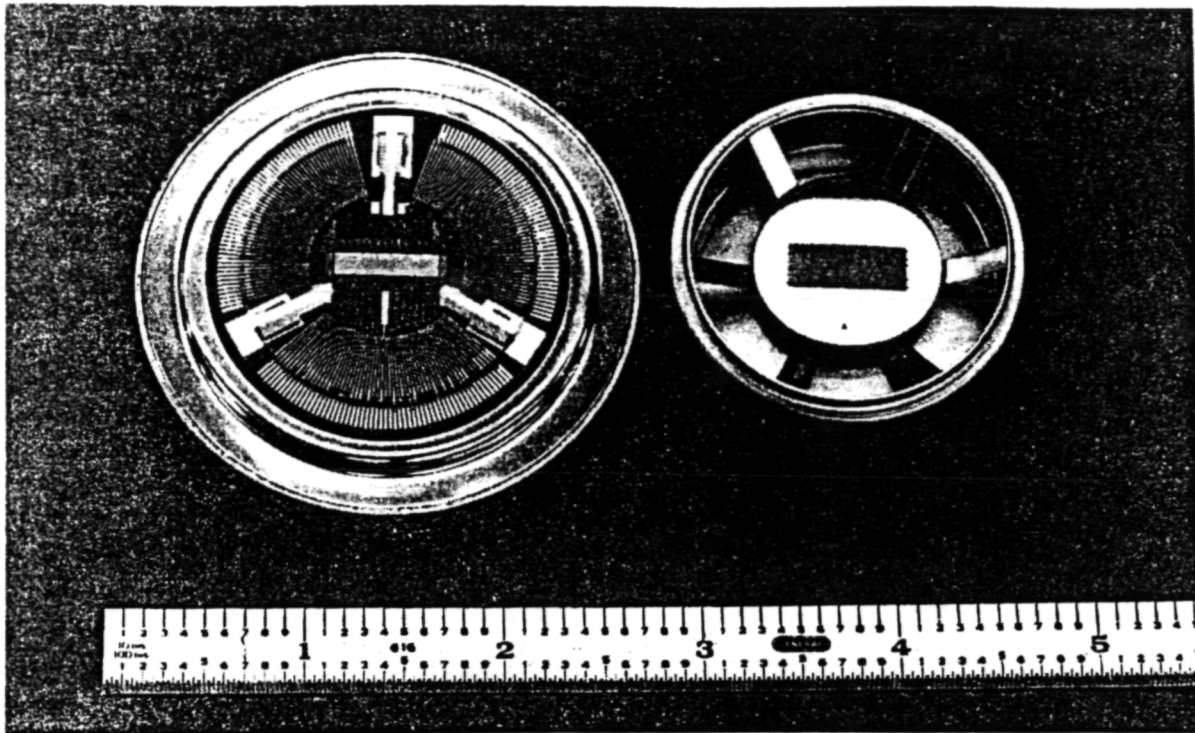
Fig. 13. Proof-of-concept FUSE MAMA (224 x 960)-pixel array with pixel dimensions of 14 x 14 microns^2. The curved-channel MCP has 8-micron-diameter channels on 10-micron centers.

6. THE ADVANCED TECHNOLOGY MAMA DETECTOR SYSTEM

The large amount of data being recorded with the MAMA detector systems, including those in the high-resolution imaging mode, have shown that the imaging characteristics of the detector system are being limited by the performance of the high-gain, curved-channel MCPs. In particular, nonuniformities of curvature and spatial distortions at the multi-fiber boundaries (see Fig. 16) are degrading the geometric fidelity of the MAMA anode array. In addition, the maximum single-pixel count rate of the MAMA is limited by the properties of the MCP. In order to
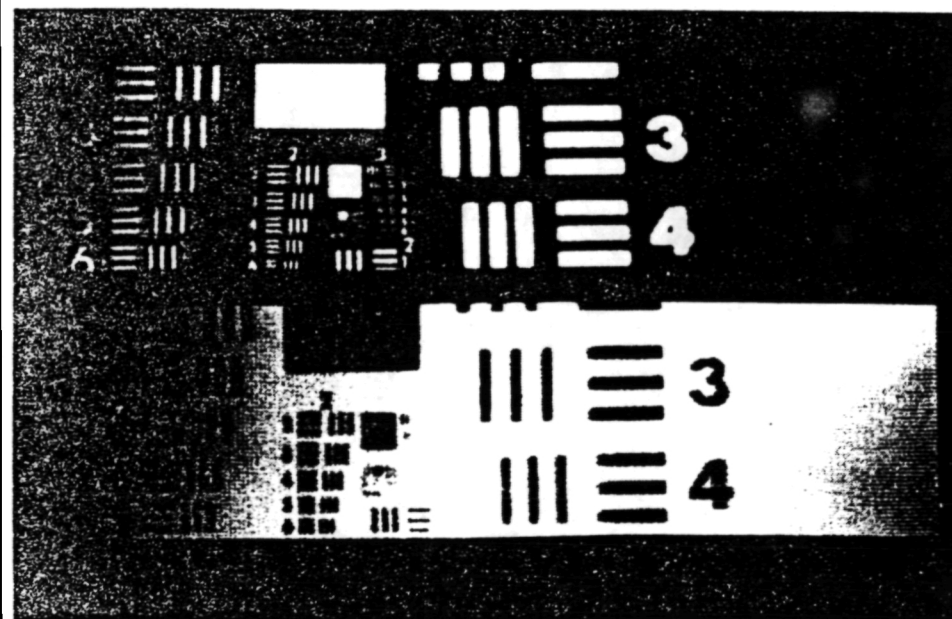
Fig. 14. Positive and negative images of a USAF test target taken at ultraviolet wavelengths with a (224 x 960)-pixel fine-fine array with 14 x 14 microns^2 pixels, and a curved-channel MCP with 8-micron-diameter channels. The sequence of bars in these images start with a resolution of 2.51 line pairs mm^{-1} (Group 0, element 3 on the right side of the images). The closest bars in the image have a resolution of 113.6 line pairs mm^{-1} (Group 5, element 6 to the left of the image centers).
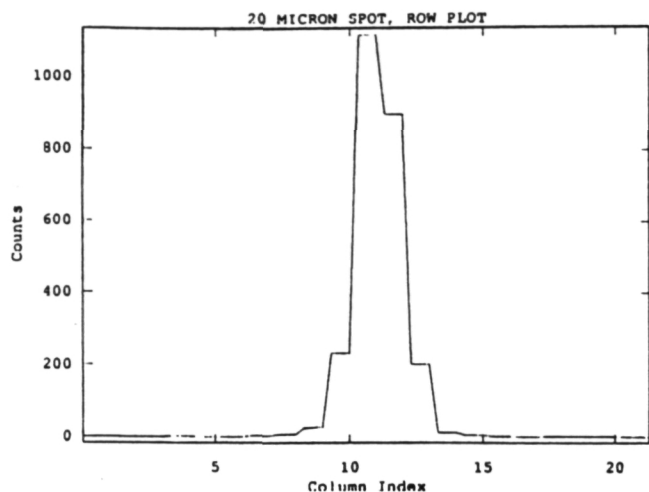
Fig. 15. A cut through an image of a 20-micron-diameter spot of ultraviolet light recorded with the 14 x 14 microns^2 pixel MAMA detector tube.

overcome these limitations, we have started investigations of improved MCPs fabricated from reduced lead silicate glass (RLSG) and, also, are conducting preliminary investigations into the possibility of fabricating advanced technology (AT) MCPs using silicon lithographic techniques.

For the RLSG MCPs, we plan to continue investigations of very small pore devices, and as part of the SOHO program, we are undertaking a series of developments at both Galileo Electro-Optics Corporation (GEOC) and Detector Technology, Inc., (Detech) in order to improve the degree of curvature and the uniformity of curvature in the present generation of MCPs. The potential advantages of the AT-MCPs are, first, the complete elimination of geometric distortions because of the precision of the lithographic fabrication process, and second, the possibility of producing a very-high-dynamic-range structure by fabrication of an optimized dynode structure. At this point in time, we have just started initial etch-tests with our first wafers in preparation for attempts to fabricate single-element and one-dimensional structures.
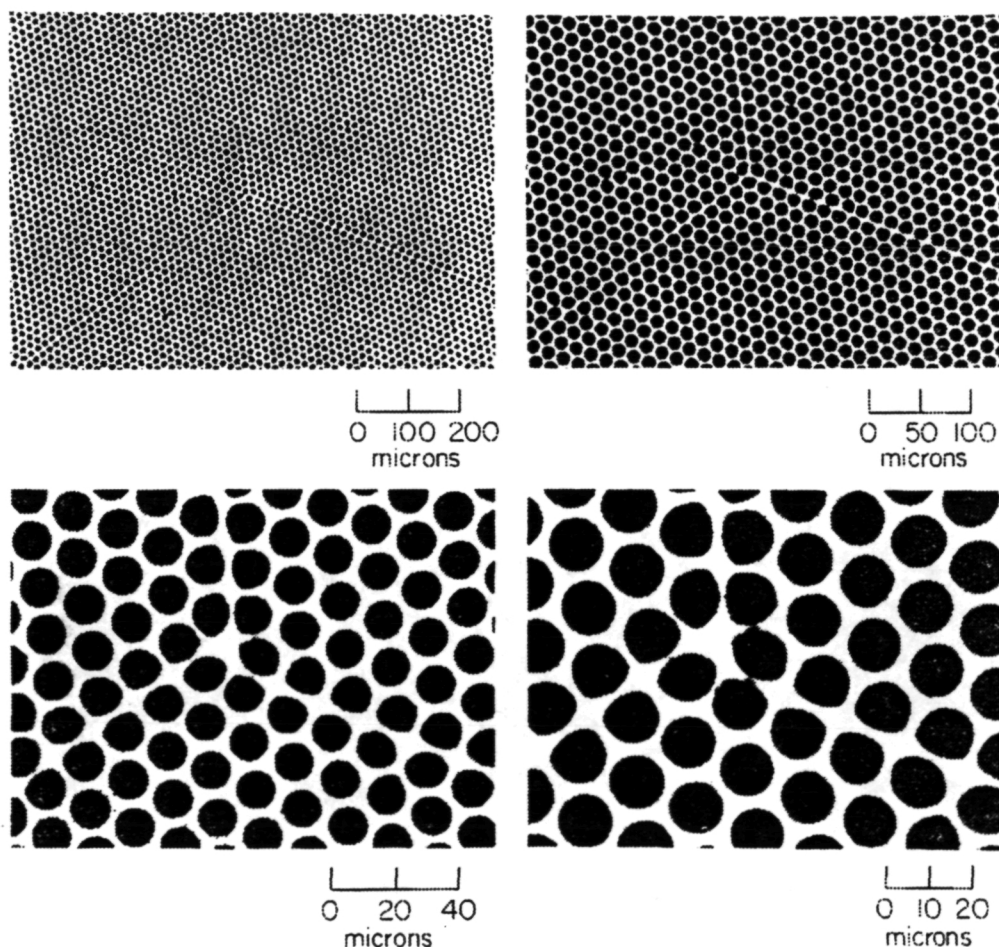
Fig. 16. Distortions of the interfaces of the multi-fibers in a curved-channel MCP.

7. ACKNOWLEDGEMENTS

8. REFERENCES

1. K. Wilhelm and the SUMER Investigation Team, "SUMER - Solar Ultraviolet Measurements of Emitted Radiation", European Space Agency *SP-1104*, pp. 31-37, November 1988.

2. J. Kohl and the UVCS Investigation Team, "UVCS - An Ultraviolet Coronagraph Spectrometer for SOHO", European Space Agency *SP-1104*, pp. 49-54, November 1988.

3. V. Domingo and A. I. Poland, "SOHO - An Observatory to Study the Solar Interior and the Solar Atmosphere", European Space Agency *SP-1104*, pp. 7-12, November 1988.

4. B. E. Woodgate and the Space Telescope Imaging Spectrograph Science Team, "Second Generation Spectrograph for the *Hubble* Space Telescope", *SPIE vol. 627 Instrumentation in Astronomy VI*, pp. 350-362, 1986.

5. "*Lyman* - The Far Ultraviolet Spectroscopic Explorer", NASA Phase A Study Final Report *NAS5-30339*, July 1989.

6. J. G. Timothy, "MAMA Detector Systems: A Status Report", *SPIE vol. 1158 Ultraviolet Technology III*, pp. 104-117, 1989.

7. J. G. Timothy, "Imaging Pulse-Counting Detector Systems for Space Ultraviolet Astrophysics Missions", to appear in *SPIE vol. 1494 Space Astronomical Telescopes and Instruments*, 1991.

8. D. B. Kasle, "Decoding Techniques for "fine-fine" Geometry Multi-Anode Microchannel Arrays", *SPIE vol. 932 Ultraviolet Technology II*, pp. 280-284, 1988.

9. D. B. Kasle, "High-resolution Decoding Techniques and Single-chip Decoders for Multi-anode Microchannel Arrays", *SPIE vol. 1158 Ultraviolet Technology III*, pp. 311-318, 1989.

10. D. B. Kasle and G. DeMicheli, "An Image Decoding ASIC for Space-Based Applications", to appear in *Proceedings of EURO ASIC 91*, IEEE Computer Society Press, 1991.

Photoelectronic Image Devices 1991

The McGee Symposium

Proceedings of the 10th Symposium on Photoelectronic Image Devices held at Imperial College of Science, Technology and Medicine, London, 2–6 September 1991

Edited by B L Morgan

Multi-anode microchannel array detector systems for space astrophysics missions

J Gethyn Timothy

Center for Space Science & Astrophysics, Stanford University ERL 314, Stanford, CA 94305, USA

ABSTRACT: The multi-anode microchannel arrays (MAMAs) are now under active development for use on a number of space ultraviolet astrophysics missions at far ultraviolet and extreme ultraviolet wavelengths. Visible-light versions of these detector systems are also being used for high-time-resolution studies, including speckle interferometry, at ground-based telescopes. The configurations of the different MAMA detector systems are described, and the use of custom application-specific integrated circuits (ASICs) in the electronics to improve the performance characteristics is discussed.

1. INTRODUCTION

We are currently fabricating and characterizing a number of different MAMA detector systems for use on space astrophysics missions at far ultraviolet (FUV) and extreme ultraviolet (EUV) wavelengths between about 300 and 28 nm. We are utilizing visible-light versions of these detector systems for scientific studies at ground-based telescopes at wavelengths between about 800 and 300 nm.

Open, open with openable cover, and sealed (360 x 1024)-pixel MAMA detector systems, with pixel dimensions of 25 x 25 microns^2 and MgF_2, KBr, and CsI photocathodes will be used in the Solar Ultraviolet Measurements of Emitted Radiation (SUMER) (Wilhelm *et al* 1988) and the Ultraviolet Coronagraph Spectrometer (UVCS) (Kohl *et al* 1988) instruments on the ESA/NASA SOHO mission (Domingo and Poland 1988), scheduled for launch in 1995. Prototype very-large-format (1024 x 1024)- and (2048 x 2048)-pixel MAMA detector systems with pixel dimensions of 25 x 25 microns^2 and CsI and Cs_2Te photocathodes are currently under test and in fabrication for the NASA Goddard Space Flight Center's *Hubble* Space Telescope Imaging Spectrograph (STIS) (Woodgate *et al* 1986), a second-generation instrument scheduled for in-orbit installation in 1997. Under this program a (256 x 1024)-pixel MAMA detector system has recently been flown twice on sounding rockets for FUV imaging of galaxies at wavelengths between about 125 and 170 nm. A (1024 x 1024)-pixel prototype FUV detector system will be flown on a sounding rocket in the coming year. Finally, proof-of-concept sealed and open (224 x 960)-pixel MAMA detector systems, with pixel dimensions of 14 x 14 microns^2 are under test as part of the FUSE/*Lyman* Phase B Study (NASA Final Report 1989). Visible-light versions of the (224 x 960)-pixel detector system and the (1024 x 1024)-pixel detector system are being utilized at ground-based telescopes in a number of high-time-resolution studies, including speckle interferometry.

2. MAMA DETECTOR SYSTEM

Details of the construction and mode-of-operation of the MAMA detector system have recently been presented in the literature (Timothy 1989 and 1991a). Briefly, the components of a MAMA detector consist of, first, the tube assembly and, second, the associated analog and digital electronic circuits. The MAMA detector tube, which can be sealed with a window or used in an open-structure configuration,

contains a single, high-gain, curved-channel microchannel plate (MCP) electron multiplier with the photocathode material deposited on, or mounted in proximity focus with the front surface. Electrodes are mounted in proximity focus with the output surface of the MCP to detect and measure the positions of the electron clouds generated by single photon events (see Figures 1 and 2). The charge collected on the anode electrodes is amplified and shaped by high-speed amplifier and discriminator circuits.
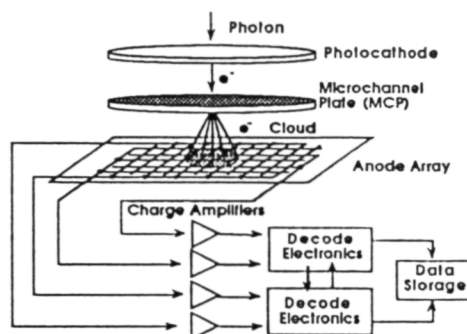
Digital logic circuits respond to the simultaneous arrival of the shaped signals from several of these electrodes in each axis, which are arranged in groups to uniquely

Figure 1. Schematic of the imaging MAMA detector system.

identify a x b pixels in one dimension with only a + b amplifier and discriminator circuits. In the imaging MAMA detector tube, two arrays are mounted in tandem with orthogonal orientations, so that the positions of the detected photons can be sensed in two dimensions. In this configuration $(a \times b)^2$ pixels can be uniquely identified with only 2 x (a + b) amplifier and discriminator circuits. Thus, a (1024 x 1024)-pixel array, for example, requires a total of only 128 amplifier and discriminator circuits. The two layers of anode electrodes in the imaging arrays are insulated from each other by a SiO_2 dielectric layer. The dielectric between the upper layer electrodes is etched away to allow the low energy (~30 eV) electrons in the charge cloud from the MCP to be collected simultaneously on both arrays. Details of the latest MAMA anode-array geometries and position-encoding algorithms can be found in the literature (Kasle 1988 and 1989; Kasle and DeMicheli 1991).
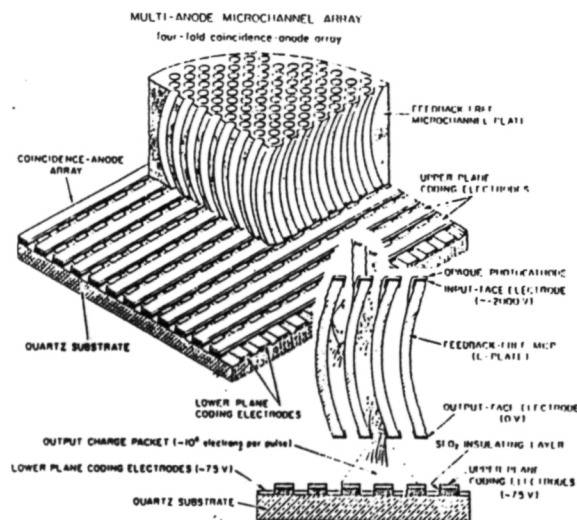
3. SOHO MAMA DETECTOR SYSTEMS

Figure 2. Schematic showing details of the curved-channel MCP and the imaging multi-layer anode array used in the MAMA detector tubes.

The MAMA detectors for the SUMER and UVCS instruments on the SOHO mission have a high degree of commonality, but also significant differences dictated by the scientific needs of the two instruments (Timothy 1991b). All of the detectors have formats of 360 x 1024 pixels and pixel dimensions of 25 x 25 microns². The other key parameters are listed in Table 1.

The open detector with the openable cover is utilized for both SUMER and UVCS. The purpose of the cover is to protect the photocathode materials and the high-gain MCP from contamination during the years of the instrument and spacecraft integration and test programs. The different subassemblies which make up the openable-cover SOHO MAMA

Table 1. Key Parameters of the MAMA Detectors for the SUMER and UVCS Instruments on the SOHO Mission.

	SUMER		UVCS	
	Detector A	Detector B	Detector 1	Detector 2
Pixel Format	360 x 1024	360 x 1024	360 x 1024	360 x 1024
Pixel Dimensions	25 x 25 μm^2	25 x 25 μm^2	25 x 25 μm^2	25 x 25 μm^2
Anode Array Active Area	9.0 x 25.6 mm^2	9.0 x 25.6 mm^2	9.0 x 25.6 mm^2	9.0 x 25.6 mm^2
MCP Active Area	10 x 27 mm^2	10 x 27 mm^2	10 x 27 mm^2	10 x 27 mm^2
MCP Pore Size	12 microns	12 microns	12 microns	12 microns
Number of Amplifiers (including analog output)	105 (104+1)	105 (104+1)	105 (104+1)	105 (104+1)
Photocathode Material	MgF_2 and KBr	MgF_2 and KBr	CsI	KBr
Configuration	Openable cover	Open	Sealed	Openable cover

detector system are shown in Figure 3a, and the detector block diagram is shown in Figure 3b.

The back-up detector in the SUMER instrument is open, and does not have the openable cover in order to eliminate the effects of any systematic design problem in the openable cover mechanism. Great care will need to be taken, however, to ensure that the photocathodes and the MCP in this detector are not contaminated during the prelaunch integration and test programs.
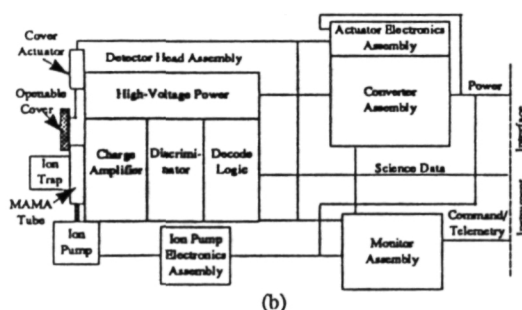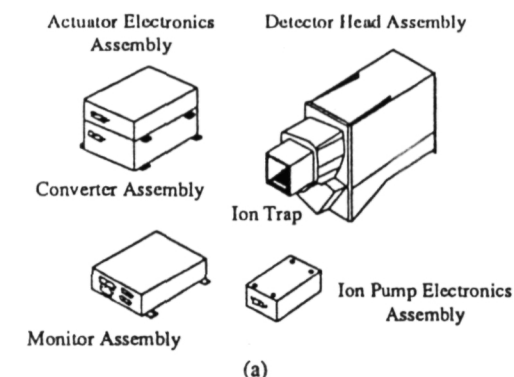

(a)

(b)

Figure 3. Openable-cover SOHO MAMA detector system. (a) System subassemblies. (b) System block diagram.

Both of the SUMER detectors employ a dual photocathode structure. Two photocathode materials are deposited on the front face of the curved-channel MCP: KBr for a high quantum efficiency at wavelengths between 80 and 160 nm, and MgF_2 for both a high quantum efficiency at wavelengths between 40 and 80 nm and also to provide rejection of radiation at, and around, the wavelength of the strong H Lyman α 121.6 nm emission line.

The UVCS MAMA sealed detector, designed to observe scattered H Lyman α 121.6 nm radiation from the solar corona, has a MgF_2 window and a CsI photocathode deposited on the front face of the MCP. The sealed detector is sensitive to radiation in the wavelength band from 113 to > 135 nm. Because of the optical configuration of the UVCS spectrometer, the sealed UVCS MAMA tube must have a thin "wafer" configuration, with the distance from the front surface of the MgF_2 window to the CsI photocathode being no more than 7 mm.

The second UVCS MAMA detector, which is open with an openable cover and is identical in configuration to the SUMER MAMA detector, is used to observe radiation at shorter wavelengths. This detector has a KBr

and also increases the dynamic range of the detector by a factor of four, since each quadrant works as an independent detector system.

The key characteristics of the STIS detector are listed in Table 2.

Recently the STIS instrument has been forced to descope and the (1024 x 1024)-pixel MAMA detector system (see Figure 4), which we have fabricated as a precursor to the fabrication of the (2048 x 2048)-pixel system, is now baselined for this instrument. Imaging tests with prototype versions of these detectors are now underway, and preparations are being made for the flight of a (1024 x 1024)-pixel detector system on a sounding rocket in November 1991.

Table 2. Key Characteristics of the MAMA Detectors for STIS.	
Pixel Format:	2048 x 2048 (4 x 1024 x 1024)
Pixel Dimensions:	25 x 25 microns^2
Anode Array Active Area:	51.2 x 51.2 mm^2
MCP Active Area:	52 x 52 mm^2
MCP Pore Size:	10 microns
Number of Amplifiers: (including analog output)	529 ([4 x 132] + 1)
Photocathode Materials:	CsI and Cs$_2$Te

5. FUSE/*LYMAN* MAMA DETECTOR SYSTEM

The prime EUV spectrograph of the FUSE instrument employs an aspheric concave diffraction grating in a Rowland circle mounting. Accordingly, the detector for this spectrograph must have a long rectangular format to cover the spectral range from 90 to 120 nm, with a required spectral resolution ($\lambda/\Delta\lambda$) of 30,000. In addition, the pixel size must be smaller than 25 microns in order to obtain the required spectral resolution in a spectrograph with a size compatible with the limitations of the Explorer-class FUSE payload. The Phase A concept for the MAMA detector system is a (728 x 8096)-pixel detector composed of four contiguous (728 x 2024)-pixel arrays, each with 22 x 16 microns^2 pixels. The proposed configuration is shown in Figure 5, and the key characteristics of the detector are listed in Table 3.

In order to validate the smaller pixel size in the MAMA detector system as part of the FUSE Phase A study, two (224 x 960)-pixel MAMA detector tubes with pixel dimensions of 14 x 14 microns^2 were fabricated (see Figure 4). The high-gain curved-channel MCP used with this array employs 8-micron-diameter channels on 10-micron centers. Images of test targets taken with this detector system have
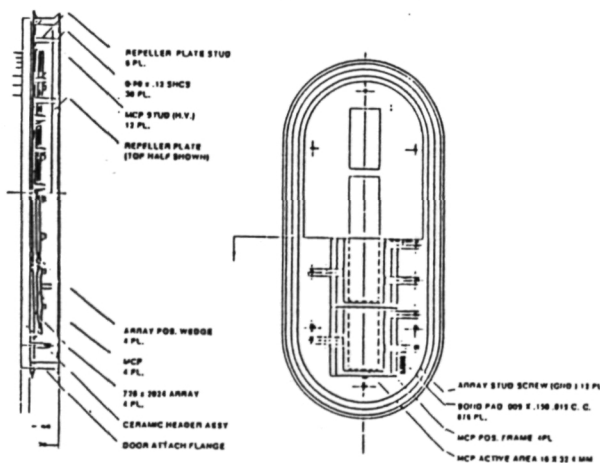

Figure 5. Schematic of proposed FUSE MAMA detector composed of four contiguous (728 x 2024)-pixel arrays with 22 x 16 microns^2 pixels.

demonstrated the theoretical spatial resolution of 14 microns. Further evaluations of this detector system in the open-structure mode at wavelengths below 120 nm will be undertaken later this year, using our toroidal grating imaging EUV spectrograph. High-resolution images will also be recorded with the visible-light detector tube in the laboratory and at ground-based telescopes using the new decode ASIC chip in order to determine if the resolution can be further improved to the theoretical limit of 10 microns set by the channel spacing of the MCP.

Table 3. Key Characteristics of the MAMA Detector for FUSE/*Lyman*.

Pixel Format:	728 x 8096 (4 x 728 x 2024)
Pixel Dimensions:	22 x 16 microns^2
Anode Array Active Area:	16.0 x 32.4 mm^2 (x 4)
MCP Active Area:	17 x 33 mm^2 (x 4)
MCP Pore Size:	8 microns
Number of Amplifiers: (including analog output)	577 ([4 x 144] + 1)
Photocathode Material:	KBr

6. IMAGING TESTS WITH THE MAMA DETECTOR SYSTEMS

The visible-light versions of the MAMA detector systems are being used in conjunction with our speckle camera in an ongoing program of speckle interferometry and speckle imaging at ground-based telescopes. The MAMA has a unique capability to identify the time of arrival of each detected photon to an accuracy significantly better than a microsecond. The pulse-pair resolution of the custom ASIC decode chip is better than 160 ns, and the temporal resolution of our time-tag system used for ground-based observations is currently set at 10 μs. The results of deconvolving the images of unresolved binary stars are shown in Figure 6. The advantage of taking this type of data with the MAMA detector system is that the integration time can be optimized for the maximum signal-to-noise ratio during the data-reduction phase of the program, rather than during the observing time at the telescope. A plot of the dependence of the signal-to-noise ratio on the integration time is shown in Figure 7.

An ultraviolet image of the galaxy NGC 4449 recorded on the last flight of the NASA Goddard Astronomy
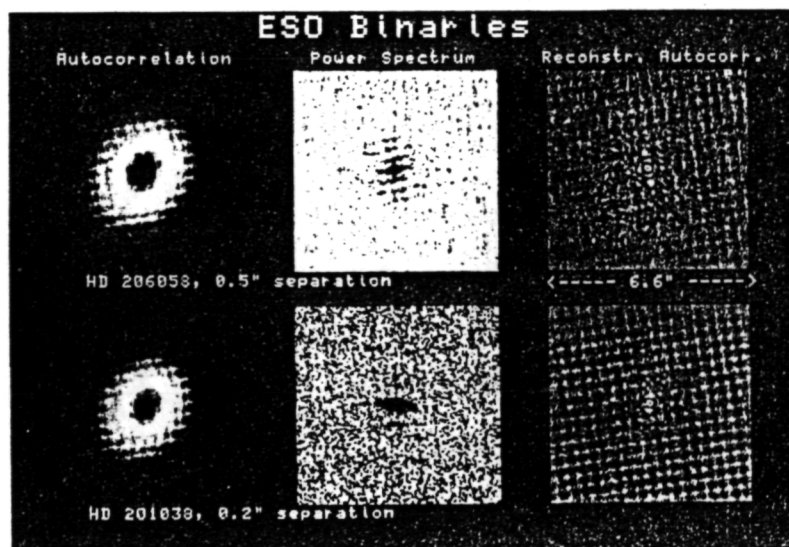

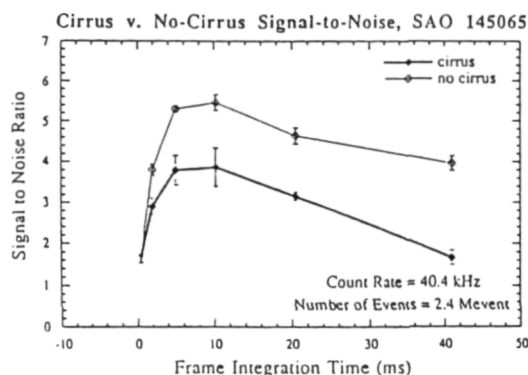Figure 6. Deconvolved images of unresolved binary stars recorded with the MAMA detector in the time-tag mode.

Cirrus v. No-Cirrus Signal-to-Noise, SAO 145065

Figure 7, Dependence of the signal-to-noise ratio of the speckle data on the integration time used to bin the time-tag data stream.

Sounding Rocket Payload (ASRP), is shown in Figure 8. Again, the time-tag mode of recording data was used to produce this image and to correct for the effects of the drifts of the sounding rocket pointing system.

As described recently by Kasle (1989) and Kasle and De Micheli (1991), the new custom decode ASIC chip enables us to use more sophisticated algorithms for decoding the positions of the detected photons. In this way, it is possible to double the resolution of the existing 25-micron pixel and 14-micron pixel MAMA detector systems, provided that the center-to-center spacing of the channels in the curved-channel MCP is small enough. The first tests of this technique have been recently undertaken, using one of the (360 x 1024)-pixel SOIIO breadboard detector systems with 25 x 25 microns^2 pixels. The improvement in resolution using the new high-resolution decode algorithm can be seen in the images of a US Air Force test target shown in Figure 9. The measured spatial resolution of this system increased from 25 microns to 16 microns FWHM, which is close to the theoretical limit of 15 microns expected from the spacing of the channels in the curved-channel MCP. Further detailed tests of this high-resolution system are now continuing, with particular emphasis on the stability of the high-resolution imaging point-spread-function as functions of both time and signal level. On the basis of these measurements, we can now foresee the use of MAMA detector systems with spatial resolutions as high as 7 to 8 microns, provided that curved-channel MCPs with channel diameters of 6 microns or less can be successfully fabricated.

Figure 8. Image of the starburst irregular galaxy NGC 4449 in the wavelength range from 125 to 170 nm recorded with a (256 x 1024)-pixel MAMA detector system on the NASA Goddard Astronomy Sounding Rocket Payload. The image has been corrected for drifts in the rocket attitude control system using the MAMA time-tag data stream.

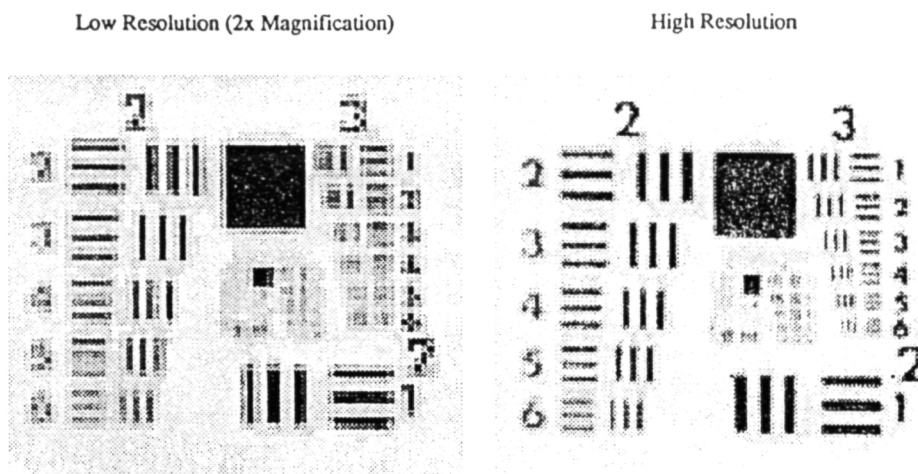Low Resolution (2x Magnification)   High Resolution

Figure 9. Normal-resolution image of groups 2 through 7 of a US Air Force test target and a high-resolution image of the same target recorded with a SOHO MAMA breadboard detector system.

7. ACKNOWLEDGEMENTS

8. REFERENCES

Domingo and Poland A I 1988 *European Space Agency* SP-1104 7-12
Kasle D B 1988 *SPIE Ultraviolet Technology II*, **932** 280-284
Kasle D B 1989 *SPIE Ultraviolet Technology II*, **1158** 311-318
Kasle DB and DeMicheli G 1991 *Proceedings of EUROPEAN ASIC 91* (IEEE Computer Soc Press)
Kohl J and the UVCS Investigation Team 1988 *European Space Agency* SP-1104 49-54
NASA Phase A Study Final Report 1989 NAS5-30339
Timothy J G 1989 *SPIE Ultraviolet Technology III* 1158 104-117
Timothy J G 1991a *SPIE Space Astronomical Telescopes and Instruments* 1494 (in press)
Timothy J G 1991b *SPIE EUV, X-Ray & Gamma Ray Instrumentation for Astronomy II* 1549 (in press)
Wilhelm K and the SUMER Investigation Team 1988 *European Space Agency* SP-1104 31-37
Woodgate B and the Space Telescope Imaging Spectrograph Science Team 1986 *SPIE Instrumentation in Astronomy VI* 627 350-362

An Imaging Extreme Ultraviolet Spectrometer
for Astrophysical Investigations in Space

M. C. E. Huber

Institut für Astronomie
ETH-Zentrum, CH-8092
Zürich, Switzerland (41) 1-256-3632

J. G. Timothy and J. S. Morgan

Center for Space Science and Astrophysics,
ERL 313, Stanford University
Stanford, CA 94305 U.S.A. (415) 725-0444

G. Lemaître

Observatoire de Marseille
2 place Le Verrier, CF-13004, Marseille, France
(33)-91-959088

G. Tondello

Instituto di Elettronica, Università di Padova,

M. E. Puiatti and P. Scarin

Instituto Gas Ionizzati, CNR, 6/A via Gradenigo, I-35100
Padova, Italy, (39) 49-8070268

Abstract

A high-efficiency, extreme ultraviolet (EUV) imaging spectrometer has been con-
structed and tested. The spectrometer employs a concave toroidal grating illuminated at
normal incidence in a Rowland circle mounting and has only one reflecting surface. The
toroidal grating has been fabricated by a new technique employing an elastically
deformable sub-master grating which is replicated in a spherical form and then mechanically
distorted to produce the desired aspect ratio of the toroidal surface for stigmatic
imaging over the selected wavelength range. The fixed toroidal grating used in the
spectrometer is then replicated from this surface. Photographic tests and initial photo-
electric tests with a two-dimensional, pulse-counting detector system have verified the
image quality of the toroidal grating at wavelengths near 600 Å. The basic designs of
two instruments employing the spectrometer for astrophysical investigations in space are
described, namely, a high-resolution EUV spectroheliometer for studies of the solar chromo-
phere, transition region, and corona; and an EUV spectroscopic telescope for studies of
non-solar objects.

Introduction

The extreme ultraviolet (EUV) spectral region at wavelengths below ∿ 1200 Å is of
critical importance for studies of dynamic phenomena in the outer atmospheres of the sun
and other stars. In addition, observations at these wavelengths can provide unique
astrophysical data on dynamic phenomena in planetary atmospheres and magnetospheres, on
the exchange of matter and energy between stars and the interstellar medium, on the
variations of light element abundances in the galaxy and on the dynamics of the hot inter-
stellar gas in galactic haloes. Because of the lack of window materials and of high-
reflectivity optical surfaces at these wavelengths, practical systems for imaging and
spectroscopy must employ open-structure detector systems and a minimum number of
reflecting surfaces. The recent development of high-resolution imaging detector systems
which can operate with high efficiency at EUV wavelengths has stimulated the design of
optical systems which can provide a stigmatic spectroscopic capability. These imaging
spectrometer systems can provide the simultaneous spectral, spatial and temporal
resolutions required for many scientific observations that have not been previously
possible. In this paper we describe the fabrication and the results of initial tests of a
toroidal diffraction grating for use in an imaging EUV spectrometer at wavelengths between
300 and 1200 Å.

Spectrometer Design

The design of the spectrometer was stimulated by the need for high-time-resolution observations of the solar corona with a high spectral resolution ($\lambda / \Delta \lambda \sim 2 \times 10^4$) and a spatial resolution of 1 arc second or better.[1] The configuration of the spectrometer mounting is shown in Figure 1.
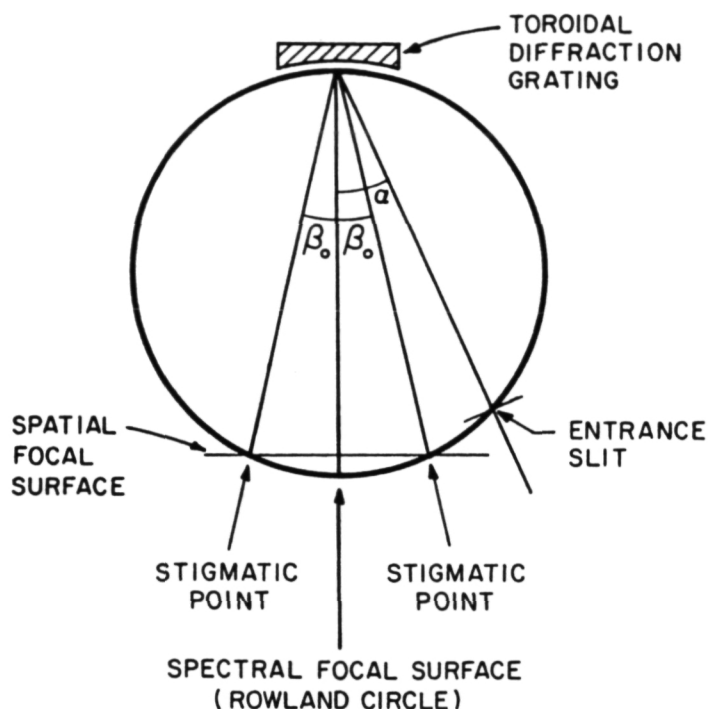

Figure 1.   Schematic of the imaging EUV spectrometer employing a single toroidal grating. Exact stigmatic focusing is obtained at angles of diffraction $\pm \beta_0$, which are defined by equation 1. Given a sufficiently small value of β_0 and some depth of focus, effective stigmatic focusing can be achieved between and somewhat beyond the two stigmatic points.

In the conventional Rowland circle mounting, the vertical and horizontal foci from a spherical diffraction grating are not coincident. However, Haber[2] has pointed out that it is possible to obtain exact stigmatic focusing at two points in the spectrum by selecting the vertical radius of curvature R_v of a toroidal grating to be smaller than its horizontal radius R_h. As shown in Figure 1, exact stigmatic focusing can then be obtained at two positions in the spectrum given by:

$$R_v = R_h \cos \alpha \cos \beta_0 \qquad\qquad (1)$$

In a practical system where β_0 is small and there is some depth of focus (focal ratios $\gtrsim$ f/15), stigmatic focusing can be achieved between and somewhat beyond the two stigmatic points.

A number of possible imaging systems can be constructed using this mounting. As shown in Figure 2a, the grating can be combined with a normal-incidence Gregorian telescope to produce a high-resolution EUV spectroheliometer for high-spatial-resolution studies of the solar chromosphere, transition region, and corona. Alternatively, as shown in Figure 2b, the grating can be combined with Wolter type II grazing-incidence telescope for astrophysical studies at wavelengths below 1200 Å. This telescope and spectrometer combination can provide a high observing efficiency for studies at wavelengths down to about 400 Å. It should, however, be noted that a simple toroidal grating will not provide optimum performance for focal ratios lower than about f/15. Fast systems for astronomical studies will need gratings in which higher order aberrations have been corrected.
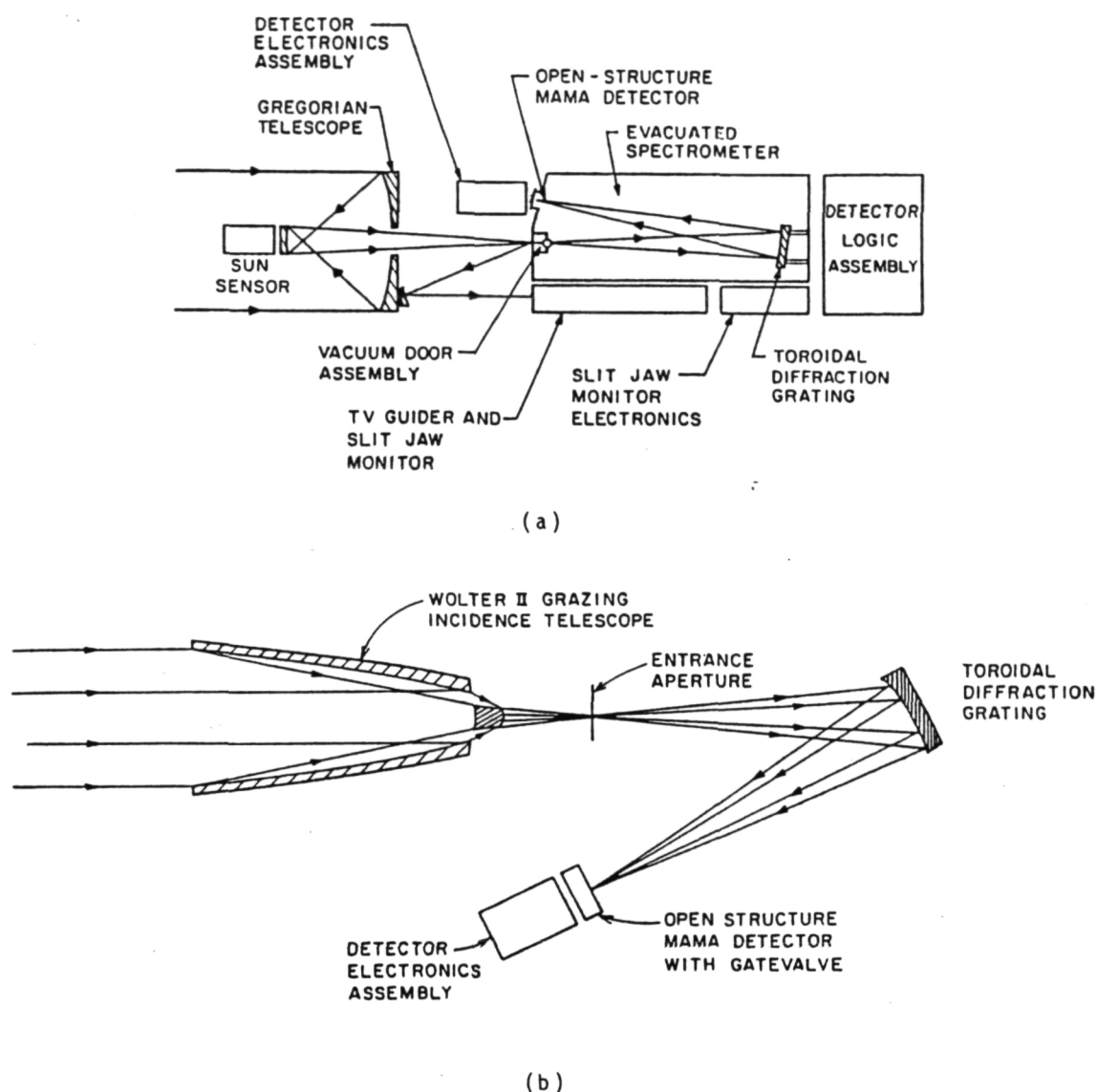
(a)

(b)

Figure 2. Schematics of telescope and imaging spectrometer systems.

    (a) High-resolution EUV spectroheliometer using a Gregorian telescope.
    (b) Grazing-incidence telescope and normal-incidence spectrometer
        combination for astrophysical studies at wavelengths below 1200 Å.

Grating Fabrication

    In order to evaluate the performance characteristics of a toroidal grating at EUV
wavelengths, we have fabricated a toroidal replica grating using a unique fabrication
technique developed at Marseille. This technique uses an elastically deformable grating
which is replicated from a spherical master ruling. The ratio of the vertical and
horizontal radii of curvature can then be set to any desired value by applying a
distorting force to the flexible substrate. The stainless steel flexible substrate (see
Figure 3) has a form which elastically deforms into an exact toroidal surface with the
application of a single distorting force. The form of the substrate is described in
reference 3. The grating, with a ruling frequency of 3600 grooves mm^{-1}, and an active
area of 70 x 70 mm^2, was replicated onto the deformable concave substrate by Hyperfine,
Inc.[4], from a concave spherical master ruling using an intermediate convex replicating
surface. After the substrate had been deformed to the appropriate aspect ratio, a fixed
concave toroidal grating was replicated from the deformable substrate again using an
intermediate convex replicating surface. The aspect ratio of the toroid was determined in
two ways: first, by using a Twyman-Green interferometer and second, by determining the
angles for stigmatic imaging in the zeroth order. The characteristics of the final
toroidal replica grating are given in Table 1.
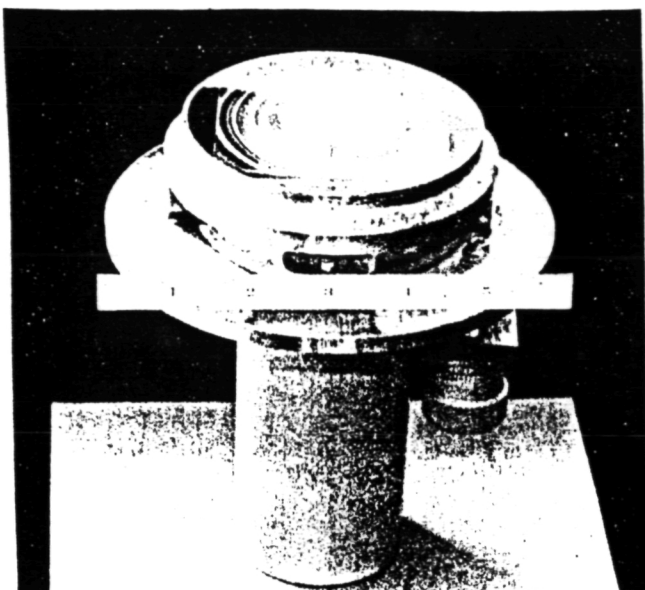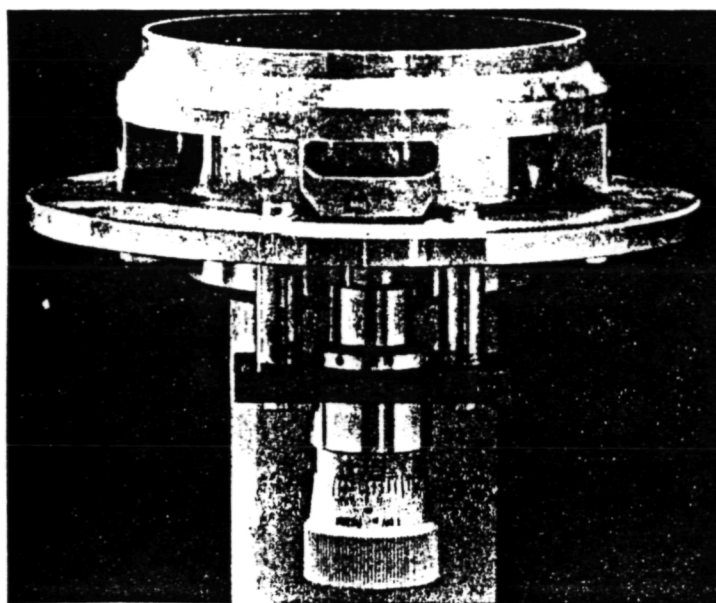
(a)   (b)

Figure 3. (a)   3600 grooves mm^{-1} grating replicated on an elastically deformable
                substrate.
   (b)   Closeup showing the deforming actuator.

Table 1.   Characteristics of the Toroidal Replica Grating

Substrate: Toroid on stiff blank
Radius of curvature: 1 meter
Toroid Aspect Ratio (R_h/R_v): 0.978
Ruling Frequency: 3600 grooves mm^{-1}
Ruled area: 70 x 70 mm^2
First order blaze wavelength: 600 Å

Test Results

Initial tests of the imaging properties of the toroidal grating at EUV wavelengths
were carried using a specially designed laboratory spectrometer. Spectral images from a
line of ten pinholes arranged along the entrance slit and illuminated by a low-voltage,
low-pressure spark-discharge source were recorded on photographic film. The pinholes were
drilled in aluminum foil with a laser and had diameters ranging from 10 to 33 microns. The
distance between adjacent pinholes was 500 microns. The EUV spectral images of the
pinholes recorded on Schumann emulsion located along the Rowland circle are shown in
Figure 4a. The stigmatic focus points are marked by arrows.

Densitometer measurements of these photographic images showed that the spatial
variation of the blur dimensions was essentially in agreement with that predicted from the
ray trace analyses[2] (see Figure 4b).
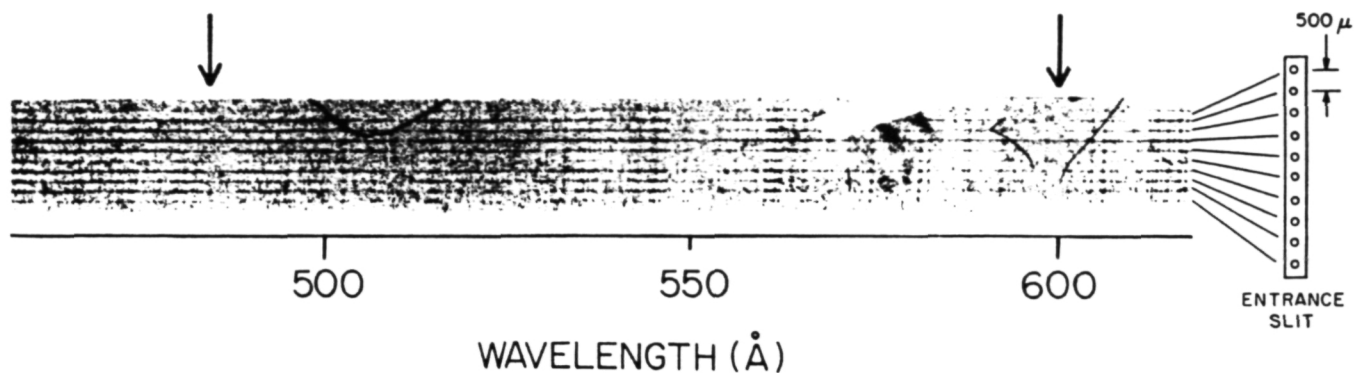
WAVELENGTH (Å)

(a)
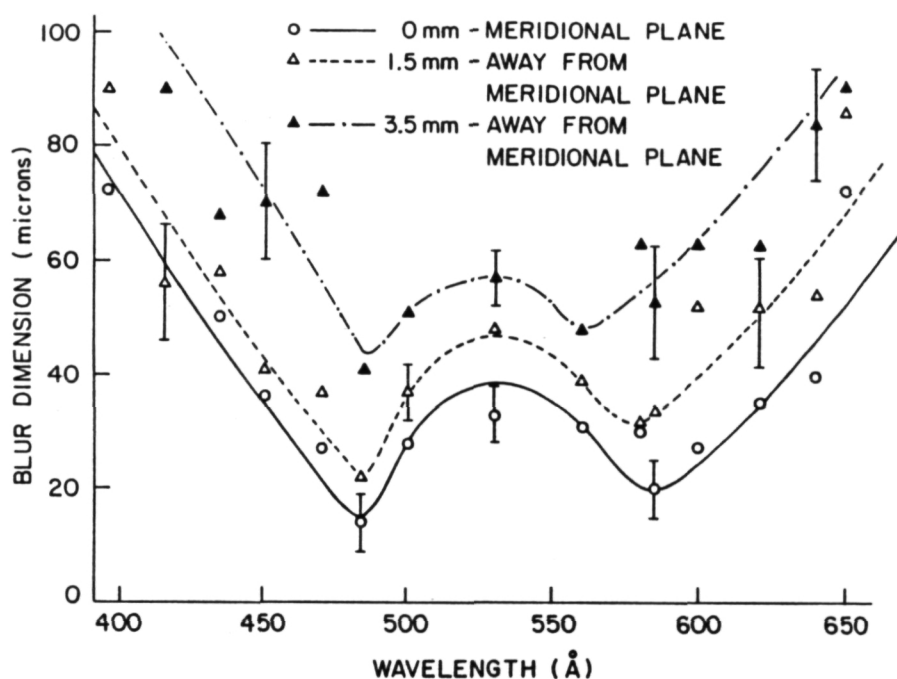
(b)

Figure 4. (a) Spectral images of ten pinholes arranged along the spectrometer
             entrance slit illuminated by a low-voltage, low-pressure spark
             source. The arrows indicate the stigmatic wavelengths.
          (b) Spatial blur dimensions determined from the photographic spectra.

    Because of the difficulties asociated with the analysis of the non-linear intensity
data in the photographic images, data were also recorded at the wavelength of the He I
resonance line at 584 Å with an imaging photoelectric detector system with a linear
response. For these tests a dc hollow-cathode light source was employed. The photographic
plate holder was replaced with a tetraphenyl-butadiene phosphor mounted on the Rowland
circle. This phosphor down-converts EUV photons into visible-light photons with a peak
emission near 4300 Å.[5] The visible-light images were viewed through a window in the
vacuum tank and re-imaged and magnified by approximately a factor of three onto the photo-
cathode of a visible-light Multi-Anode Microchannel Array (MAMA) detector tube[6] using the
optical system shown in the schematics in Figure 5.
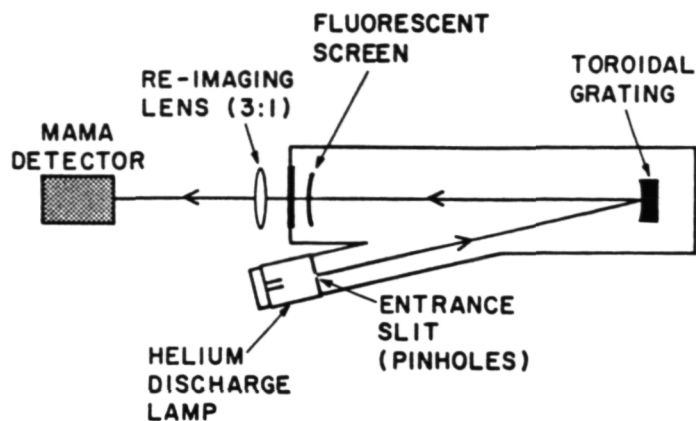
(a)
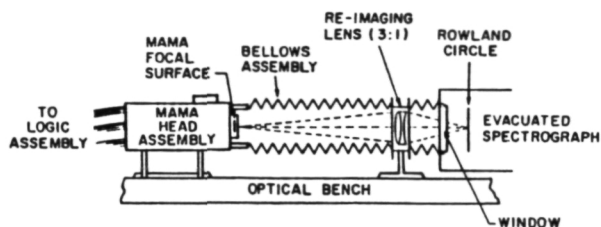
(b)

Figure 5. (a) Schematic of the optical system for photoelectric tests of the toroidal
               grating.
           (b) Detail of the re-imaging system and detector assembly.

As shown in Figure 6, the imaging MAMA detector tube employs a bi-alkali semi-transparent
photocathode in proximity focus with a high-gain curved-channel microchannel plate (MCP)
and has a format of (256 x 1024)-pixels with pixel dimensions of 25 x 25 microns^2. The
two-dimensional digital images obtained from the MAMA detector in the laboratory were
recorded on a portable data handling and display system.
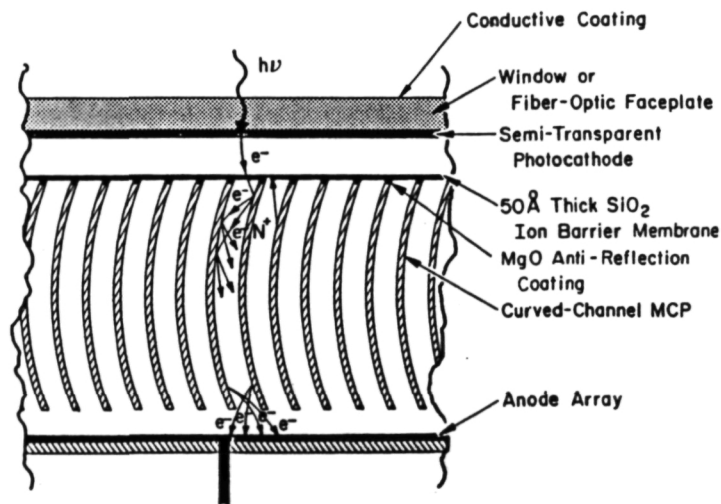
(a)
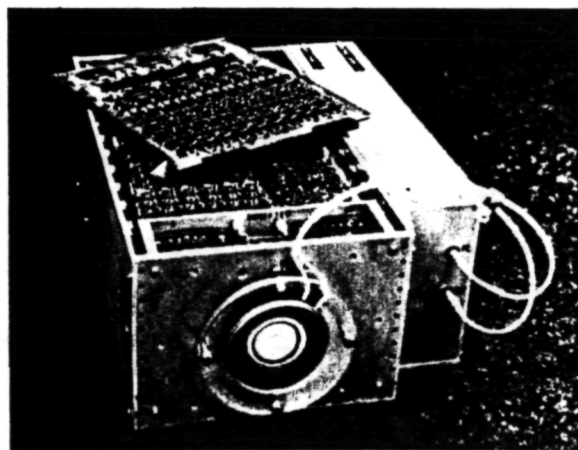
(b)

Figure 6. (256 x 1024)-pixel MAMA detector system.

           (a) Schematic of detector tube.
           (b) Detector head assembly.

A one-dimensional cut through the line of ten pinholes along the entrance slit at the
wavelength of 584 Å is shown in Figure 7. A two-dimensional image showing the self-
reversal of the He I 584 Å resonance line is shown in Figure 8. Because of the low
transfer efficiency of the phosphor and the lens system, it was only possible in these
initial tests to record images at the wavelength of the strong He I resonance line. In
order to determine the modulation transfer function of the phosphor and the lens system
after the EUV images had been recorded, the pinholes were attached to the phosphor and
back-illuminated by an incandescent lamp. Deconvolution of the two sets of pinhole images
showed that the maximum spatial blur dimensions were below 25 microns as predicted from
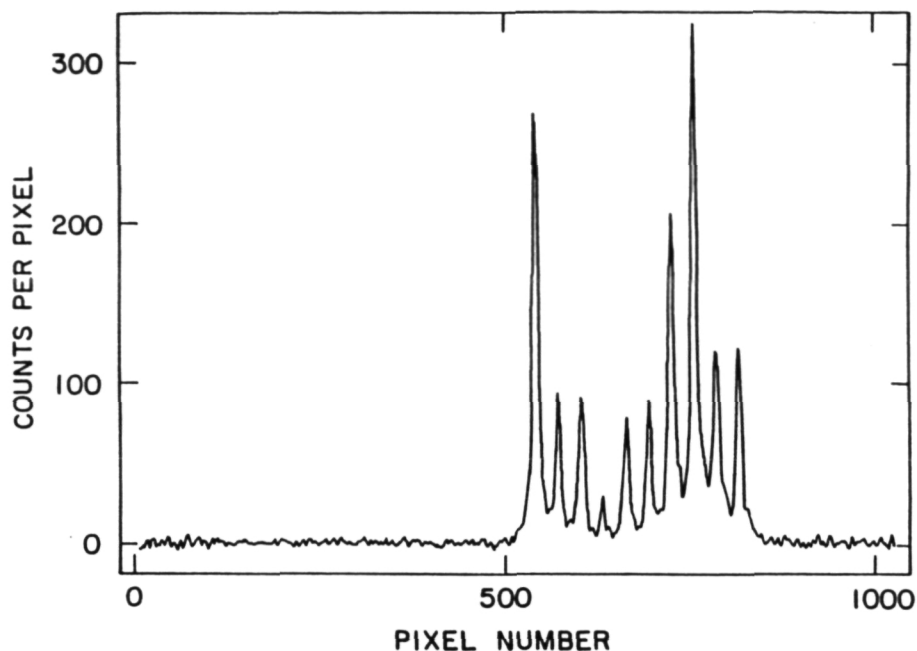the ray trace analyses. Detailed analyses of these data are currently in progress.

Figure 7. One-dimensional image at the wavelength of the He I resonance line at 584 Å of ten pinholes located along the spectrometer entrance slit. The intensity variations are the result of the different pinhole diameters which range from 10 to 33 microns.
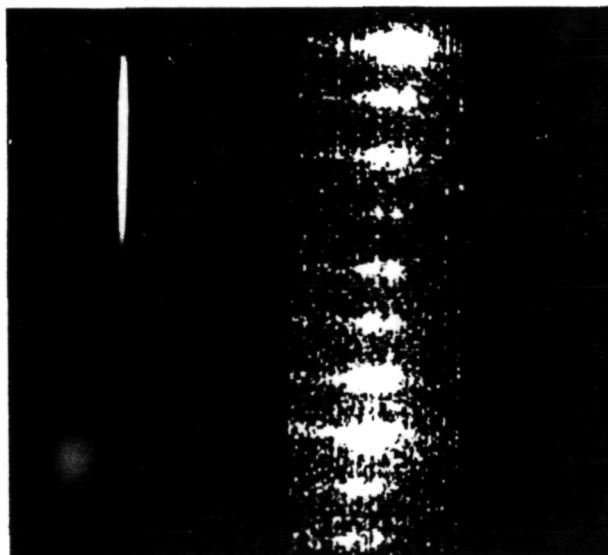
Figure 8. Two-dimensional image of the self-reversed He I 584 Å resonance line produced by the hollow-cathode light source.

Summary

Initial tests have shown that a single toroidal diffraction grating produced by a simple procedure utilizing an elastically deformable substrate has excellent imaging characteristics at EUV wavelengths. More detailed tests of the imaging properties of the toroidal grating over a wider range of wavelengths will be undertaken shortly with an open-structure version of the two-dimensional (256 x 1024)-pixel MAMA detector system. Studies will also be initiated to define ways of providing higher-order aberration corrections in fast systems. It now appears that diffraction gratings fabricated by this technique will be of use in a number of space astrophysics missions including the European Space Agency (ESA) Solar and Heliospheric Observatory (SOHO) and the NASA/ESA EUV spectro-scopic mission called Lyman.

Acknowledgements

References

1. Huber, M. C. E. and Tondello, G., "Stigmatic Performance of an EUV Spectrograph with a Single Toroidal Grating," Applied Optics 18, p. 3948, 1979.
2. Haber, H., "The Torus Grating," J. Opt. Soc. Amer. 40, p. 153, 1950.
3. Huber, M. C. E., Jannitti, E., Lemaître, G., and Tondello, G., "Toroidal Grating Obtained on an Elastic Substrate," Applied Optics 20, p. 2139, 1981.
4. Hyperfine, Inc., 1930 Central Avenue, Suite B, Boulder, CO 80301, (303) 444-6882.
5. Burton, W. M., and Powell, B. A., "Fluorescence of Tetraphenyl-Butadiene in the Vacuum Ultraviolet," Applied Optics 12, p. 87, 1973.
6. Timothy, J. G., "Multi-anode Microchannel Array Detector Systems: Performance Characteristics," Optical Engineering 24, p. 1066, 1985.

Imaging extreme ultraviolet spectrometer employing a single toroidal diffraction grating: the initial evaluation

M. C. E. Huber, J. G. Timothy, J. S. Morgan, G. Lemaitre, G. Tondello, E. Jannitti, and P. Scarin

A high-efficiency extreme ultraviolet (EUV) imaging spectrometer has been constructed and tested. The spectrometer employs a concave toroidal grating illuminated at normal incidence in a Rowland circle mounting and has only one reflecting surface. The toroidal grating has been fabricated by a new technique employing an elastically deformable submaster grating which is replicated in a spherical form and then mechanically distorted to produce the desired aspect ratio of the toroidal surface for stigmatic imaging over the selected wavelength range. The fixed toroidal grating used in the spectrometer is then replicated from this surface. Photographic tests and initial photoelectric tests with a 2-D pulse-counting detector system have verified the image quality of the toroidal grating at wavelengths near 600 Å. The results of these initial tests are described in detail, and the basic designs of two instruments which could employ the imaging spectrometer for astrophysical investigations in space are briefly described, namely, a high-resolution EUV spectroheliometer for studies of the solar chromosphere, transition region, and corona and an EUV spectroscopic telescope for studies of nonsolar objects.

I. Introduction

The extreme ultraviolet (EUV) spectral region at wavelengths below ~1200 Å is of critical importance for the diagnostics of conditions in high-temperature plasmas, since this region contains emission lines and continua characteristic of temperatures in the range from ~10^4 to >10^6 K. This spectral region is thus particularly useful for studies of dynamic phenomena in the outer atmosphere of the sun and other stars. In addition, observations at these wavelengths can provide unique astrophysical data on dynamic phenomena in planetary atmospheres and magnetospheres, on the exchange of matter and energy between stars and the interstellar medium, on the variations of light ele-

ment abundances in the galaxy, and on the dynamics of the hot interstellar gas in galactic halos.

Because of the lack of window materials and of high-reflectivity optical surfaces at these wavelengths, practical systems for imaging and spectroscopy must employ open-structure detector systems and a minimum of reflecting surfaces. The recent development of high-resolution imaging detector systems which can operate with high efficiency at EUV wavelengths has stimulated the design of optical systems which can provide a stigmatic spectroscopic capability. These imaging spectrometer systems can provide the simultaneous spectral, spatial, and temporal resolutions required for many scientific observations that have not been previously possible. In this paper we describe the fabrication and results of initial tests of a toroidal diffraction grating for use in an imaging EUV spectrometer at wavelengths between 300 and 1200 Å.

II. Spectrometer Design

The design of the spectrometer was stimulated initially by the need for high-time-resolution observations of the solar chromosphere, transition region, and corona with a high spectral resolution ($\lambda/\Delta\lambda \sim 2 \times 10^4$) and a spatial resolution of 1 sec of arc or better.[1] The basic configuration of the spectrometer mounting is shown in Fig. 1(a).

In the conventional Rowland circle mounting, the vertical and horizontal foci from a spherical diffraction

M. C. E. Huber is with the European Space Agency, ESTEC, Space Science Department, P.O. Box 299, Noordwijk NL-2200, The Netherlands; J. G. Timothy and J. S. Morgan are with Stanford University, Center for Space Science & Astrophysics, Stanford, California 94305; G. Lemaitre is with Marseilles Observatory, 2 place Le Verrier, F-13004 Marseilles, France; G. Tondello is with the University of Padua, Department of Electronics & Information, 6A via Gradenigo, I-35100 Padua, Italy; E. Jannitti and P. Scarin are with CNR Istituto Gas Ionizzati, 6A via Gradenigo, I-35100 Padua, Italy.

PRECEDING PAGE BLANK NOT FILMED

TOROIDAL DIFFRACTION GRATING

SPATIAL FOCAL SURFACE

ENTRANCE SLIT

STIGMATIC POINT

STIGMATIC POINT

SPECTRAL FOCAL SURFACE (ROWLAND CIRCLE)

(a)

ROWLAND CIRCLE

TOROIDAL GRATING

SPATIAL FOCAL PLANE
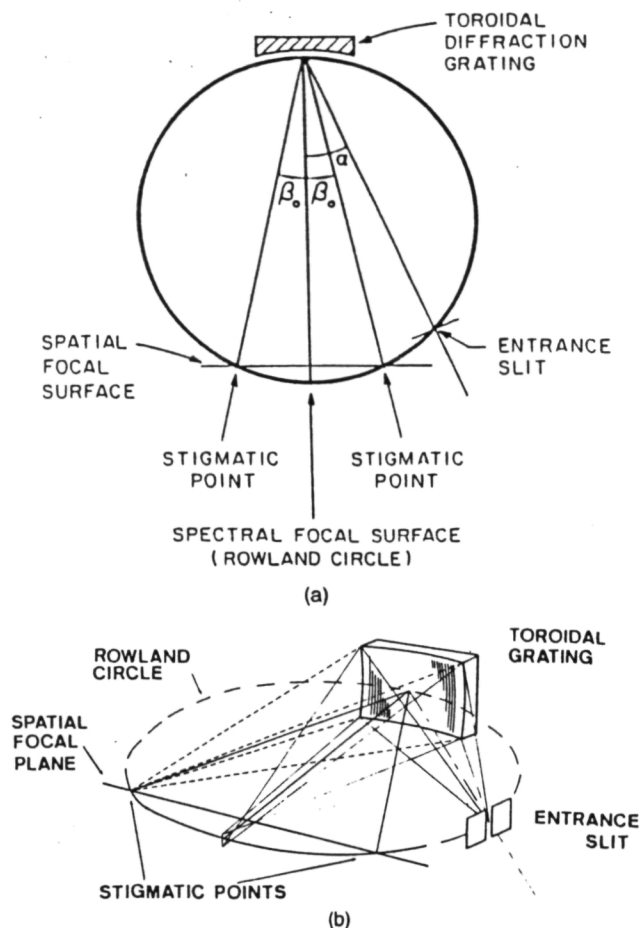
ENTRANCE SLIT

STIGMATIC POINTS

(b)

Fig. 1. (a) Schematic of the imaging EUV spectrometer employing a single toroidal grating. Exact stigmatic focusing is obtained at angles of diffraction $\pm\beta_0$, which are defined by Eq. (1). Given a sufficiently small value of β_0 and some depth of focus, effective stigmatic focusing can be achieved between and somewhat beyond the two stigmatic points. (b) Isometric display of the imaging properties at the two stigmatic points $\pm\beta_0$.
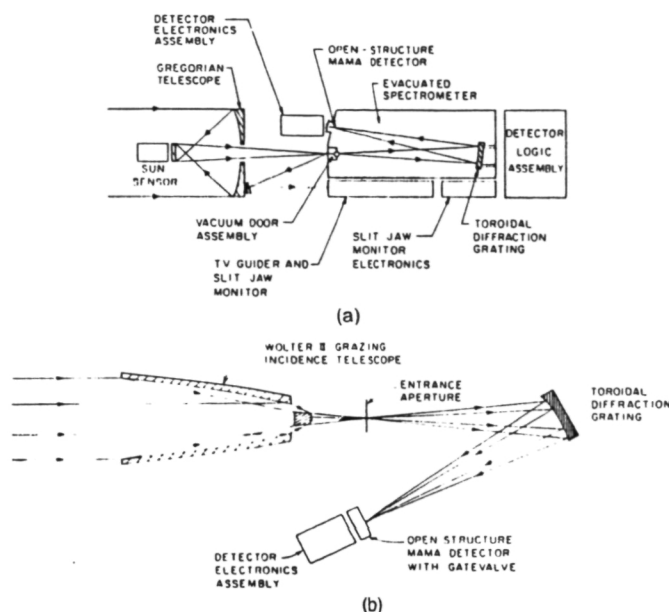

(a)

(b)

Fig. 2. Schematics of telescope and imaging spectrometer systems: (a) high-resolution EUV spectroheliometer using a Gregorian telescope; (b) grazing-incidence telescope and normal-incidence spectrograph combination for astrophysical studies at wavelengths below 1200 Å.

grating are not coincident. However, Haber[2] has pointed out that it is possible to obtain exact stigmatic focusing at two points in the spectrum by selecting the vertical radius of curvature R_v of a toroidal grating to be smaller than its horizontal radius R_h. As shown in Fig. 1(a), exact stigmatic focusing can then be obtained at two positions in the spectrum given by

$$R_v = R_h \cos\alpha \, \cos\beta_0. \tag{1}$$

The two stigmatic points are located symmetrically to the grating normal at the angles of diffraction $\pm\beta_0$, as shown in Fig. 1(a). An isometric display of the imaging properties of the two stigmatic points is shown in Fig. 1(b).

In a practical system where β_0 is small and there is some depth of focus (moderate speed systems with focal ratios $</f/15$), stigmatic focusing can be achieved between and somewhat beyond the two stigmatic points with a simple toroidal surface. Ray tracing studies[1] have shown for a 3600-groove mm^{-1} grating with a radius of curvature of 2000 mm, blur sizes of significantly <40 μm can be obtained over an effective

wavelength range of >100 Å. However, for higher speed systems ($f/10$ or faster), which will be required for astrophysical studies, corrections for higher-order aberrations are required.[3]

A number of high-efficiency EUV imaging spectrographic systems can be constructed using this type of diffraction grating. For example, as shown in Fig. 2(a), the toroidal grating spectrograph can be combined with a normal-incidence Gregorian telescope to produce a high-resolution EUV spectroheliometer for high-spatial-resolution studies of the solar chromosphere, transition region, and corona. Alternatively, as shown in Fig. 2(b), the toroidal grating spectrograph can be combined with a Wolter type II grazing-incidence telescope for astrophysical studies at wavelengths below 1200 Å.

III. Grating Fabrication

To evaluate the performance characteristics of a toroidal grating at EUV wavelengths, we fabricated a toroidal replica grating using a unique technique developed by Lemaitre.[4] This technique uses an elastically deformable grating which is replicated from a spherical master ruling. The ratio of the vertical and horizontal radii of curvature can then be set to any desired value by applying a distorting force to the flexible substrate. The stainless steel flexible substrate (see Fig. 3) has a form which elastically deforms into an exact toroidal surface with the application of a single adjustable distorting force.[5] The grating, with a ruling frequency of 3600 grooves mm^{-1}, and an active area of 70 × 70 mm^2 was replicated onto the deformable concave substrate by Hyperfine, Inc.,[6] from a concave spherical master ruling using an intermediate
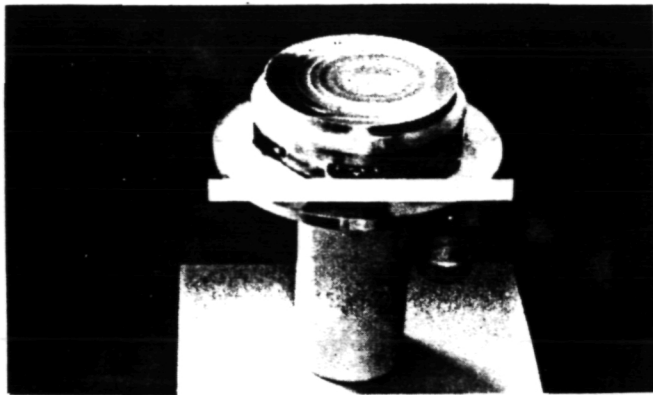
(a)
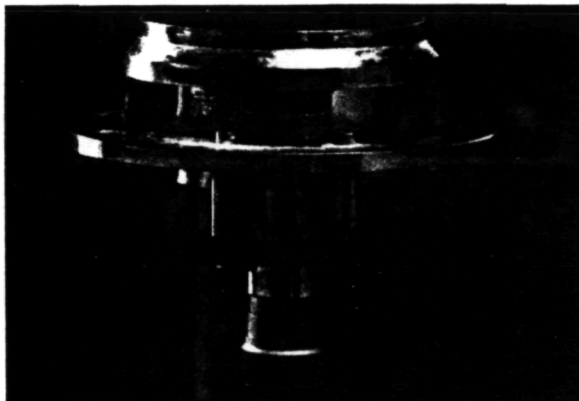
(b)

Fig. 3. (a) 3600 grooves mm^{-1} grating replicated on an elastically deformable substrate; (b) close-up showing the deforming actuator (a differential micrometer).

Fig. 4. Form of the elastically deformable substrate. Forces are applied at the indicated points.

convex replicating surface. A radius of curvature of 1000 mm was selected for the initial grating for convenience in laboratory testing. After the substrate had been deformed to the appropriate aspect ratio, a fixed concave toroidal grating was replicated from the deformable substrate, again using an intermediate convex replicating surface. The way in which the forces are applied to the deformable substrate is shown in Fig. 4.

The aspect ratio of the toroidal surface was determined in two ways: first, by using a modified laser-illuminated Martin-Watt-Weinstein version of the Twyman-Green interferometer[7-9] and, second, by determining the angle for stigmatic imaging in the zeroth order. The setup of the modified Martin-Watt-Weinstein interferometer with unequal path lengths is shown in Fig. 5(a). The reference surface was a concave spherical mirror with a radius of curvature of 400 mm. If the grating were spherical, the wavefronts from both the reference and grating surfaces would be identical (spherical) producing a uniform illumination in the recombined beam. When the grating figure is toroidal, a saddle surface is superimposed on the sphere, and, accordingly, fringes exhibit a saddle path in the recombined beam over the projection of the test surface. The maximum deviation of the grating sur-
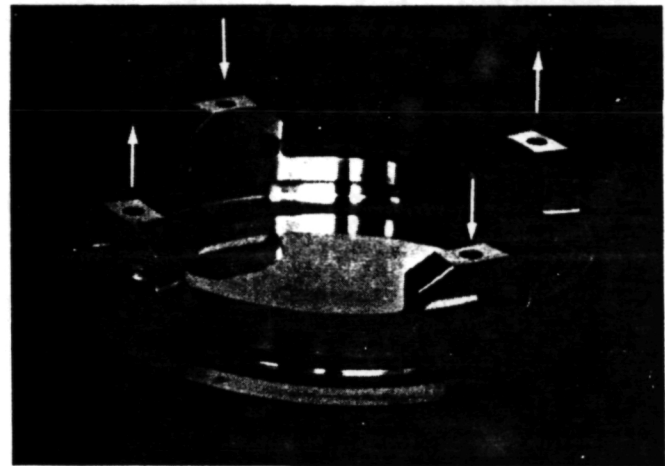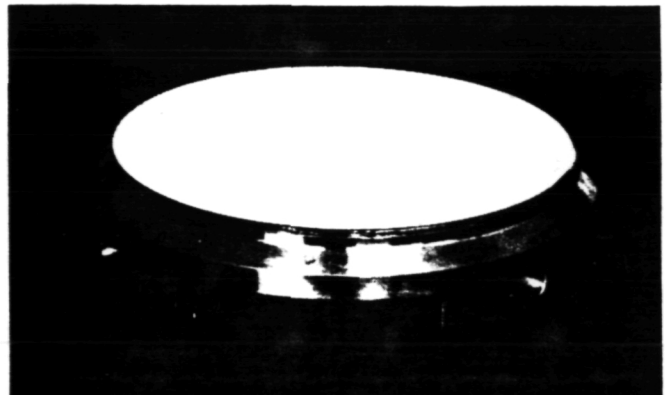
face from a sphere occurs in the directions where there are the greatest number of fringes from the center to the edge. In these directions the difference in height between the toroid and the reference sphere is equal to $(N\lambda)/2$, where N is the number of fringes from the center to the edge and λ is the wavelength of the laser (6325 Å). The total deviation Δ across the complete toroidal surface is then given by $\Delta = (2N\lambda)/2$, where

$$\Delta = h_v - h_h = \frac{a^2}{2}\left(\frac{1}{R_v} - \frac{1}{R_h}\right) \sim \frac{a^2}{2R^2}(R_h - R_v),$$

with a the halfwidth of the grating and R the mean radius of curvature of the grating.

The aspect ratio R_v/R_h is then determined from

$$\frac{R_v}{R_h} = \frac{R - \left(\dfrac{R_h - R_v}{2}\right)}{R + \left(\dfrac{R_h - R_v}{2}\right)} = \frac{1 - \dfrac{R}{a}\Delta}{1 + \dfrac{R}{a}\Delta} = \frac{a - R\Delta}{a + R\Delta}. \qquad (2)$$

The second measurement technique is shown in the schematic in Fig. 5(b). Since from Eq. (1),

$$\frac{R_v}{R_h} = \cos\alpha \, \cos\beta_0, \qquad (3)$$

it follows that for the symmetrical case of stigmatic imaging in zeroth order, where $\alpha = \beta_0 = \gamma$,
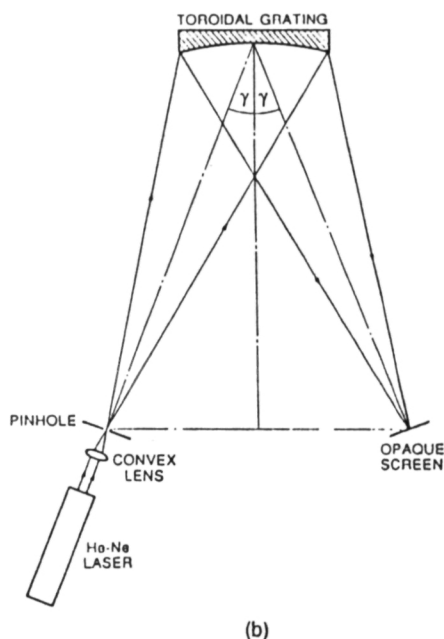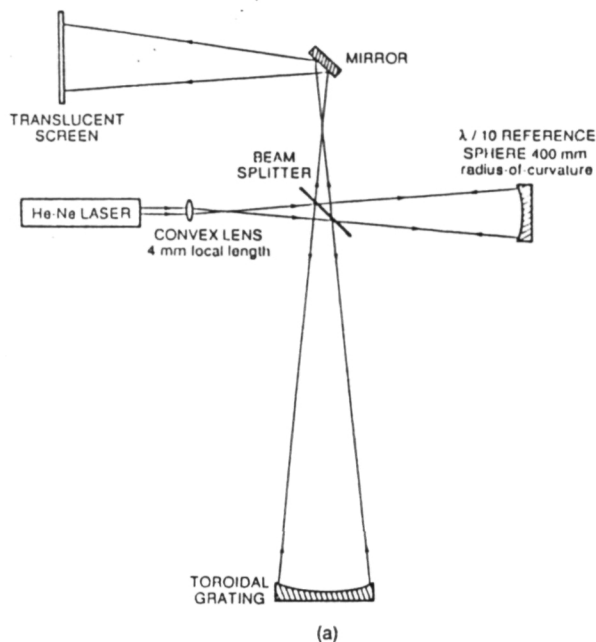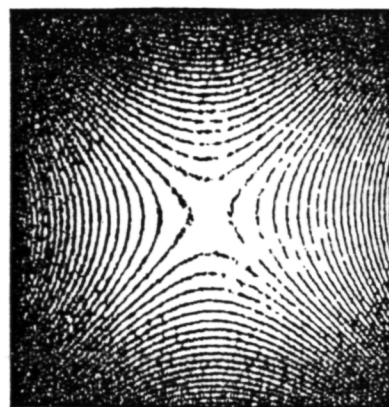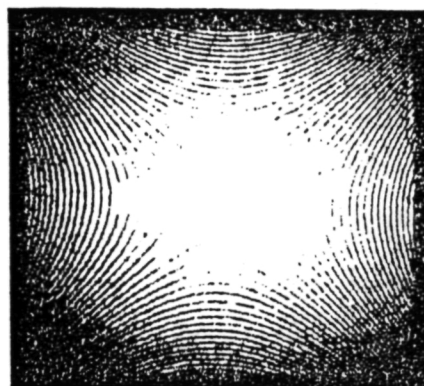
Fig. 5. (a) Schematic of the modified Martin-Watt-Weinstein interferometer for the determination of the aspect ratio of the toroidal grating surface. (b) Schematic showing the zeroth-order technique for measurement of the aspect ratio of the toroidal grating surface.

(a)

(b)

Fig. 6. Saddle fringe pattern produced by toroidal grating 3: (a) before thermal vacuum test; (b) after thermal vacuum test.

$$\frac{R_v}{R_h} = \cos^2\gamma. \qquad (4)$$

The angle of reflection γ is determined by measuring the position of the best focus for the 1:1 image of a pinhole.

The desired characteristics of the grating for imaging at wavelengths near 600 Å are given in Table I. Three toroidal replica gratings have been fabricated to date. The symmetry of the toroidal surface was excellent in all cases as shown by the uniformity of the classic saddle fringe pattern (see Fig. 6). Since toroidal gratings have been identified for possible use on the ESA/NASA Solar and Heliospheric Observatory (SOHO) mission and the Lyman EUV Spectroscopic Explorer mission, the grating was subjected to a thermal vacuum test over the temperature range from −20 to +40°C. No change in the aspect ratio was observed, as can be seen from a comparison of Figs. 6(a) and (b). The estimated uncertainty of these measurements was less than ±1 fringe.

The results from both measurement techniques agreed to within the experimental error. The first grating received from Hyperfine, Inc. had too low an aspect ratio of 0.9892, which would produce stigmatic images on the normal at wavelengths near 410 Å when used at an angle of incidence of 8°.43. However, the

Table I. Desired Characteristics of the Test Toroidal Diffraction Grating

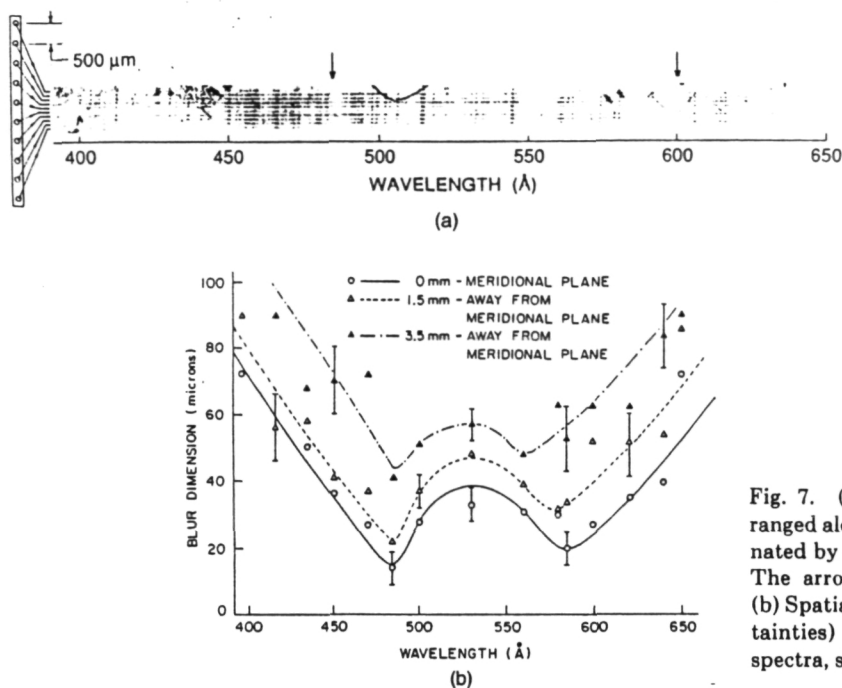|	
Wavelengths and angles of rays	
Stigmatic wavelength range	520–630 Å (first order)
Angle of incidence α	11.947°
Wavelength on grating normal ($\beta = 0°$)	575 Å
Wavelength at stigmatic ponts	
($\beta_0 = \pm0.825°$)	535 Å, 615 Å
Grating surface	
Horizontal radius of curvature R_h	1011.1 mm
Vertical radius of curvature R_v	989.1 mm
Aspect ratio R_v/R_h	0.9782
Ruling frequency	3600 grooves mm^{-1}
Ruled area	70 × 70 mm^2

(a)

(b)

Fig. 7. (a) Spectral images of ten pinholes arranged along the spectrometer entrance slit illuminated by a low-voltage low-pressure spark source. The arrows indicate the stigmatic wavelengths. (b) Spatial blur dimensions (with estimated uncertainties) as determined from the photographic spectra, shown in comparison with the ray-tracing results.

second and third replicas were essentially identical with aspect ratios of 0.9809 close to the desired value of 0.9782. The reasons for the lower than expected aspect ratios are currently being investigated with Hyperfine, Inc. At an angle of incidence of 11°.2 the wavelength on the grating normal is 540 Å, and an acceptable imaging performance over the wavelength range from 520 to 630 Å was obtained by slightly changing the angle of incidence.

IV. Test Results

Initial tests of the imaging properties of the toroidal grating at EUV wavelengths were carried out using a specially designed laboratory spectrometer. First, spectral images from a line of ten pinholes arranged along the entrance slit and illuminated by a low-voltage low-pressure spark-discharge source were recorded on photographic film. The pinholes were drilled in aluminum foil with a laser and had diameters ranging from 10 to 33 μm. The distance between adjacent pinholes was 500 μm. The EUV spectral images of the pinholes recorded on Schumann emulsion located along the Rowland circle are shown in Fig. 7(a). The stigmatic focus points are marked by arrows. Densitometer measurements of these photographic images show that the spatial variation of the blur dimensions agrees with that predicted from the ray trace analyses[1] [see Fig. 7(b)].

Because of the difficulties associated with the analysis of the nonlinear intensity data in the photographic images, data were also recorded at the wavelength of the He I resonance line at 584 Å with an imaging photoelectric detector system having a linear response. For these tests a dc hollow-cathode light source was employed. The photographic plate was replaced with a tetraphenyl-butadiene phosphor applied to a glass plate mounted on the Rowland circle. This phosphor
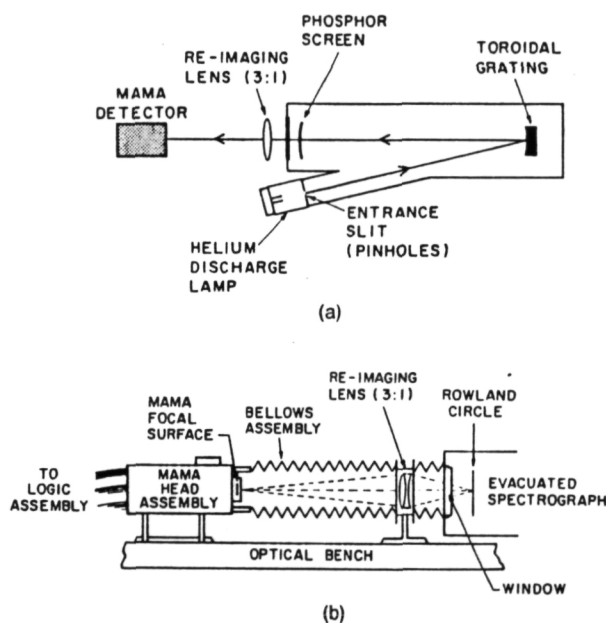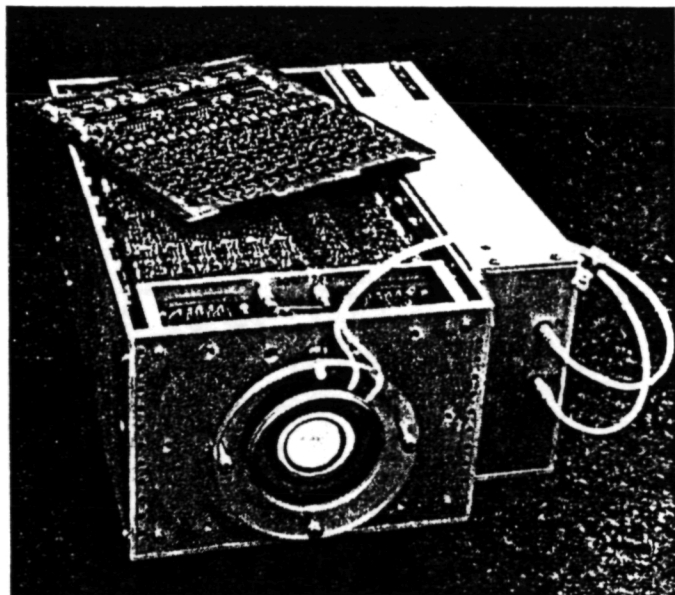

(a)

(b)

Fig. 8. (a) Schematic of the optical system for the initial photoelectric tests of the toroidal grating. (b) Detail of the reimaging system and detector assembly.

downconverts EUV photons into visible-light photons with a peak emission near 4300 Å.[10] The visible-light images were viewed through a window in the vacuum tank and reimaged and magnified by a factor of ~3 onto the photocathode of a visible-light multi-anode microchannel array (MAMA) detector tube[11] using the optical system shown in the schematics in Fig. 8.

As shown in Fig. 9(a), the imaging visible-light MAMA detector tube employs a bialkali semitransparent photocathode in proximity focus with a high-gain curved-channel microchannel plate (MCP) and has a readout anode array of precision electrodes to
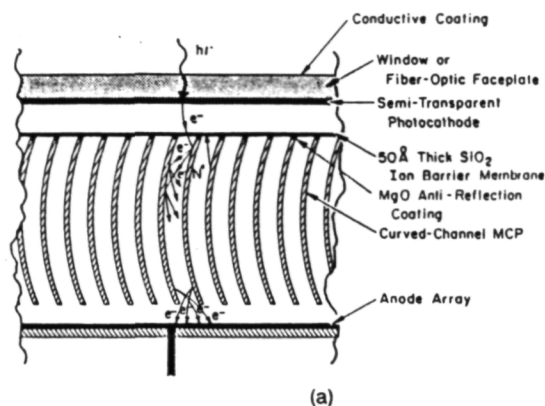
(a)

(b)

Fig. 9. (256 × 1024)-pixel MAMA detector system: (a) schematic
of detector tube; (b) detector head assembly.

Fig. 10. One-dimensional image at the wavelength of the He I
resonance line at 584 Å of ten pinholes located along the spectrome-
ter entrance slit. The different pinhole diameters (ranging from 10
to 33 μm) result in different peak intensities.

(a)

(b)

Fig. 11. (a) Comparison of the pinhole and phosphor image profile
with the image from the complete optical system including the
diffraction grating. Solid line, pinhole and phosphor profile;
dashed line, profile recorded with the toroidal grating. (b) Compar-
ison of convolved pinhole image with the image from the toroidal
grating.

produce a format of 256 × 1024 pixels with pixel di-
mensions of 25 × 25 μm^2. The complete detector head
assembly is shown in Fig. 9(b). Details of the readout
array have been described recently by Timothy.[12]
The detector operates as a pulse-counting system with
zero readout noise. The dark count from the bialkali
photocathode at room temperature was of the order of
5 counts s^{-1} for the whole array. For these measure-
ments a set of pinholes with separations of 250 μm was
employed. The magnifying optics gave an effective
spatial resolution for each detector pixel of ~8 μm on
the Rowland circle of the spectrograph. The 2-D digi-
tal images obtained from the MAMA detector in the
laboratory were recorded on a portable data handling
and display system.

A 1-D cut through the line of ten pinholes along the
entrance slit at the wavelength of 584-Å resonance line
is shown in Fig. 10. Because of the low transfer effi-
ciency of the phosphor and the lens system, it was only
possible in these initial tests to record images at the
wavelength of the strong He I resonance line. To
determine the modulation transfer function of the
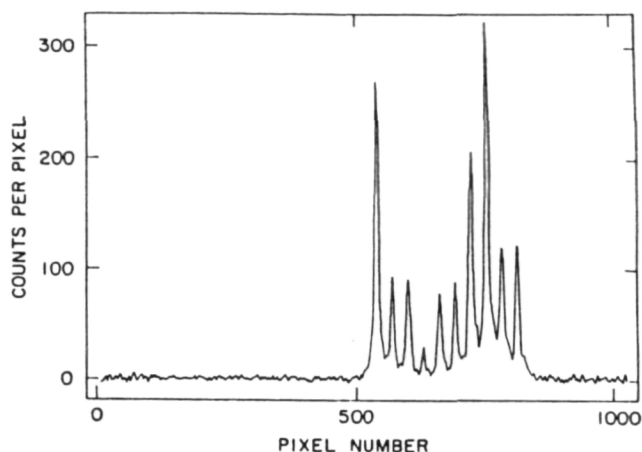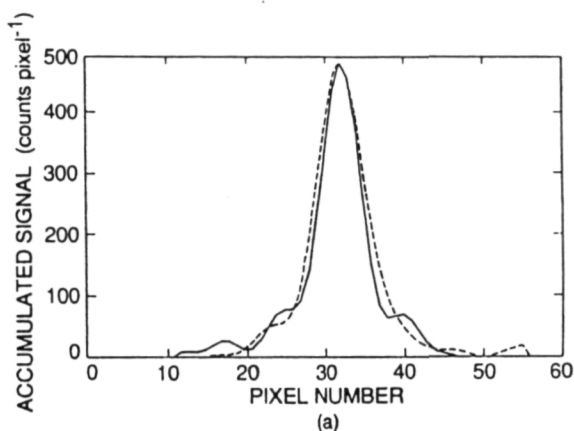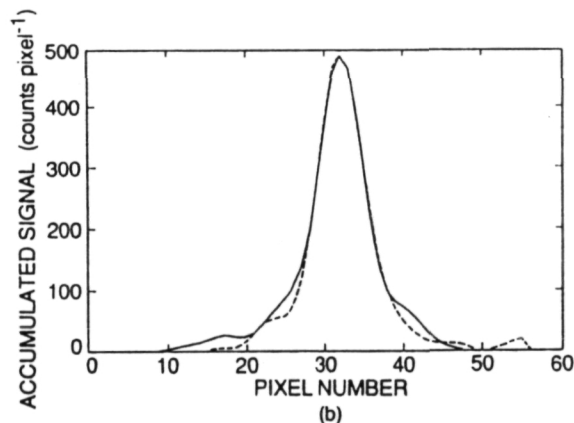phosphor and the lens system after the EUV images

had been recorded, the pinholes were attached to the
phosphor and backilluminated by an incandescent
lamp. The two image profiles are shown in Fig. 11(a).
Convolution of the two sets of images show that the
maximum spatial blur dimensions introduced to the
toroidal grating are below 25 μm as predicted from the
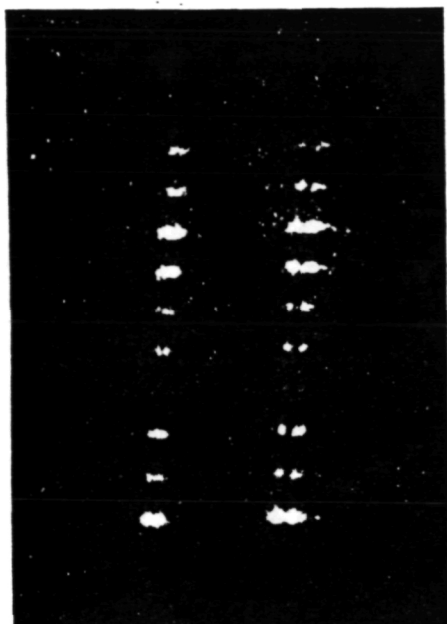ray trace analyses. The convolved image of the pin-

Fig. 12. Spectral images of the ten pinholes showing the self-reversal of the He I 584-Å resonance line with different gas pressures in the light source. Left, low gas pressure; right, high gas pressure. Good imaging is achieved although the line of pinholes is skew with respect to the normal to the plane of dispersion.
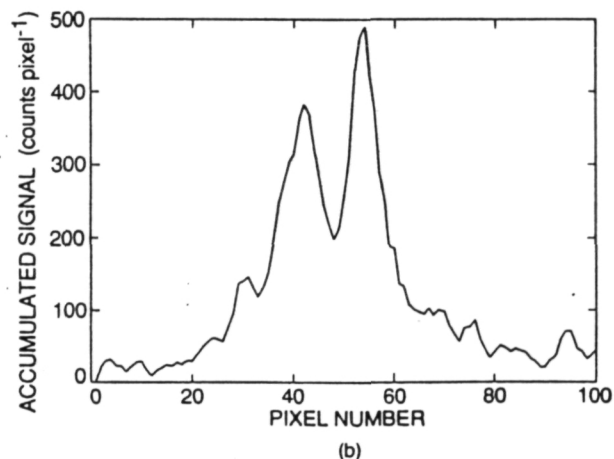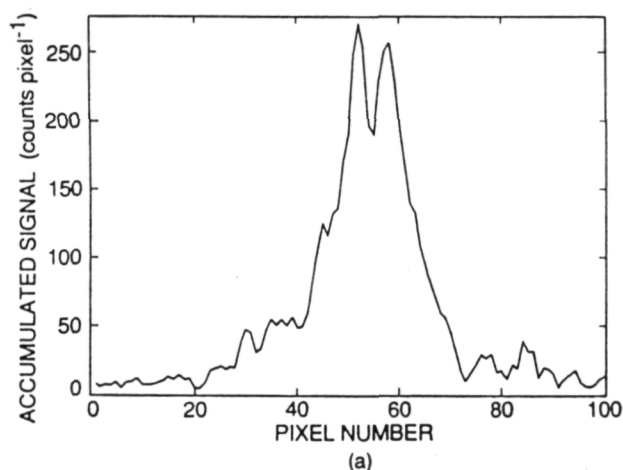

(a)

(b)

Fig. 13. Spectral images from one pinhole showing the width and depth of the self-reversal of the He I 584-Å resonance line: (a) low gas pressure; (b) high gas pressure.

hole image compared with the grating image is shown in Fig. 11. On a root-sum-square basis the spatial aberrations introduced by the grating at this wavelength are calculated to be ~16 μm (FWHM).

Two-dimensional images recorded with the MAMA detector showing the self-reversal of the He I 584-Å resonance line for two different gas pressures in the light source are shown side by side in Fig. 12. The difference in the linewidths for one of the pinhole images when the hollow cathode lamp is run at low and high gas pressures is shown in Fig. 13. The measured difference in the linewidths is 0.14 Å (FWHM). As the depth and width of the self-reversal are not known the spectral resolution could not be determined in these tests. An estimate of the saturated self-reversed part of the profile leads to a width of 19 mÅ, corresponding to ~7 μm on the Rowland circle. Zero intensity in the self-reversed part of the line profile would not be expected, given the calculated aberrations and measured modulation transfer of the phosphor–lens system.

V. Summary

Initial tests have shown that a single toroidal diffraction grating produced by a simple procedure utilizing an elastically deformable substrate has excellent imaging characteristics at EUV wavelengths. More detailed tests of the imaging properties of the toroidal grating over a wider range of wavelengths will be undertaken shortly with an open-structure version of the 2-D (256 × 1024)-pixel MAMA detector system, using a laboratory spectrograph which is now under construction at the University of Padua. Studies have also been initiated to define ways of providing corrections for higher-order aberrations in fast systems ($f/10$ of lower), using an elastically deformable substrate with a more complex configuration.

References

1. M. C. E. Huber and G. Tondello, "Stigmatic Performance of an EUV Spectrograph with a Single Toroidal Grating," Appl. Opt. 18, 3948 (1979).
2. H. Haber, "The Torus Grating," J. Opt. Soc. Am. 40, 153 (1950).
3. W. C. Cash, Jr., "Aspheric Concave Grating Spectrographs," Appl. Opt. 23, 4518 (1984).
4. G. Lemaitre, "Coma and Astigmatism Compensated by Elastic Relaxation on Each Mirror Pair of a Two-Mosaic Telescope," in Optical Telescopes of the Future, F. Pacini, W. Richter, and R. N. Wilson, Eds. (European Southern Observatory, Garching bei munchen, 1978), p. 321.

5. M. C. E. Huber, E. Jannitti, G. Lemaitre, and G. Tondello, "Toroidal Grating Obtained on an Elastic Substrate," Appl. Opt. **20**, 2139 (1981).

6. Hyperfine, Inc., 4946 North 63rd St., Boulder, CO 80301, (303) 530-0709.

7. M. Born and E. Wolf, *Principles of Optics* (Pergamon, New York, 1980), p. 303.

8. M. Françon, *Optical Interferometry* (Academic, New York, 1966), p. 202.

9. S. Johansson and U. Litzen, "Analysis of 4d–4f Transitions in Fe II," Phys. Scr. **10**, 121 (1974).

10. W. M. Burton and B. A. Powell, "Fluorescence of Tetraphenyl-Butadiene in the Vacuum Ultraviolet," Appl. Opt. **12**, 87 (1973).

11. J. G. Timothy, "Multi-Anode Microchannel Array Detector Systems: Performance Characteristics," Opt. Eng. **24**, 1066 (1985).

12. J. G. Timothy, "Imaging at Soft X-Ray Wavelengths with High-Gain Microchannel Plate Detector Systems," Proc. Soc. Photo-Opt. Instrum. Eng. **691**, 35 (1986).

EXTREME ULTRAVIOLET
ASTRONOMY

A SELECTION OF
PAPERS PRESENTED AT THE
FIRST BERKELEY COLLOQUIUM ON
EXTREME ULTRAVIOLET ASTRONOMY

University of California, Berkeley
January 19–20, 1989

□ □ □

Co-Sponsored by
IAU Commissions 29, 44, and 48

EDITED BY

ROGER F. MALINA
Center for EUV Astrophysics
University of California, Berkeley

STUART BOWYER
Astronomy Department and
Center for EUV Astrophysics
University of California, Berkeley

A HIGH EFFICIENCY IMAGING
EXTREME ULTRAVIOLET SPECTROMETER

JEFFREY S. MORGAN
DAVID C. SLATER
GIUSEPPE TONDELLO
GIAMPIERO NALETTO
GERARD LEMAÎTRE

J. GETHYN TIMOTHY
MARTIN C. E. HUBER
ERMANO JANNITTI
PIERGIORGIO NICOLOSI

1. INTRODUCTION

The demands for the high spatial, spectral, and temporal resolution that are required to address many problems in astrophysics have stimulated the development of imaging detector systems and of optical systems which can simultaneously provide spectral and spatial information. At EUV wavelengths, which are of critical importance for the study of high-temperature plasmas, the lack of window materials and high reflectivity optical surfaces require the use of open-structure detector systems and a minimum number of reflecting surfaces. In this paper we describe the results of the first tests of an imaging EUV spectrometer employing a single concave toroidal diffraction grating and a two-dimensional pulse-counting MAMA detector system utilized in an open-structure configuration. The imaging characteristics of the spectrograph are determined primarily by the performance of the toroidal grating which was fabricated by a unique technique employing an elastically-deformable substrate.

Initial tests of the grating were made in a laboratory spectrograph using photographic film. Subsequent tests were made using an imaging visible-light MAMA detector coupled to a down-converting EUV-to-visible phosphor screen. The results of these measurements were reported in Huber et al. (1988a). Both of these measurements indicated that the toroidal grating produced stigmatic imaging over the desired wavelength range, but the results from these tests were limited by deficiencies in the experimental instrumentation. The nonlinearity of the photographic film made it difficult to properly estimate the blur size of a point source image, and in the second series of measurements the blur in the image was dominated by the transfer function of the down-converting phosphor rather than aberrations from the grating. Consequently, although we were able to demonstrate that the grating had good imaging characteristics, we were not able to determine the ultimate performance of the grating. In this paper we present the first measurements taken with instrumentation designed to overcome these past deficiencies. The down-converting phosphor screen has been removed by the use of a specially designed spectrometer built at the University of Padua which was coupled to an open-structure MAMA detector system.

2. SPECTROMETER CONFIGURATION

The design of the imaging spectrometer was stimulated initially by the need for high-temporal-resolution observations of the solar chromosphere, transition region and corona with high spectral resolution ($\lambda/\Delta\lambda \approx 2 \times 10^4$) and a spatial resolution of 1″ or better (Huber and Tondello 1979). The basic configuration of the spectrometer is shown in Figure 1. In the conventional Rowland circle mounting, the vertical and horizontal foci from a spherical diffraction grating are not coincident. Exact stigmatic focusing can, however, be obtained at two points in the spectrum by selecting the vertical radius of curvature, R_v, of a toroidal grating to be smaller than the horizontal radius, R_h (Haber 1950; Cash 1984). The two stigmatic points are located symmetrically to the grating normal at the angles of diffraction $\pm\beta_0$ given by:

$$R_v = R_h \cos\alpha \cos\beta_0 \qquad (1)$$

where α is the incidence angle of light on the grating. In a system where β_0 is small and the focal ratio is of the order of f/15 or slower, stigmatic focusing can be achieved with a toroidal grating between and somewhat beyond the two stigmatic points. However, for higher speed systems (f/10 or faster), corrections for higher-order aberrations are required (e.g., Cash 1984). In order to evaluate a system of this type, we have fabricated toroidal replica gratings using a unique technique developed by Lemaître (1978) which employs an elastically deformable substrate. Descriptions of the fabrication technique and of the first laboratory test results are given in Huber et al. (1988a). Equation (1) shows that the spectral region over which stigmatic focusing is achieved is determined by R_v/R_h, the aspect ratio of the grating, and by α. The grating equation

$$m\lambda = d(\sin\alpha - \sin\beta) \qquad (2)$$

with the diffraction angle β set to zero shows that α also determines the central wavelength on the detector. For a toroidal grating spectrometer it is therefore necessary to select a wavelength interval of interest over which α and the grating aspect ratio are matched to give stigmatic imaging. The central wavelength on the detector increases with α, but the size of the stigmatic interval determined by β_0 decreases with α. We define the incidence angle α_m to be where $\beta_0 = 0$ and $\cos\alpha_m = R_v/R_h$. As α increases to and beyond α_m, stigmatic focus is achieved only on the grating normal. β_0 varies rapidly with α when $\alpha \cong \alpha_m$. The maximum
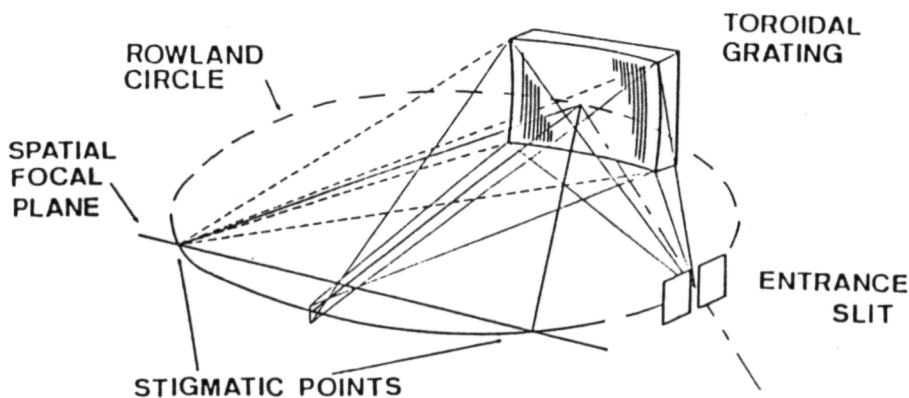

FIGURE 1—The focal properties of a toroidal grating are shown. The best focus is achieved on the Rowland circle at the two stigmatic points. Image degradation between and just beyond these points is slight.

width of the stigmatic interval is limited by the speed of the grating. Faster speeds require smaller stigmatic intervals. For most practical spectrometers the size of β_0 will be constrained to be small enough so that using α_m in equation (2) with $\beta = 0$ will give an excellent approximation to the center of the stigmatic interval.

Table 1 shows the design specifications that were initially set for the toroidal grating as well as the grating characteristics that were actually achieved. The grating specifications were chosen to allow measurements of the He I 584 Å resonance line near one of the grating's stigmatic points. For our initial tests, three gratings were fabricated by Hyperfine, Inc. of Boulder, Colorado. Measurements on the first grating fabricated showed an aspect ratio of 0.9892, which was too high and would have limited the stigmatic interval to wavelengths centered near 407 Å. The second and third replica gratings had identical aspect ratios of 0.9809, close to the desired value of 0.9782. These gratings have stigmatic intervals centered near 540 Å.

TABLE 1—DESIRED AND ACTUAL GRATING CHARACTERISTICS

Grating Parameter	Desired Value	Actual Value
Stigmatic wavelength range	520–630 Å (1st order)	520–630 Å
Angle of incidence α	11.947°	11.2°
Wavelength of grating normal ($\beta = 0°$)	575 Å	540 Å
Wavelength of stigmatic points	528, 622 Å	510, 570 Å
Horizontal radius of curvature R_h	1011.1 mm	1011.1 mm
Vertical radius of curvature R_v	989.1 mm	991.8 mm
Aspect ratio R_v/R_h	0.9782	0.9809
Ruling frequency	3600 lines mm^{-1}	3600 lines mm^{-1}
Ruled area	70×70 mm^2	70×70 mm^2

Figure 2 shows a schematic of our vacuum spectrometer. A water-cooled, hollow-cathode source illuminates the entrance aperture which consisted of a row of circular pinholes with
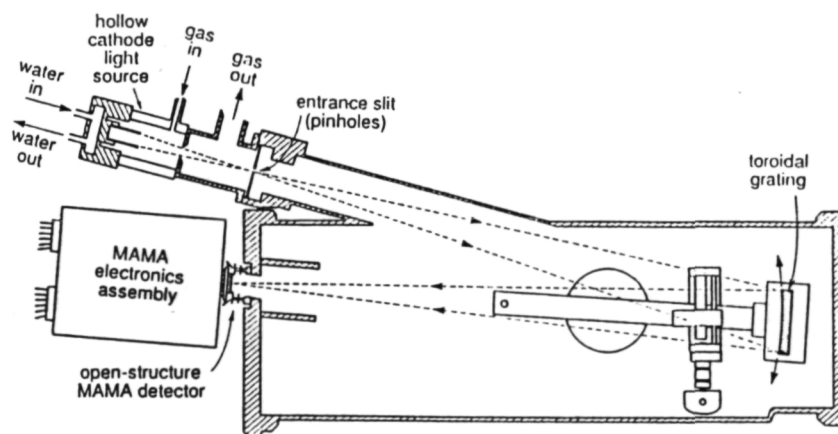

FIGURE 2—A schematic of the vacuum spectrometer used to obtain our measurements. The grating is movable along the 1 m diameter Rowland circle in order to set the incidence and emergence angles. Focus is set by moving the grating along the pivot arm.

diameters ranging between 19.2 and 22.5 μm. The pinhole centers were separated by 250 μm. The row of pinholes ran perpendicular to the plane of Figure 2 and intersected this plane on the Rowland circle. The MCP of a windowless MAMA detector was also positioned on the Rowland circle. The detector used has 25 μm square pixels in a 256 × 1024 format. The long dimension of the detector's image plane ran in the direction of spectral dispersion, i.e. parallel to the Rowland circle. Details of the construction and operation of MAMA detectors can be found in Timothy (1986). A pivot arm in the spectrometer allows the grating to be moved along the Rowland circle. The spectrometer is focused by moving the grating along the pivot arm.

One purpose of the initial tests of the spectrometer was to calibrate the incidence and diffraction angles (α and β) as a function of the grating's position settings. These were not known *a priori* owing to uncertainties in the detector mounting flange. Equation (2) shows that observing a spectral line of any known wavelength serves to define the difference ($\sin\alpha - \sin\beta$). If, in addition, a stigmatic point (β_0) can be identified by the variation of the blur diameters as a function of position on the detector, then both α and β may be derived. Measurements of β_0 can yield particularly accurate estimates of α and β because near α_m, β_0 is a rapidly varying function of α. Differences in α of only 0.1° can change the position of the stigmatic points by 50 Å. Since the detector covers only ~70 Å, this technique usually requires an initial search to locate the stigmatic points.

The spectrometer was operated with a pressure of $\leq 10^{-6}$ Torr in the main chamber. A differential pumping system on the hollow-cathode source keeps most of the lamp gas and cathode residual from entering the main chamber; however, gas flow through the pinholes is inevitable and causes pinhole blockage because of the buildup of residual cathode material which is entrained in the gas flow. The pinholes had to be reopened by cleaning several times during the course of these measurements. A vertical array of ten pinholes was used to obtain ten spectra simultaneously. As we will show shortly, buildup of material in the pinholes was partially responsible for large intensity variations between images of the various pinholes, and made the true diameter of a given pinhole quite uncertain for any given spectrum.

Gas in the main vacuum chamber represents a potential danger to a functioning MAMA detector. High ambient pressures can cause arcing within the tube. During the course of these measurements the chamber was opened several times to allow adjustments of the detector mounting and to clean the pinholes. To allow a shorter pumping cycle-time the tube was operated at an unusually low MCP voltage which resulted in low and unstable gain in the detector. Time constraints did not permit flat fields to be recorded at the time these measurements were taken. The flat field used to normalize this spectrum was recorded in a different lab several weeks later. At normal MCP voltages the detector stability is sufficient for this procedure to be acceptable, but this was not the case at the low voltages used for these data.

3. TEST RESULTS

The hollow-cathode lamp on the spectrometer can be run with different noble gases. We have recorded spectra from He, Ne, and Ar, but here we will only discuss the results obtained from a single Ne spectrum. This spectrum was chosen for this initial discussion of the performance of the spectrograph because it shows a large number of spectral lines which are distributed throughout the image and which encompass a large range of intensities. It was also chosen because it was taken during a period when most of the pinholes were unblocked. We will see below, however, that this spectrum was not well suited for a determination of the optimal imaging characteristics of the spectrograph.

PINHOLES:
1
2
3
4
5
6
7
8
9
10

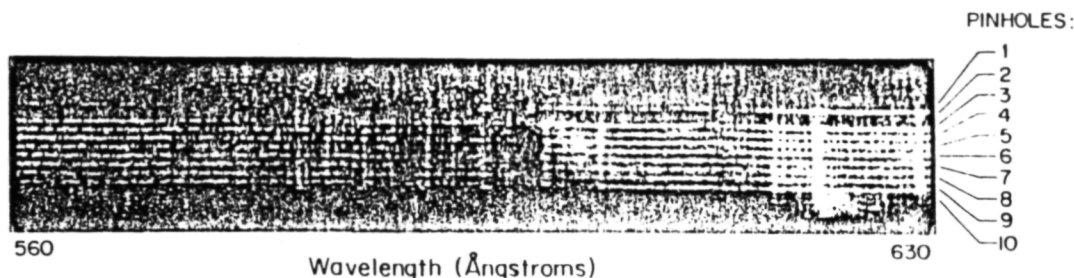560   Wavelength (Ångstroms)   630

FIGURE 3—A 1000 s exposure of the Ne I spectrum. The entrance aperture consisted of 10 equi-spaced pinholes. Each horizontal stripe is the Ne I spectrum imaged through a single pinhole. The dispersion runs in the horizontal direction; wavelength increases from left to right starting at about 560 Å and near 630 Å. The second pinhole from the top was blocked at the time of this exposure.

Figure 3 shows an image of a 1000 s exposure of the Ne I spectrum. The horizontal axis of the figure is in the direction of spectral dispersion and the vertical axis is parallel to the spatial dimension. Each horizontal stripe is the spectrum from a single pinhole. For reference we number the pinholes starting with pinhole 1 at the top of Figure 3. Pinhole 2 (the second from the top) was blocked at the time of this exposure. Wavelengths increase from left to right in the image. The lookup table used in this display was chosen to emphasize the low-intensity emissions. This look-up table does not vary linearly with input intensity and results in a decreased contrast between the bright emissions at the right of the figure and those seen elsewhere.

Flat field corrections have been applied to these data. A wavy pattern of alternating high and low columns may be seen in the low intensity background light on the right side of Figure 3. This pattern is the result of improper flat field corrections owing to the problems discussed in Section 2. Errors in the flat field corrections are much less severe on the left side of the detector owing to gain variations across the MCP. Such errors lead to large uncertainties in the relative intensities of the spectral lines measured at wavelengths longward of 615 Å. The spatial structure in the measured background light caused by the errors in the flat field corrections shows that the errors are most severe in the spectral dimension. To first order they inhibit only our attempts to estimate the spectral resolution of the spectrograph.

Figure 4 shows the spectrum obtained by averaging the signal from pinholes 7 through 10 from the array. The inset in Figure 4 shows the weak emissions on the left side of the detector with an expanded scale. Nearly all of the small scale structure seen in the inset is real. The lines labeled in the spectrum are not the only identified lines. Only 6 of the 42 Ne I lines listed to be in this wavelength interval by Kelly and Palumbo (1973) are missing from the spectrum. All of the missing lines are of weak intensity. Emissions from elements other than Ne are clearly present. The two strong lines between 615.63 Å and 618.67 Å are possibly from O II. Many of the weak lines, like that at 593.96 Å, are as yet unidentified.

The spectrograph dispersion was measured from the known wavelengths of the identified Ne I lines and was found to agree with the theoretically calculated value to within 0.25%. Based on a ruling frequency of 3600 lines mm^{-1} and a focal length of 1011.1 mm, a dispersion of 69.8 mÅ pixel^{-1} is expected. The dispersion derived from a linear fit to the wavelengths of the Ne I lines was 70.0 mÅ pixel^{-1}. For this combination of grating and detector, fits of higher
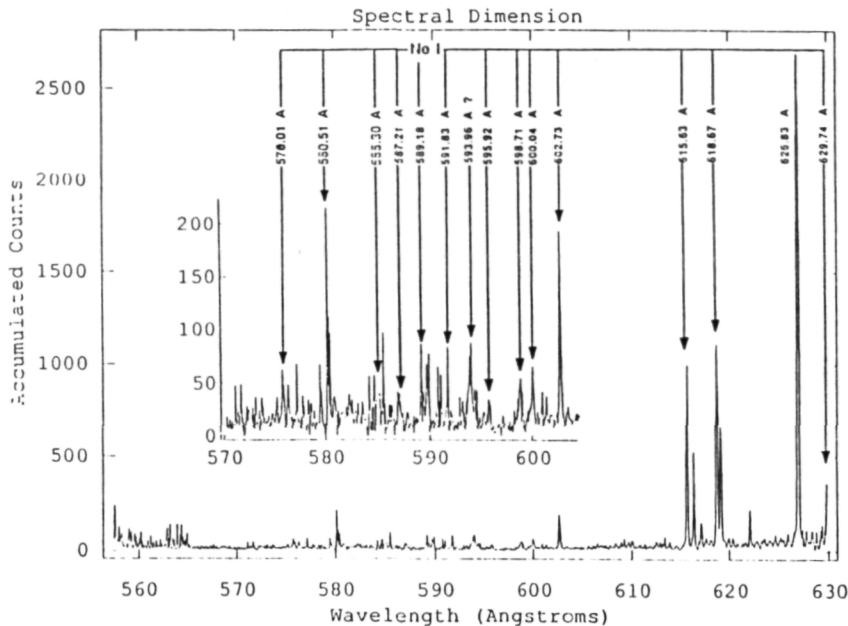
FIGURE 4—The spectrum obtained by averaging the bottom four pinholes shown in Figure 3. The inset shows the weak emissions between 570 and 603 Å with an expanded scale. The lines labeled are not all of those that have been identified. Errors in the flat field corrections applied to these data make the intensity of lines longward of 610 Å very uncertain.

than linear order are not required. The deviations from the linear fit were negligible. A large majority of the 32 lines used for the dispersion calibration had sub-pixel deviations from the linear fit.

The true spectral resolution of the spectrograph is difficult to estimate from this exposure. Owing to errors in the flat field corrections, the relative peak intensities of the strong lines longward of 615 Å could be in error by factors as large as 50%. This can be seen by the oscillations present in what should be a smoothly varying continuum between 620–630 Å. These oscillations are caused by the errors in the flat field corrections discussed earlier. Accordingly, the measured spectral widths of the lines longward of 615 Å can be in error by nearly this same factor. Attempts to fit profiles to these lines confirm this.

Lines within this wavelength interval have spectral widths that vary by a factor of ~2. The known f-values for these lines and estimates of the gas density and temperature in the hollow-cathode lamp indicate that all of these lines should be spectrally unresolved. The width variations are nearly random and do not correspond to any variations attributable to the grating performance. Lines shortward of 615 Å are not strongly affected by flat field errors, but the weak lines are so crowded together that it is difficult to avoid profiles which are blends of multiple lines. The possibility of line blends makes fits to the weak lines meaningful only if all line emissions have been properly identified.

Rough estimates of the spectral resolution can be made by inspection of closely spaced line pairs. The inset of Figure 4 shows a well-resolved triplet of lines beginning at 580.51 Å and ending at 580.79 Å. These are clearly the Ne I lines that Kelly and Palumbo list at 580.57, 580.69 and 580.71 Å. It is clear from this example that the spectral resolution is close to or better than the pixel spacing on the detector. Another example is the line in the inset
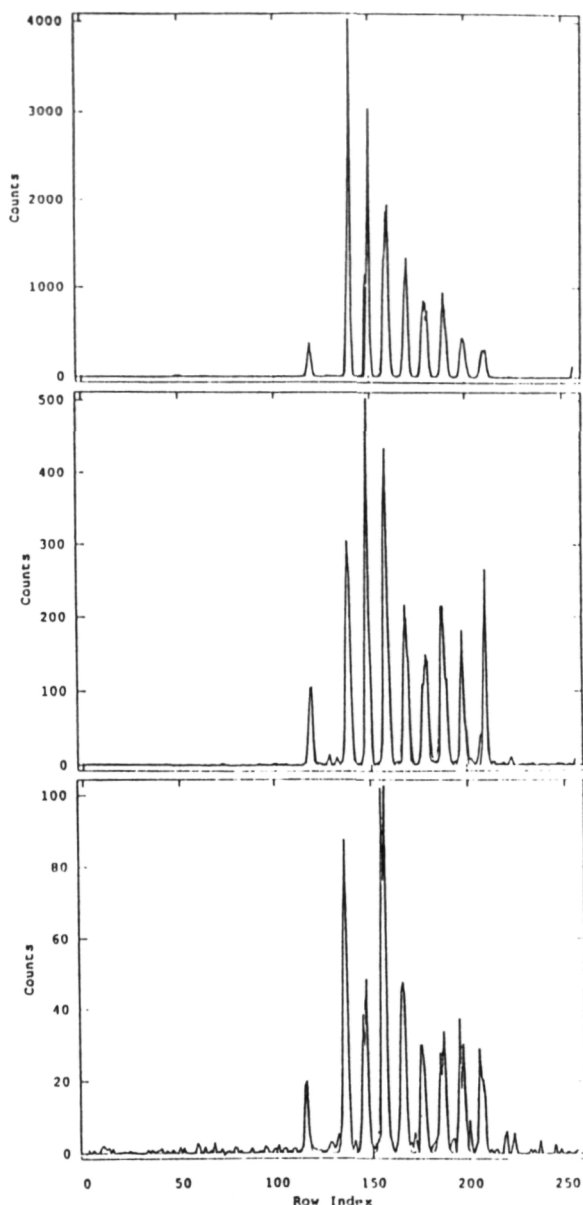
386 ☐ MORGAN ET AL.

FIGURE 5—Three spatial cuts through the spectrum in Figure 3. The cuts were made at the wavelengths of the emission lines at 626.83, 615.63, and 602.73 Å. Pinhole 1 (which appears as the topmost horizontal strip in Fig. 3) appears as the leftmost peak in these plots. The dark line in each plot shows the data and the thin line shows the result of the least-squares Gaussian fits to the data.

marked 585.30 Å. This line, which looks broader than others nearby, is actually a blend of two Ne I lines, one at 585.30 Å and the other at 585.25 Å. As can be seen from Figure 4, these two lines are almost resolved in the spectrum. These estimates agree with attempts to fit the spectral profiles of several lines near 600 Å. These attempts yielded an average line width of ~1 pixel.

The spatial resolution in the spectrograph image is illustrated by the spatial cuts shown in Figure 5. The figure shows vertical cuts through the image of Figure 3 at three different wavelengths. The heavy lines in Figure 5 show the data obtained by averaging over 350 mÅ of the spectrum centered at each labeled wavelength. Pinhole 1 is the first peak on the left. Blockage from the hollow-cathode residual material is partially responsible for the variation of intensity seen through the pinholes. This certainly causes the lack of any emission from pinhole 2. It probably causes the reduced intensity seen in pinholes 1 and 6 through 10. However it is clear from a comparison of the relative pinhole intensities at each wavelength that pinhole blockage does not cause all of the intensity variations. The greatest intensity is not seen through the same pinhole at all wavelengths. These variations must be caused either by spatial variations in the lamp emissions or by problems with the flat field corrections. The former explanation appears likely in light of the fact that the relative pinhole intensities appear to vary throughout the spectrum, both in and out of the region affected by errors in the flat field corrections. In addition, these spatial cuts should be relatively unaffected by the flat field errors owing to the spatial structure which is clearly associated with these errors.
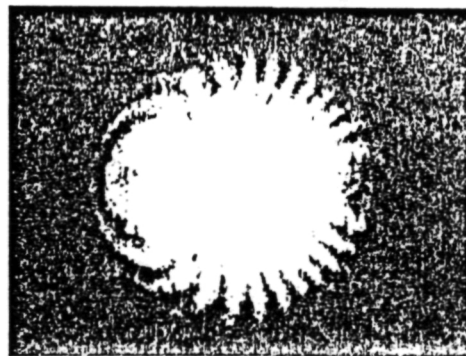
The light lines in Figure 5 show Gaussian fits to the image of each pinhole. In units of the 25 μm pixels, the average e^{-1} half-width for each spatial cut was found
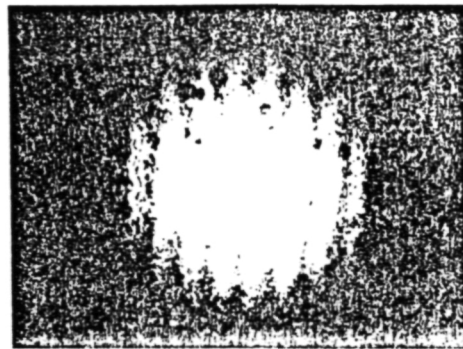
RELAXED - SPHERICAL
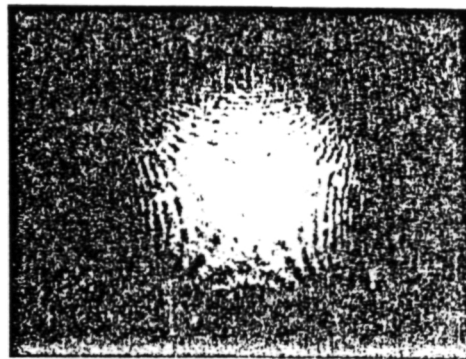
DEFORMED - TOROIDAL

DEFORMED - COMA INDUCED

FIGURE 7—Interferograms indicating the surface figure of the substrate illustrated in Figure 5 are shown. A modified Martin-Watt-Weinstein interferometer was used to record the interferograms. This configuration uses a spherical mirror in the reference beam. In its relaxed state the substrate produces the top interferogram which is indicative of its spherical surface. For the middle interferogram the substrate was distorted into a toroid, for which the saddle pattern is characteristic. The bottom interferogram shows that coma may be induced by the proper application of the mechanism's pressure points.

the detector and entrance aperture to lie along the grating's Rowland circle.

The benefits of being able to move either the detector or the entrance aperture off the Rowland circle are freedom to decrease the size of the spectrograph and an added ability to add magnification or to change the speed of the grating. This can be accomplished by adding second order corrections to the grating surface which add the appropriate amount of the negative coma. Figure 6 shows a mechanism which has been designed to help fabricate gratings with the required surface figure. This mechanism is used to deform the spherical master grating shown mounted on it in the figure. It differs from that used to produce the toroidal grating used in these measurements in that it has four independent pressure points through which the grating surface may be defined. Figure 7 shows interferograms which illustrate that the mechanism can successfully produce the required deformations. The interferograms in Figure 7 show the fringes relative to a spherical reference mirror. The top interferogram was obtained with the undistorted spherical master grating. The middle interferogram shows the characteristic saddle pattern obtained with the master deformed to a toroidal figure and the bottom interferogram shows that the master can be deformed to induce coma.

To properly utilize the advantages gained by these new gratings requires low-noise imaging detectors of smaller pixel size and larger pixel formats. As the complexity of the grating surfaces grows so does the area over which useful images may be made. As the spectrograph size decreases so do the blur diameters. The development of MAMA detectors is keeping pace with these demands.

Jeffrey S. Morgan, David C. Slater, and J. Gethyn Timothy are at the Center for Space Science and Astrophysics, Stanford University, ERL 314, Stanford, CA 94305.

Martin C. E. Huber is at the Space Science Department, ESA, ESTEC Postbus 299, NL-2200 Noordwijk, The Netherlands. He is on leave from the Institute for Astronomy, ETH-Zentrum, Zürich, Switzerland.

Ermano Jannitti, Giampiero Naletto, Piergiorgio Nicolosi, and Giuseppe Tondello are at the University of Padua, Department of Electronics and Informatics, 6/A via Gradenigo, I-35100 Padua, Italy.

Gerard Lemaître is at the Marseilles Observatory, 2 place Le Verrier, F-13004 Marseilles, France.

The fabrication of toroidal and coma-corrected toroidal diffraction gratings from spherical master gratings using elastically-deformable substrates: a progress report

Martin C. E. Huber

Space Science Department, ESTEC
Postbus 299, 2200 AG Noordwijk, The Netherlands

J. Gethyn Timothy and Jeffrey S. Morgan

Center for Space Science and Astrophysics, Stanford University, ERL 314
Stanford, California 94305-4055 USA

Gerard Lemaître

Observatoire de Marseille
2 place Le Verrier, F-13248 Marseille Cedex 4, France

and

Giuseppe Tondello and Giampiero Naletto

Istituto di Elettronica, Università di Padova
Via Gradenigo 6/a, I-35100 Padova, Italy

ABSTRACT

We have developed a technique which permits toroidal, and coma-corrected toroidal, diffraction gratings to be replicated from spherical master gratings by the use of elastically-deformable substrates. Toroidal gratings correct for astigmatism and, thus, make it possible to construct stigmatic spectrometers that employ a single reflective diffraction grating. These spectrometers are particularly useful for the extreme-ultraviolet (EUV) wavelength range, where reflection coefficients are low, since the single optical surface provides for dispersion, focussing, and astigmatism correction. The fabrication procedures for the pure toroidal, and coma-corrected toroidal, gratings are described, and initial test results are presented. The use of the toroidal gratings in a high-resolution sounding-rocket EUV spectroheliometer (HiRES), and in both the Coronal Diagnostics Spectrometer (CDS) and the Ultraviolet Coronagraph Spectrometer (UVCS) on the ESA/NASA Solar and Heliospheric Observatory (SOHO) mission, is described briefly, and the use of this technique for the fabrication of a coma-corrected toroidal grating for the prime Rowland spectrograph of the FUSE/Lyman mission is briefly discussed.

1. INTRODUCTION

The extreme ultraviolet (EUV) spectral region at wavelengths below ~120 nm is of critical importance for the diagnostics of conditions in high-temperature plasmas, since this region contains emission lines and continua characteristic of temperatures in the range from ~10^4 to >10^6 K. This spectral region is, thus, particularly useful for studies of dynamic phenomena in the outer atmospheres of the sun and other stars. In addition, observations at these wavelengths can provide unique astrophysical data on dynamic phenomena in planetary atmospheres and magnetospheres, on the exchange of matter and energy between stars and the interstellar medium, on the variations of light element abundances in the galaxy, and on the dynamics of the hot gas in galactic halos.

Because of the lack of window materials and of high-reflectivity optical surfaces at these wavelengths, practical systems for imaging and spectroscopy must employ open-structure detector systems and a minimum of reflecting surfaces. The recent development of high-resolution imaging detector systems which can operate with high efficiency at EUV wavelengths has stimulated the design of imaging spectrometers for use at these wavelengths.

We have developed a technique which permits toroidal, and coma-corrected toroidal, diffraction gratings to be replicated from spherical master gratings by the use of elastically-deformable substrates. Toroidal gratings correct for astigmatism and, thus, make it possible to construct stigmatic spectrometers that employ a single reflective diffraction grating. These spectrometers are particularly useful for EUV wavelength range, since the single optical surface provides for dispersion, focussing, and astigmatism correction. To date, we have fabricated and tested three pure toroidal replica gratings with aspect ratios of the order of 0.978, average radii of curvature of 1000 mm, and ruling frequencies of 3600 grooves mm^{-1}, which are designed to operate with a focal ratio of f/15 at an angle of incidence of 11.95°. These gratings produce stigmatic images over a wavelength range of about 10 nm centered around 60 nm at angles of diffraction close to the grating normal. A fast toroidal replica grating with a focal ratio of f/8, which can be used at a large angle of incidence in the range from 25° to 30°, has also been fabricated and is under initial test. A coma-corrected version of this toroidal grating will be fabricated shortly. The fabrication procedures for the pure toroidal, and coma-corrected toroidal, gratings are described, and test results are presented. The use of the toroidal gratings in a high-resolution sounding-rocket EUV spectroheliometer (HiRES), and in both the Coronal Diagnostics Spectrometer (CDS) and the Ultraviolet Coronagraph Spectrometer (UVCS) on the ESA/NASA Solar Heliospheric Observatory (SOHO) mission, is briefly described, and the use of this technique for the fabrication of a coma-corrected toroidal grating for the prime Rowland spectrograph of the FUSE/Lyman mission is briefly discussed.

2. THE TOROIDAL GRATING SPECTROMETER

The design of the spectrometer was stimulated initially by the need for high-time-resolution observations of the solar chromosphere, transition region, and corona with a high spectral resolution ($\lambda/\Delta\lambda \sim 2 \times 10^4$) and a spatial resolution of 1 arc sec or better.[1] The basic configuration of the spectrometer mounting is shown in Fig. 1(a).

In the conventional Rowland circle mounting, the vertical and horizontal foci from a spherical diffraction grating are not coincident. However, Haber[2] has pointed out that it is possible to obtain stigmatic focusing at two points in the spectrum by selecting the vertical radius of curvature R_v of a toroidal grating to be smaller than its horizontal radius R_h. As shown in Fig. 1 (a), exact stigmatic focusing can then be obtained at two positions in the spectrum given by
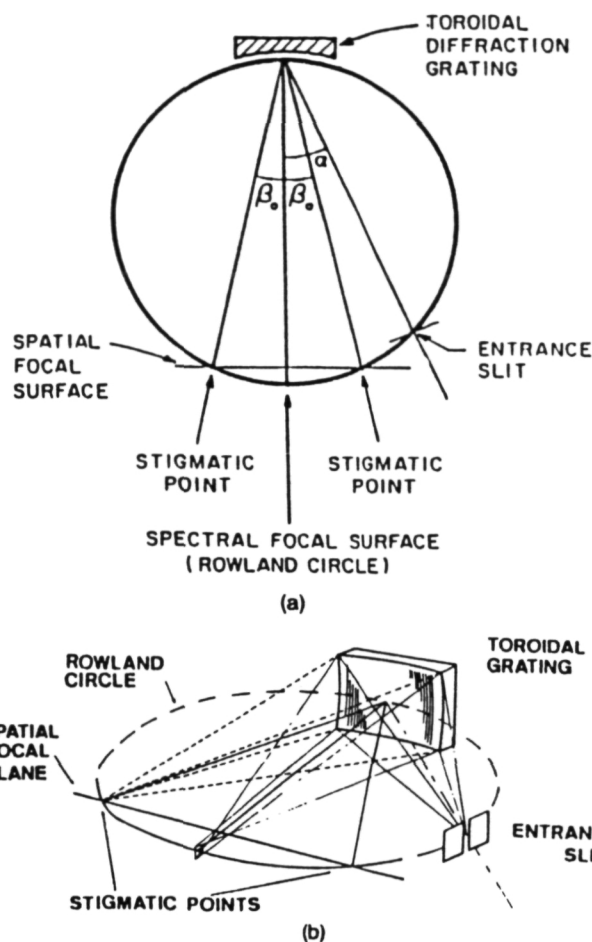

Fig. 1 (a) Schematic of the imaging EUV spectrometer employing a single toroidal grating. Exact stigmatic focusing is obtained at angles of diffraction $\pm \beta_0$, which are defined by Equation (1). Given a sufficiently small value of β_0 and some depth of focus, effective stigmatic focusing can be achieved between and somewhat beyond the two stigmatic points. (b) Isometric display of the imaging properties at the two stigmatic points $\pm \beta_0$.

$$R_v = R_h \cos\alpha \cos\beta_0 \qquad (1)$$

The two stigmatic points are located symmetrically to the grating normal at the angles of diffraction $\pm\beta_0$, as shown in Fig. 1 (a). An isometric display of the imaging properties of the two stigmatic points is shown in Fig. 1 (b).

In a practical system where β_0 is small and there is some depth of focus (moderate speed systems with focal ratios <f/15), stigmatic focusing can be achieved between and somewhat beyond the two stigmatic points with a simple toroidal surface. Ray tracing studies[1] have shown for a 3600-groove mm^{-1} grating with a radius of curvature of

2000 mm, blur sizes of significantly <40 μm can be obtained over an effective wavelength range of >10 nm. However, for higher speed systems (f/10 or faster), which will be required for astrophysical studies, corrections for higher-order aberrations are required.[3]

3. GRATING FABRICATIONS

To evaluate the performance characteristics of a toroidal grating at EUV wavelengths, we have fabricated a number of toroidal replica gratings using a unique technique developed by Lemaître. This technique uses an elastically deformable grating which is replicated from a spherical master ruling. The ratio to the vertical and horizontal radii of curvature can then be set to any desired value by applying a distorting force to the flexible substrate. The stainless steel flexible substrate has a form which elastically deforms into an exact toroidal surface with the application of a single adjustable distorting force. The grating, with a ruling frequency of 3600 grooves mm^{-1}, and an active area of 70 x 70 mm^2, was replicated onto the deformable concave substrate by Hyperfine, Inc., Boulder, CO from a concave spherical master ruling using an intermediate convex replicating surface. A radius of curvature of 1000 mm was selected for the initial grating for convenience in laboratory testing. After the substrate had been deformed to the appropriate aspect ratio, a fixed concave toroidal grating was replicated from the deformable substrate, again using an intermediate convex replicating surface. The replication sequence is shown in Fig. 2.

The characteristics of the f/15 toroidal grating are given in Table 1.

A total of three toroidal replica gratings with these characteristics have been fabricated to date by Hyperfine, Inc.; one is at the University of Padua and two are at
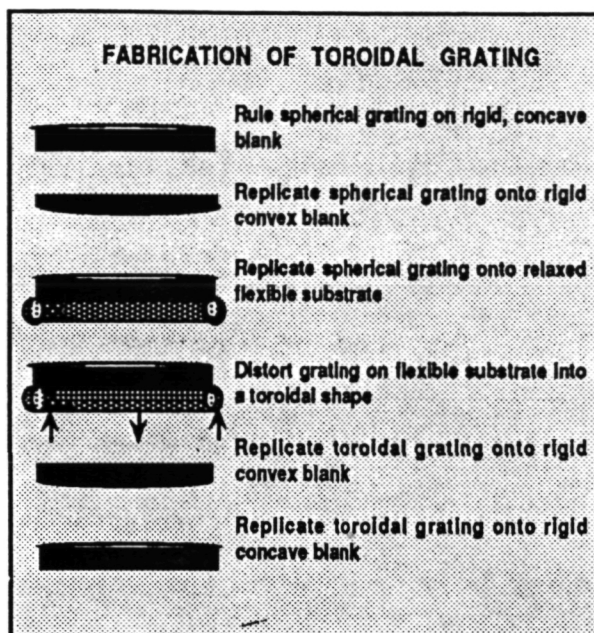

Fig. 2. Fabrication sequence for toroidal replica grating using an elastically-deformable substrate.

Stanford University. In addition, a further toroidal replica grating has been fabricated from a spherical master grating with a ruling frequency of 1800 grooves mm^{-1}. This grating will be used to produce stigmatic images at wavelengths between 104 and 126 nm in the first order and between 52 and 63 nm in second order for characterization of the MAMA detector systems for the SOHO mission.[4] All the other characteristics of this grating are identical to those listed in Table 1.

In order to fabricate a coma-corrected toroidal grating using this technique, a more complex deformable substrate is required to impose the small departures from the pure toroidal form required for the correction of coma. The

---

TABLE 1.	
Desired Characteristics of the f/15 Test Toroidal Diffraction Grating	
Wavelengths and angles of rays	
Stigmatic wavelength range	52-63 nm (first order)
Angle of incidence α	11.947°
Wavelength on grating normal (β=0°)	57.5 nm
Wavelength at stigmatic points (β$_0$ = ± 0.825°)	53.5 nm, 61.5 nm
Grating surface	
Horizontal radius of curvature R$_h$	1011.1 mm
Vertical radius of curvature R$_v$	989.1 mm
Aspect ratio R$_v$/R$_h$-	0.9782
Ruling frequency	3600 grooves mm^{-1}
Ruled area	70 x 70 mm^2

oma-correcting deformable substrate is, again, spherical in its relaxed form, but requires six actuators for the deformation, rather than the single actuator required for the toroid-forming substrate.

The fabrication sequence for the coma-corrected toroidal grating is essentially identical to that shown in Fig. 2, but is a two-stage process. First, the spherical master ruling is replicated onto the coma-correcting substrate. This is then deformed into the figure required for the coma correction. The coma-correcting figure is then replicated onto the relaxed toroid-forming substrate. The substrate is then deformed into the exact toroidal shape and the fixed coma-corrected toroidal grating replicated.

In order to evaluate this procedure for fabricating coma-corrected toroidal gratings, we are in the process of fabricating two replica gratings, the first a pure toroid and the second a coma-corrected toroid. We have selected a fast focal ratio of f/8 and an angle-of-incidence of 30° in order to introduce a large amount of coma in the spectral images from the pure toroidal grating. The desired characteristics of the f/8 toroidal test grating are listed in Table 2.

The wavelength on the grating normal of 208 nm is very close to that of a strong Zn emission line produced by a commercially-available light source.

At this time, the first toroidal replica grating is under initial evaluation and fabrication of the elastically-deformable substrate for the coma correction is about to start.

4. TEST RESULTS

A series of measurements of the performance of the first f/15 toroidal replica grating at EUV wavelengths were carried out at the University of Padua in 1985 and 1988, and have been reported in the literature.[5,6]

Further measurements on this grating were completed at the University of Padua in 1990 in an attempt to arrive more closely at the exact stigmatic focus. The laboratory spectrometer was set up in the same manner as for the earlier tests with a row of ten pinholes along the entrance slit, each 20 µm in diameter with separations of 250 µm. The data were recorded using a tetraphenyl butadine down-correcting phosphor deposited on a fiber-optic faceplate that was the window to the vacuum spectrograph. The visible-light photons were detected by an intensified CCD detector system. The light source was a dc hollow cathode operating with noble gases; most of the data were recorded at 58.4 nm, the wavelength of the strong He I resonance line. It was found that the stigmatic condition could be satisfied for $\alpha = 11.62°$ and $\beta = 0.51°$ at 58.4 nm, yielding an aspect ratio R_v/R_h of 0.9795, very close to the desired value of 0.9782. Images of the pinholes at 58.4 nm, recorded with low (5 mbar) and high (30 mbar) pressures in the hollow cathode lamp are shown in Fig. 3. The point spread function of the detector and the effect of the finite size of the pinholes were determined by placing the pinholes directly on the phosphor and illuminating them with 253.7 nm radiation from a Hg lamp. The measured instrument function was then deconvolved from the recorded data, yielding the spectral images shown in Fig. 4. The image of a single pinhole which clearly demonstrates the outstanding combination of spatial and spectral resolution provided by the toroidal grating is shown in Fig. 5. The residual aberrations are close to those predicted by the earlier ray trace studies.[1]

We have just started the initial tests of the first f/8 toroidal grating. These tests are being carried out at the University of Padua, using a laboratory spectrograph modified to accommodate the larger angle-of-incidence of the grating. The same detector system that was used for the

TABLE 2.
Desired Characteristics of the f/8 Test Toroidal Grating

Wavelengths and angles of rays
Stigmatic wavelength range	200 - 220 nm (first order)
Angle of incidence α	30.0°
Wavelength on grating normal	208 nm
Test wavelength	213.9 nm ($\beta = 0.75°$)

Grating surface
Horizontal radius of curvature R_h	1071.8 mm
Vertical radius of curvature R_v	928.2 mm
Aspect ratio R_v/R_h	0.866
Ruling frequency	2400 grooves mm^{-1}
Ruled area	120 x 140 mm^2
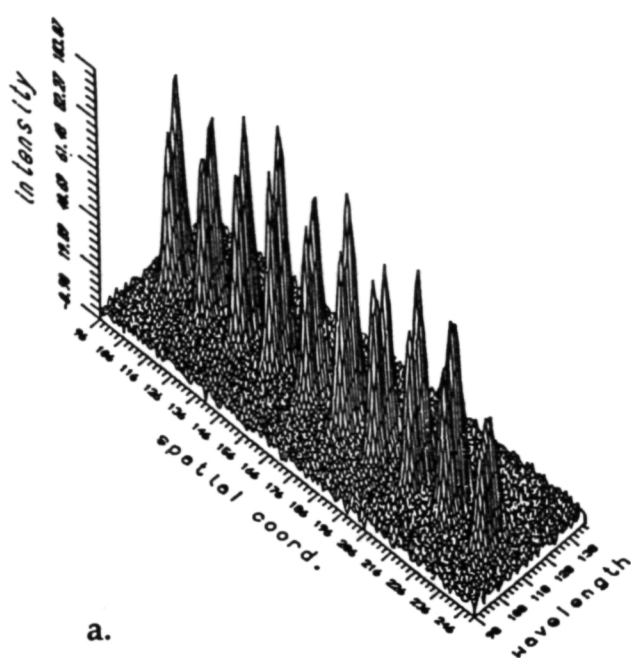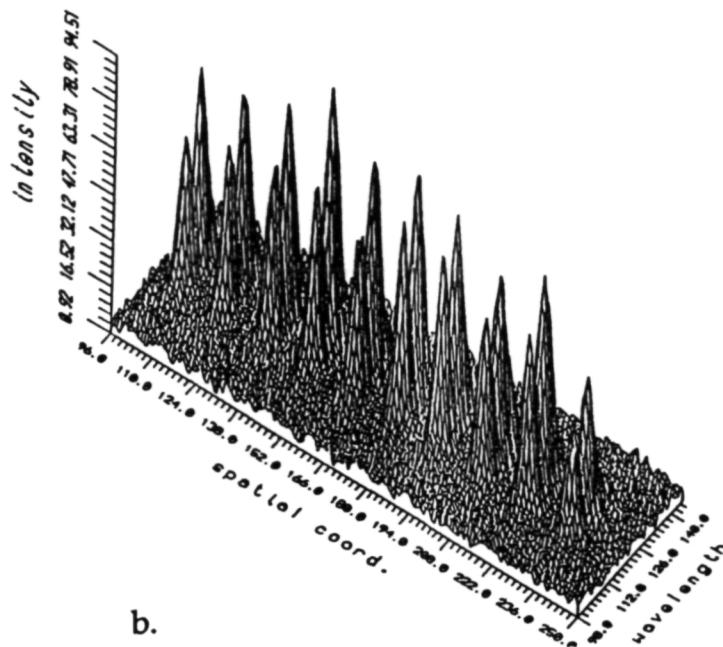
Fig. 3. Images of ten pinholes at the wavelength of the He I 58.4 nm resonance line.

a. Low gas pressure (5 mbar).   b. High gas pressure (30 mbar).
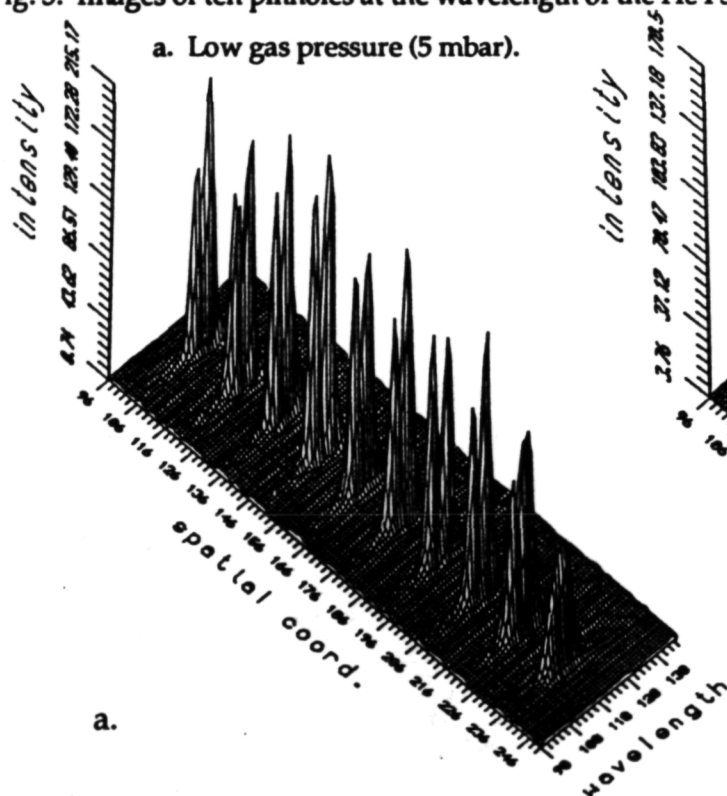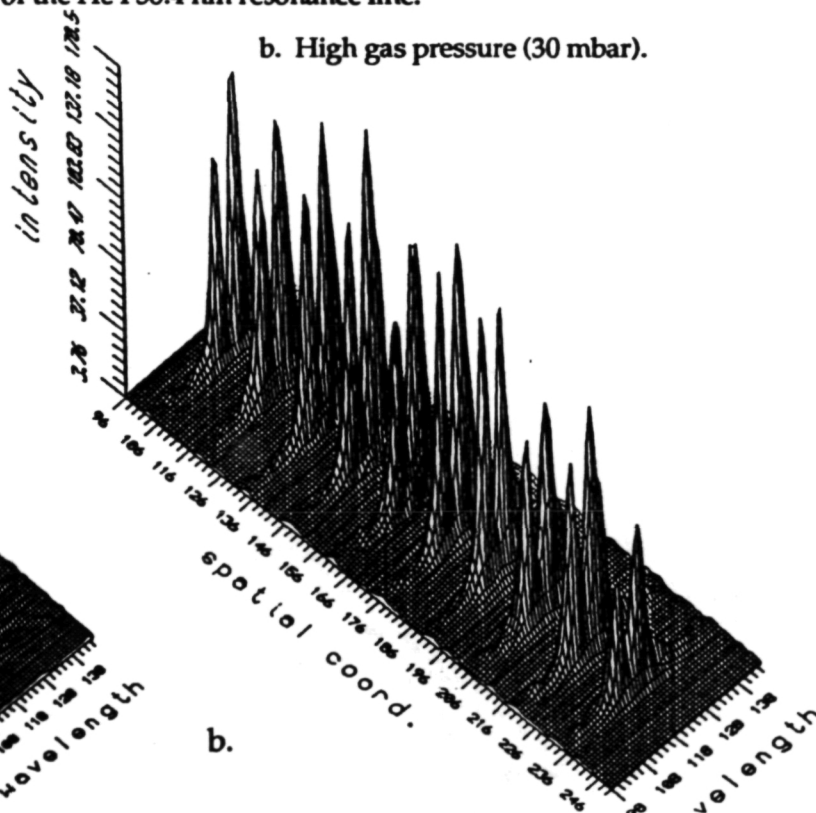
Fig. 4. Deconvolved images of ten pinholes at the wavelength of the He I 58.4 nm resonance line. Point spread function of the detector and the effects of the finite pinhole size have been removed.

a. Low gas pressure (5 mbar).   b. High gas pressure (30 mbar).

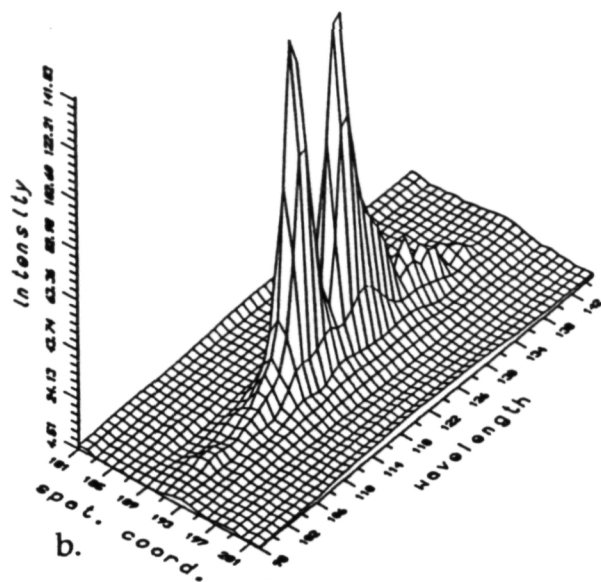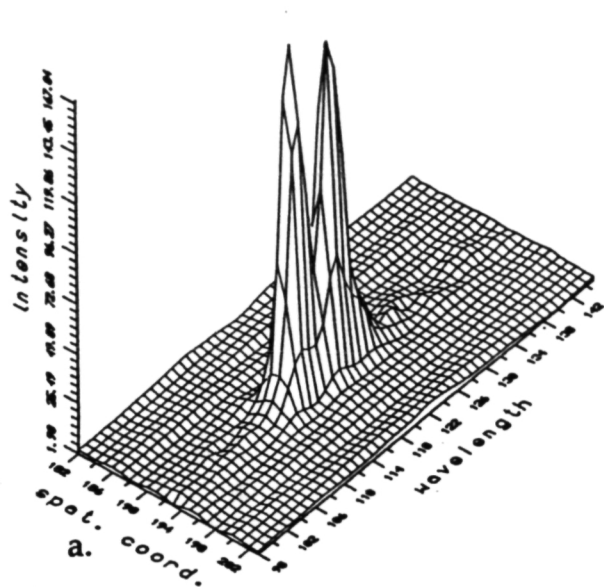Fig. 5. Deconvolved image of a single pinhole at the wavelength of the He I 58.4 nm resonance line.

a. Low gas pressure (5 mbar).   b. High gas pressure (30 mbar).
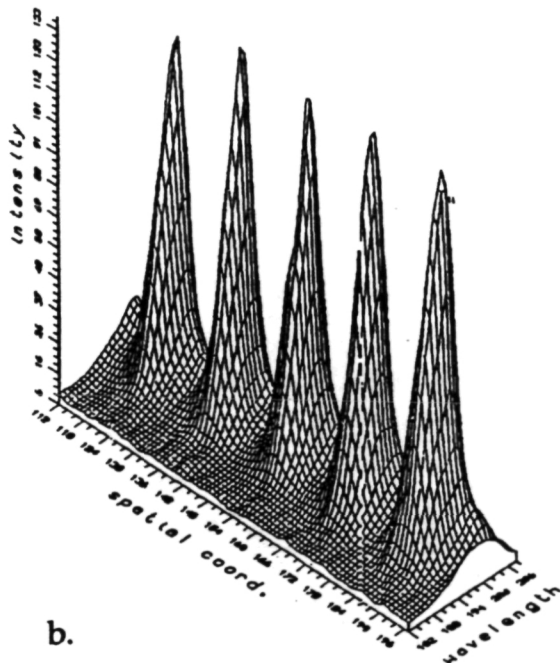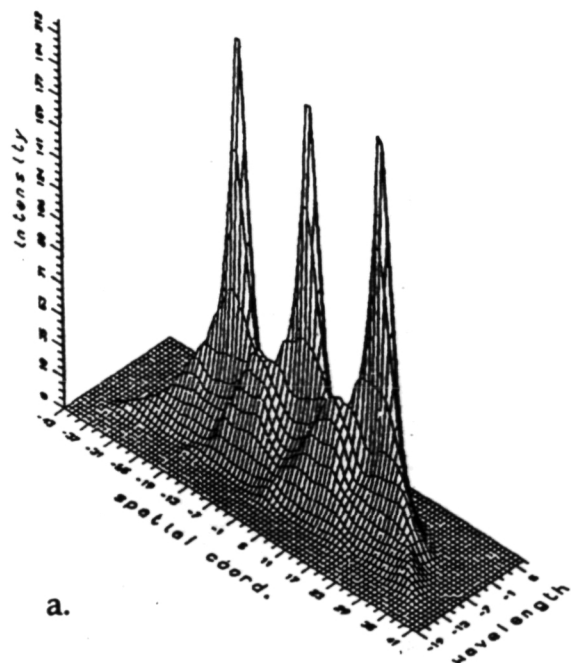

Fig. 6. Images of pinholes at the wavelength of the Zn I 213.9 nm emission line with the full 120 x 120 mm² area of the grating illuminated.

a. Analytical profiles.   b. Measured profiles.

f/15 toroidal grating tests is being employed, but in this case, the data are being recorded at the wavelength of the Zn I 213.9 nm emission line and it is not necessary to evacuate the spectrograph. The expected analytical image profiles, obtained by convolving the ray trace data with the instrumental function, for three pinholes, and the experimental data for five pinholes, with the full 120×120 mm^2 ruled area of the grating illuminated, are shown in Fig. 6. The broadening of the images, caused by coma, can be clearly seen in the analytical profiles. However, the image quality in the wings of the measured profiles appears better than that predicted by analysis, while the central core of the image is not as sharp as predicted.

In order to try to understand the measured results, the grating was masked down to its central 60×60 mm^2 area so as to limit the effects of coma. The analytical and measured data for this condition are shown in Fig. 7. It is immediately evident that the emission line is spectrally broadened with some self-reversal caused by absorption in the light source. When this effect is taken into account, there is relatively good agreement between the analytical and measured image profiles.

In a further attempt to understand why the measured profiles are superior to the analytical profiles when the full grating area is illuminated, the central 80×80 mm^2 area of the grating was masked off. The measured and analytical profiles for this condition are shown in Fig. 8. These measurements confirm the results obtained when the full area of the grating was illuminated; namely, that the effects of coma appear to be significantly less than predicted by the ray-trace analysis. The reason for this effect is at present not undersoood, and further studies of the grating performance are in progress.

We plan to continue further detailed studies of the f/15 toroidal gratings now that a second laboratory spectrograph, fabricated at the University of Padua, has been delivered to Stanford University for integration with the imaging pulse-counting MAMA detector system. The evaluation of the f/8 toroidal grating will continue at the University of Padua and will be followed by a detailed study of the first coma-corrected f/8 toroidal grating.

5. FLIGHT APPLICATIONS

A number of space ultraviolet astrophysics istruments are planning to utilize toroidal diffraction gratings fabricated by this technique. Our sounding rocket High-Resolution EUV Spectroheliometer (HiRES)[7] will employ a 1-m radius-of-curvature 3600 grooves mm^{-1} toroidal grating in an imaging EUV spectrometer in order to produce spatially-resolved

spectra of structures in the solar outer atmosphere with an angular resolution of 0.4 arc sec, a spectral resolution $\lambda/\Delta\lambda$ of about 10^4 in first order, and a temporal resolution of the order of seconds. The wavelength range from about 51 to 63 nm which contains emission lines with excitation temperatures ranging from 3×10^4 K to 2×10^6 K will be covered simultaneously.

On the ESA/NASA Solar and Heliospheric Observatory (SOHO) mission,[8] two instruments will employ toroidal diffraction gratings. These are the Coronal Diagnostics Spectrometer (CDS)[9] and the Ultraviolet Coronagraph Spectrometer (UVCS).[10] In the CDS, two toroidal gratings will be used in a normal-incidence imaging spectrometer to measure emission-line intensities in the wavelength ranges from 31 to 38 nm and from 52 to 63 nm. The UVCS will utilize the toroidal gratings in two imaging spectrometers to measure emission-line profiles and intensities at wavelengths between 102 and 130 nm in the solar corona at distances ranging from 1.2 to 10 solar radii. Emission line intensities at wavelengths between 50 and 130 nm on the solar disk will also be measured.

The FUSE/*Lyman* payload is designed to study faint sources throughout our galaxy and at very large extragalactic distances with a very high ($\lambda/\Delta\lambda \sim 3 \times 10^4$) spectral resolution at wavelengths shorter than the *Hubble* Space Telescope limit of 120 nm.[11] As currently baselined, the prime spectrograph for the wavelength range from 91 to 125 nm employs a coma-corrected toroidal grating with a focal ratio of f/10 in a Rowland-circle mounting with a diameter of 172 cm. A part of the NASA Phase A study, an asphere for the test grating was fabricated by Hyperfine, Inc. using three-axis grinding and cylindrical polishing machines. This work is continuing as part of the NASA Phase B study.

The successful fabrication of a coma-corrected toroidal grating by means of the procedures described in this paper would demonstrate the viability of this technique as an alternative fabrication procedure for the FUSE/*Lyman* gratings. This technique would permit small variations to be made to the shape of the final asphere without the necessity of repeating the grinding and polishing procedures.
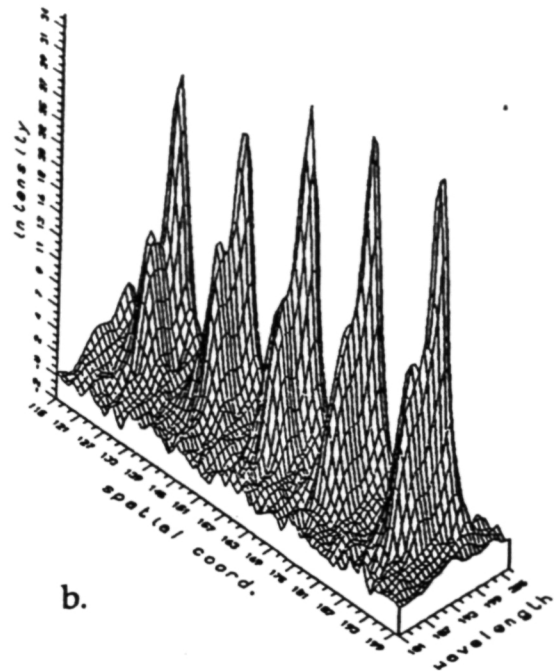
6. ACKNOWLEDGMENTS
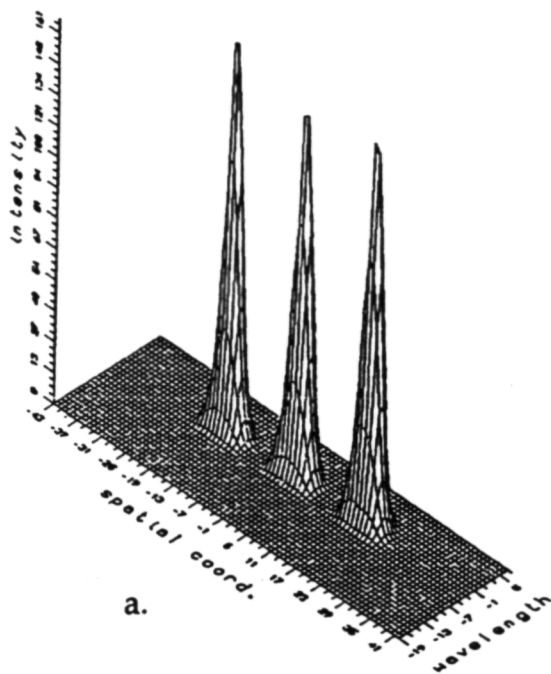
Fig. 7. Images of pinholes at the wavelength of the Zn I 213.9 nm emission line with the central 60 x 60 mm² area of the grating illuminated.

a. Analytical data.
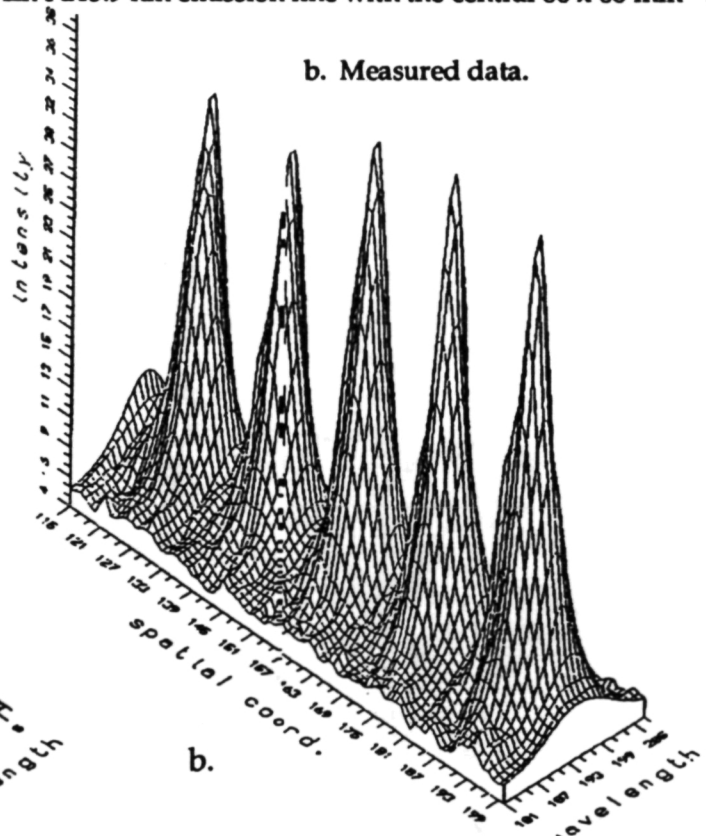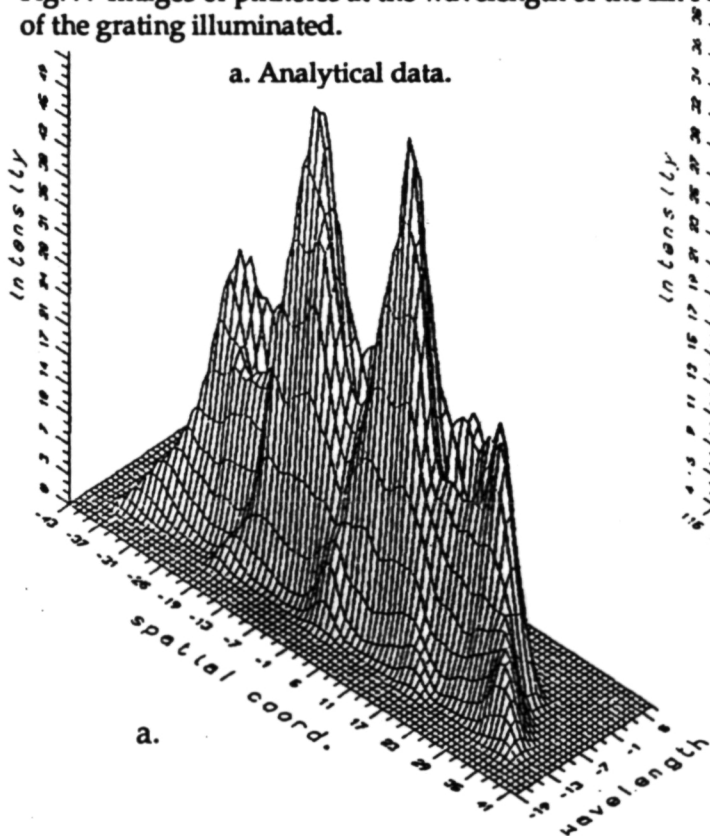
b. Measured data.

Fig 8. Images of pinholes at the wavelength of the Zn I 213.9 nm emission line recorded with the central 80 x 80 mm² area of the grating masked off.

a. Analytical data.

b. Measured data.

7. REFERENCES

1. M.C.E. Huber and G. Tondello, "Stigmatic Performance of an EUV Spectrograph with a Single Toroidal Grating", *Applied Optics* vol. 18, pp. 3948-3953, December 1979.

2. H. Haber, "The Torus Grating", *J. Opt. Soc. Am.* vol. 40, pp. 153-165, March 1950.

3. W. Cash, "Aspheric Concave Grating Spectrographs", *Applied Optics*, vol. 23, pp. 4518-4522, December 1984.

4. J. G. Timothy, "Imaging Pulse-Counting Detector Systems for Space Ultraviolet Astrophysics Missions", in these *Proceedings*.

5. M.C.E. Huber, J.G. Timothy, J.S. Morgan, G. Lemaître, G. Tondello, E. Jannitti and P. Scarin, "Imaging Extreme Ultraviolet Spectrometer Employing a Single Toroidal Diffraction Grating: the Initial Evaluation, "*Applied Optics*, vol. 27, pp. 3505-3510, August 1988.

6. J. S. Morgan, J. G. Timothy, D.C. Slater, M.C.E. Huber, G. Tondello, G. Lemaître, G. Naletto, E. Jannitti and P. Nicolosi, "A High-Efficiency Extreme Ultraviolet Spectrometer", *Extreme Ultraviolet Spectroscopy*, eds. R. F. Malina and S. Bowyer, Pergamon Press, 1991, pp. 380-389.

7. J. G. Timothy and the HiRES Science Team, "HiRES - A High Resolution Stigmatic EUV Spectroheliometer", *SPIE X-Ray/EUV Optics for Astronomy*, vol. 1343, pp. 350-358, 1990.

8. V. Domingo and A. I. Poland, "SOHO - An Observatory to Study the Solar Interior and the Solar Atmosphere", European Space Agency *SP-1104*, pp. 7-12, November 1988.

9. B. E. Patchett and the CDS Investigation Team, "CDS - The Coronal Diagnostic Spectrometer", European Space Agency *SP-1104*, pp. 7-12, November 1988.

10. J. Kohl and the UVCS Investigation Team, "UVCS - An Ultraviolet Coronagraph Spectrometer for SOHO", European Space Agency *SP-1104*, pp. 49-54, November 1988.

11. "*Lyman* - The Far Ultraviolet Spectroscopic Explorer", NASA Phase A Study Final Report *NAS5-30339*, July 1989.

Evaluation of toroidal gratings in the EUV

M.C.E. Huber*

Space Science Department of the European Space Agency (ESA) ESTEC, The Netherlands

G. Lemaître

Observatoire de Marseille, France

G. Naletto, P. Nicolosi and G. Tondello

Dipartimento di Elettronica ed Informatica, Università di Padova, Italy

E. Jannitti

Istituto Gas Ionizzati, C.N.R., Padova, Italy

J.S. Morgan and J.G. Timothy

Centre for Space Science and Astrophysics, Stanford University, USA

ABSTRACT

Toroidal gratings can be used for imaging spectrometers. These can provide stigmatic images and are very useful for space applications. Two cases are described: an Ultraviolet Coronagraph for the solar SOHO mission and a high resolution spectrometer for the stellar Lyman mission. The toroidal gratings have been produced by replicating an elastically deformed spherical one. By properly applying the distorting forces also coma-corrected surfaces can be achieved.

1. INTRODUCTION

The extreme ultraviolet region (EUV) at wavelengths below 1200 Å is of critical importance for the diagnostics of high temperature plasmas; in fact at temperatures from 10^4 K up to 10^6 K and larger their characteristic emission spectra lie in this spectral range. The EUV observations are thus particularly useful for studying phenomena in the outer atmosphere of the sun and the stars, and, in addition, they can provide unique astrophysical data on dynamic phenomena in planetary atmospheres and magnetospheres, on the flow exchange of matter and energy between the stars and the interstellar medium, on the distribution of the light elements abundances in the galaxy and on the dynamics of the hot interstellar gas in the galactic haloes.

Because of the lack of transparent window materials and of high efficiency reflecting coatings at these wavelengths, open structure detector systems and the minimum number of reflecting surfaces must be used. The recent development of high-resolution and high efficiency EUV detectors has stimulated the design of optical systems which can provide a stigmatic spectroscopic capability. These imaging spectrometers use toroidal gratings achieving simultaneously the spectral, spatial and temporal resolution required for many scientific observations.

In this paper we describe the fabrication and the results of the testing of toroidal diffraction gratings, for use in imaging EUV spectrometers at wavelengths between 300 and 1200 Å. The correction technique of various aberrations is in particular discussed.

2. PROPERTIES OF A TOROIDAL GRATING

The basic optical configuration of a toroidal grating-spectrometer is shown in Fig. 1. The entrance slit, the vertex of the grating and the diffracted image lie on the Rowland circle. In the usual Rowland circle mounting, the equatorial and sagittal foci of a spherical diffraction grating, are not coincident. It is possible however to obtain exact stigmatic focusing at one or two points in the spectrum by using a toroidal grating[1]. In this case the equatorial radius of curvature R and the sagittal one ς fulfill the equation

$$\varsigma = R \cos\alpha \cos\beta \tag{1}$$

where α and β are respectively the angle of incidence and diffraction on the grating.

* Currently on leave from Institut für Astronomie, ETH-Zentrum Zürich, Switzerland
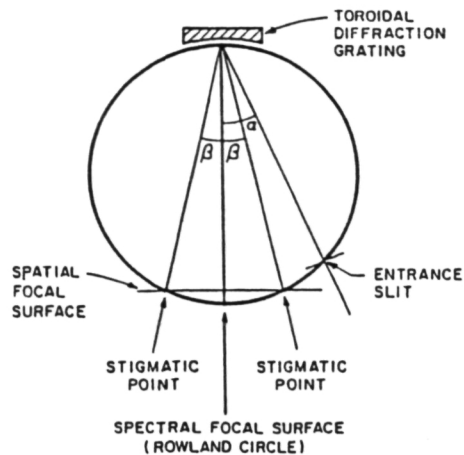
PRECEDING PAGE BLANK NOT FILMED

Figure 1. Schematic of an imaging EUV spectrometer using a single toroidal grating. Exact stigmatic focusing is obtained at the angles of diffraction ±ß.

As shown in Fig. 1 the two stigmatic points are located symmetrically with respect to the grating normal in the directions at ±ß. When in a practical system ß is relatively small there is some depth of focus especially if the aperture in the sagittal plane is quite small; consequently stigmatic focusing can be achieved on an extended region of the Rowland circle between and somewhat beyond the two stigmatic points.

The aberrations theory of a toroidal grating has been developed by Haber[2]. As usual the optical path from the source A to the image B is expanded in a power-series of the coordinates y,z of a point P on the grating surface:

$$AP + PB = \Sigma_{ij} \, a_{ij} y^i z^j \tag{2}$$

the y-axis is perpendicular and the z-axis is parallel to the grooves. In general the higher order a_{ij} coefficients are progressively smaller and correspond to the various aberrations. When working on the Rowland circle and at the stigmatic points the aberrant terms are zero up to the terms in yz^2 (i.e. the term giving rise to coma). It follows, as known, that for large focal ratios and/or for large incidence angles, even the spectral aberration, in addition to the spatial one, can be intolerably high. For correcting these higher order aberrations it is necessary to shape the surface of the grating beyond the simple toroidal surface.

3. A TOROIDAL GRATING FOR THE ULTRAVIOLET CORONAGRAPH (UVCS) ON SOHO

The SOHO (Solar and Heliospheric Observatory) Mission, approved in 1987 is a joint ESA-NASA mission. It will consist of a satellite orbiting around the Lagrangian L_1 point and carrying on board several experiments for the observation of the solar corona, the solar interior and for in-situ measurements. The launch is presently foreseen in 1995. One of the selected experiment is the UVCS, an Ultraviolet Coronagraph Spectrometer; it will study the extended corona up to ten solar radii, by measuring the light scattered by the corona at several wavelengths: Lyα HI, 1032-1036 Å OVI, 780 Å NeVIII, 625 Å MgX. Both the intensity and the profile of the lines will be measured, deriving values for the electron and ions temperature, density and velocity[3].

An optical scheme of the proposed UVCS is shown in Fig. 2. Briefly, an occulted telescope (off-axis parabola) forms the image of a portion of the solar corona, perpendicular to the radial direction, on the entrance slit of a spectrograph. The parabola can scan the corona at various distances from the sun; furthermore the entire UVCS can rotate around the axis joining the spacecraft to solar centre in order to probe the entire corona. The spectrograph is fitted with a toroidal grating and produces the diffracted images of the entrance slit on bidimensional MAMA type detectors (Multi Anode Microchannel Array). For efficiency reasons separate channels are provided for the Lyα and the other lines.

The essential parameters of the entire experiment and of the toroidal gratings in particular are reported in Table I. One can see that the f-number of the grating is not very large; also the incidence angle is small. Consequently the aberrations predicted by the theory of the toroidal grating are small.

Fig. 3 shows the spectral and spatial blurs predicted by a ray-tracing program for several source points located at various heights on the entrance slit. It is quite apparent how
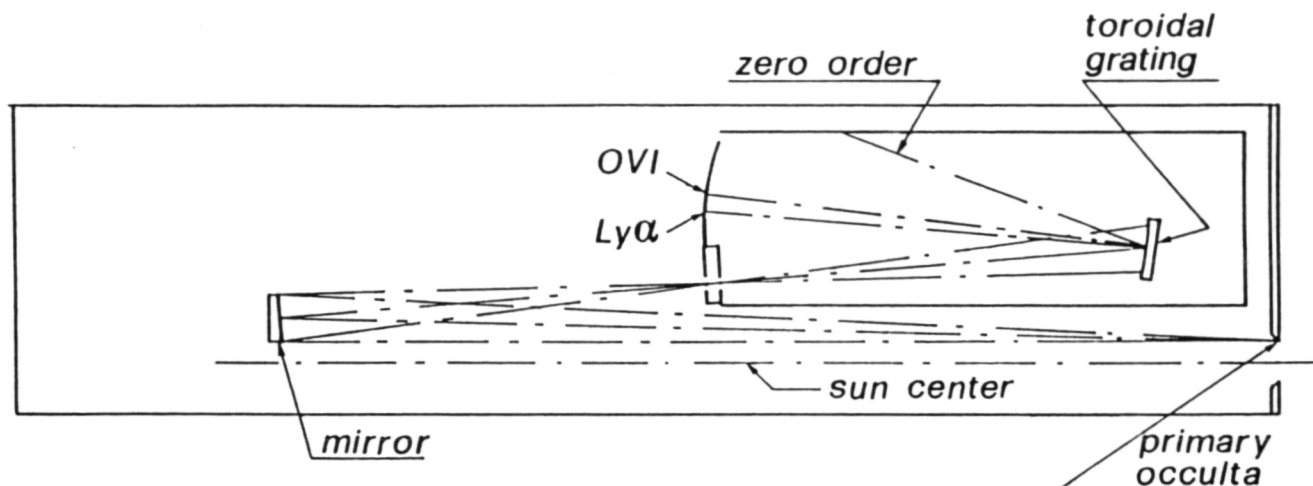
Figure 2. Optical layout of the ultraviolet coronagraph. The telescope, which is an off-axis parabola, is externally and internally occulted in order to reject the light from the full disk.

Table I. Optical Specifications of the UVCS

Telescope	Spectrometer
Size: 70 (disp) x 50 mm^2	Grating size 105 (disp) x 70 mm^2
Figure: Off-axis parabolic mirror	Figure: toroidal
	Radius: 750 mm
Focal length: 750 mm	Radii ratio R/ϱ: 1.0259 (Lyα)
Image scale : 0.22 mm/arcmin	: 1.0215 (1032 Å)
Field of view: 42'(tang) x 141'	Ruling Frequency: 2400 ℓ/mm
	Recipr. disp. : 5.63 Å/mm (1°ord)

Figure 3. Blurs obtained by ray-tracing the toroidal grating proposed for the UVCS. The full extent of the spatial (dotted lines) and spectral (solid lines) aberrations for several points on the entrance slit are reported: z is the height above the equatorial plane of the source point.

the blurs increase by going out of the equatorial plane but, for a central region they re-
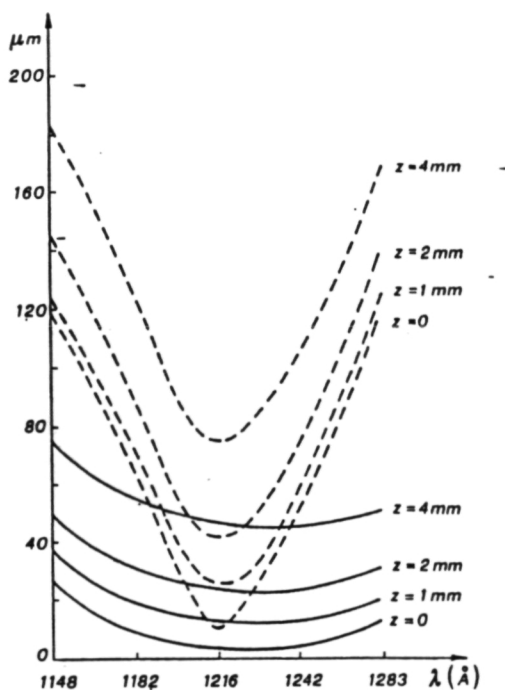main below the pixel size of 25 x 25 μm² that will be adopted for the MAMA detectors. In par-
ticular very good spectral resolution can be obtained in-plane.

4 . A CORRECTED TOROIDAL GRATING FOR LYMAN

The Lyman (previously FUSE) Mission, presently at the phase A study at both ESA and NASA,
is intended to observe stellar objects in the very important, yet unexplored region, from
1200 Å down to the HI photoionization limit at 912 Å.

Basically Lyman will consist of a Wolter type two telescope with high resolution (1" HEW),
followed by some spectrographs on the focal plane. Detection will be done with photon coun-
ting detectors[4]. In order to achieve the planned scientific objectives two, somewhat conflic-
ting, requirements: high resolution ($\approx$30.000) and high-throughput (total effective area of
$\approx$50 cm²) should be fullfilled.

Two spectrographs have been studied up to now as possible candidates: an echelle confi-
guration and a Rowland mounting[5]. The main advantage of the echelle is the intrinsic high
resolution; this propriety results very good in relaxing the constraints for the pointing
stability of the spacecraft as well as for the thermal distortion of the spectrograph struc-
ture; however, due to the large number of reflecting surfaces, the efficiency, especially
below 1050 Å (the LiF limit) is very low. On the other hand, a Rowland configuration, using
a properly corrected grating, presents a high efficiency (only one reflection), but on the
contrary for achieving high resolution it will need very high pointing stability and it will
be very sensitive to thermal distortion of the structure. However the Rowland option appears
highly desirable in the region 912-1050 Å, and also at shorter wavelengths for planetary
objects.

An optical scheme of the system is shown in Fig. 4. One can see the Wolter type two tele-
scope illuminating the entrance slit, followed by a grating and a MAMA type detector. Table
II reports the parameters of the system. Note that the key elements characterizing the gra-
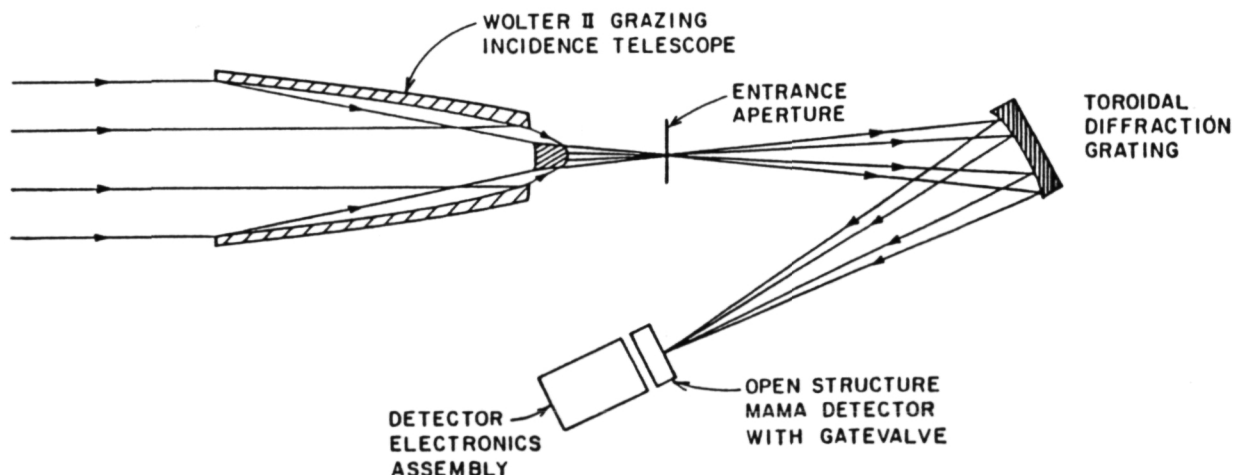
Figure 4.   Schematic of the Lyman telescope and spectrograph using a coma-corrected toroi-
dal grating.

Table II.   Optical characteristics of the Lyman mission

Telescope	Spectrograph
Figure: Wolter type two	Figure: aspheric grating
Diameter: 80 cm	Size: 200 cm diameter
f number: 10	f number: 10
Lenght : 240 cm	Radius : 200 cm
Effective collecting area 1250 cm² (300-1216 Å)	Ruling frequency: 4600 ℓ/mm

ting are: i) the f-number = 10; ii) the ruling frequency = 4600 lines/mm. The latter in particular implies that, in order to have the central wavelengths of 982 Å near the grating normal, the incidence angle α should be equal to 26.8°.

A simple toroidal grating with such parameters produces of a point source located at the centre at the entrance slit an image very wide. Fig. 5 a) shows a spot diagram of the image for $\lambda = 982$ Å for such case. A large blur is present. By introducing as proposed by Cash[6] an extra deformation of the surface of the type $k \cdot yz^2$ on top of the toroidal surface with the optimal value of $k=4.0 \times 10^{-9}$ mm^{-2} *, an image much smaller both in the spectral and spatial direction respectively can be obtained as shown in Fig. 5 b). One can see that the improvement on the aberrations is about a factor 3-4. A further correction in the spectral direction can be obtained by applying an additional correction to the surface of the type $k' \cdot y^4$ (spherical aberration), with $k'=1.9 \times 10^{-12}$ mm^{-3}. The corresponding curve is shown in Fig. 5 c), an image ab. 20 μm wide in the spectral direction is obtained corresponding to a resolution larger than 30.000.
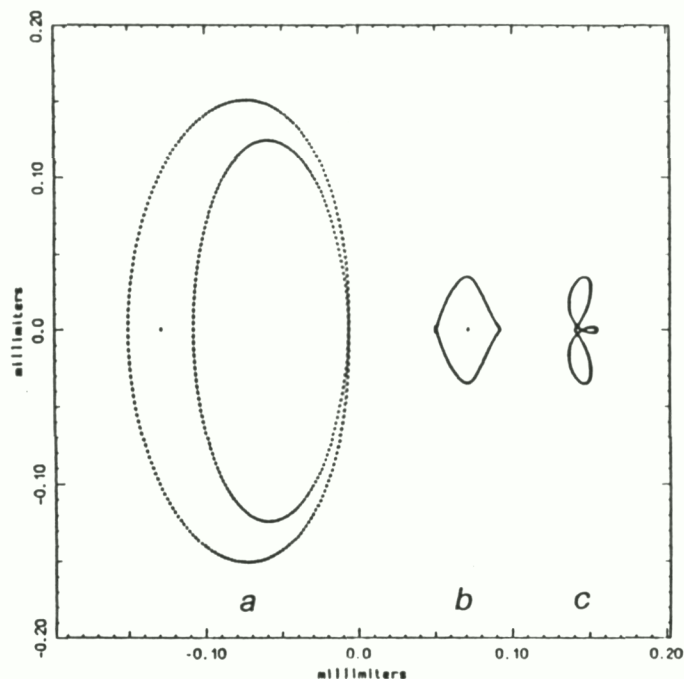

Figure 5.   The image obtained with ray-tracing for the grating proposed for Lyman at 982 Å
            a): a simple toroidal grating; b): with added the coma-correction; c): with
            added the spherical aberration correction.

5. THE EFFECT OF SLOPE ERRORS

An effect that has to be taken in account in evaluating the effective resolution achievable with an optical element is the presence of slope errors i.e. errors arising in the manufacturing of the optical element. They manifest as deviations of the actual surface from the ideal one. Their effect on the spectral resolution is particularly serious at grazing incidence and in fact it is well known in the synchrotron light source community[7]. It is not negligible however even at normal incidence.

In Fig. 6 the image obtained for the previously treated case of the grating for the Lyman is shown respectively for the two cases of extra correction without and with slope errors. For the latter case two values have been considered: in one case a value of 1 μrad

* Note that the value of k adopted here and verified as the optimal one is given by:

$$k= \frac{1}{2(\cos\alpha+\cos\beta)} f(\alpha,\beta)$$

where $f(\alpha,\beta)$ is a somewhat complicated function of the angles α and β. This in contrast to the value adopted by Cash[6] as given by:

$$k= \frac{1}{2(\sec\alpha+\sec\beta)} f(\alpha,\beta)$$

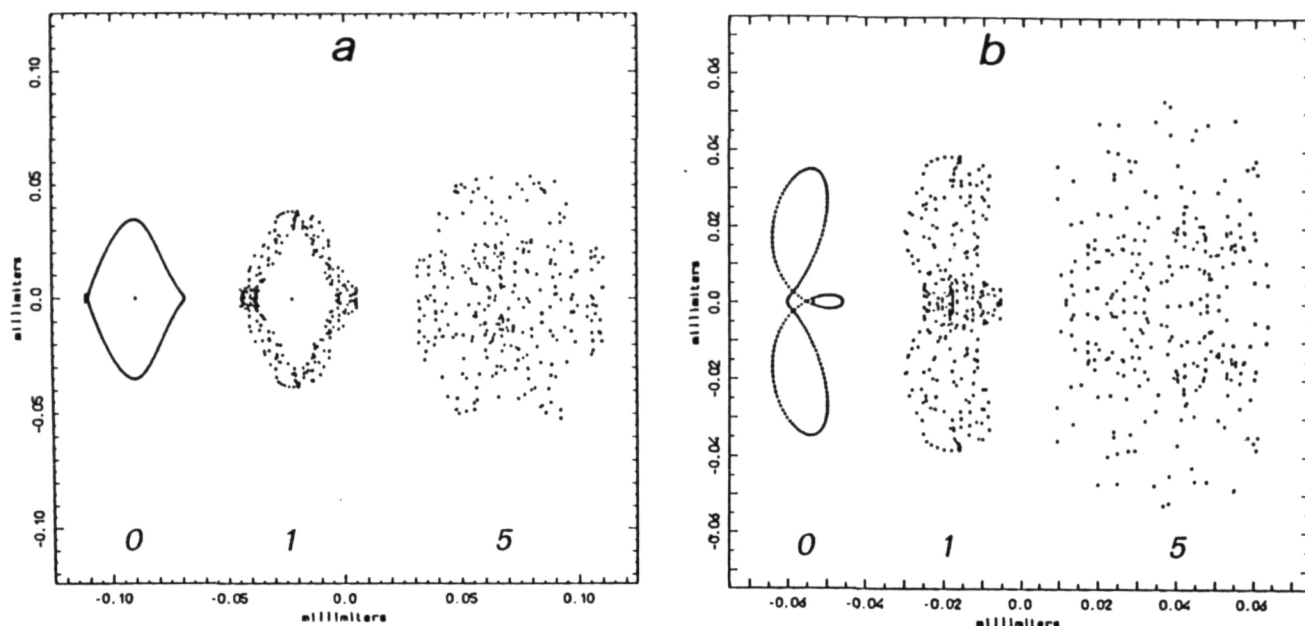For near normal incidence there is very little difference between the two.

Figure 6. The image calculated for the grating proposed for Lyman a) coma-corrected gra -
ting without and with the slope errors (1 and 5 μrad maximum); b) spherical aber-
ration corrected grating without and with the slope errors (1 and 5 μrad maximum)

maximum slope error, typical of the best spherical surfaces obtainable; and a value of 5
μrad maximum slope error, representative of the best aspherical surfaces. It is immediately
evident that the slope errors degrade considerably the performances even in the case where
only the $k \cdot yz^2$ correction is applied to the grating. It is therefore very important to try
to fabricate a grating with slope errors as small as possible.

6. GRATING FABRICATION

We have developed a method for fabricating toroidal gratings using a technique of elastic
deformation. The details of the method and its properties have been fully treated elsewhere[8].
Briefly, the process consists in ruling a grating on a concave spherical master and replica-
ting it on an intermediate convex surface. Then the grating is replicated on a stainless
steel flexible substrate accurately polished, while it is in the relaxed state i.e. the
surface is spherical. The flexible substrate is mounted on a special holder that is capable
of applying distorting forces. The final shape of the flexible substrate depends on the way
on which the flexible blank is built and on the way in which the forces are applied.

A simple toroidal surface can be obtained by applying a single adjustable distorting for-
ce. For obtaining a deformation proportional to yz^2 a more complicated pattern of forces
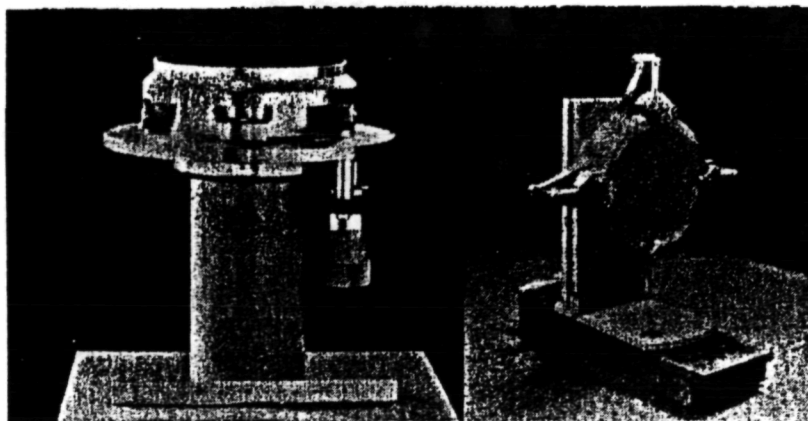has to be applied. Figs. 7 a,b show respectively the blank for obtaining a pure toroid and.

Figure 7. a): the blank for producing a simple toroidal grating; b): the blank for produ-
cing a coma-corrected toroidal grating.

the one for obtaining the coma correcting deformation. After the substrate has been shaped in the suitable aspect ratio, a fixed concave toroidal grating is replicated from it, again by using an intermediate convex replicating surface.

The aspects ratio of the toroidal surface on the flexible blank can be determined using a modified laser-illuminated version of the Twyman-Green interferometer as fully described in ref.8. Note that this method of producing aspheric gratings presents several advantages:
i)   with only one master grating whole families of toroidal or coma corrected gratings can be produced
ii) being the process of elastic deformation very well adjustable, the aspect ratio R/ς of the grating can be finely controlled
iii) by using properly shaped elastic blanks and holders there is the possibility of imparting accurately controlled deformations and in principle to control higher order aberrations
iv) by using spherical blanks at the beginning of the cicle of replication, the slope errors should be kept to a minimum, in contrast to the method of directly grinding an aspheric blank.

7. GRATING PERFORMANCES

The entire process of grating manufacturing has already been tested by measuring the performances of simple toroidal gratings. As a test case a grating with a ruling frequency of 3600 lines mm^{-1}, an active area of 70 x 70 mm^2 and radii R=1011, ς =989 mm has been produced and tested. For the test the equipment represented in Fig. 8 has been used. A hollow cathode, He-filled lamp illuminates the grating that is positioned inside a specially built normal incidence spectrograph. In place of the entrance slit a series of ten pinholes separated by 250 μm was employed. The diameter of the pinholes varied from 10 to 33 μm. In the image position on the Rowland circle is located a glass plate coated with a TBP phosphor. This phospor down converts EUV photons into visible light with a peak emission near 4300 Å. The visible light images, viewed through a window in the vacuum tank are imaged, magnified by a factor of three, onto the photocathode of a visible light MAMA type detector. This system gives an effective spatial resolution for each detector pixel of ab. 8 μm on the Rowland circle of the spectrograph.

An example of one dimensional cut through the line of the ten pinholes is shown in Fig.9. The measurement has been made at 584 Å, HeI where the intensity was sufficiently high. The pinholes are clearly well separated. A throughout analysis of the data has shown that the aberrations produced by the grating are well in agreement with the ray tracing results, indicating that no particular anomaly is present[9].

More recently we have started developing a coma-corrected toroidal grating. Again, for ease of testing a 1000 mm starting radius of the blank was chosen, an effective area of 120 mm diameter and a ruling frequency of 1200 ℓ/mm. A flexible blank with the proper holder has been built. Fig. 10 shows preliminary results of induced deformations on the blank as was shown in Fig. 7b. Fig. 10a shows the interference pattern on the blank in the relaxed
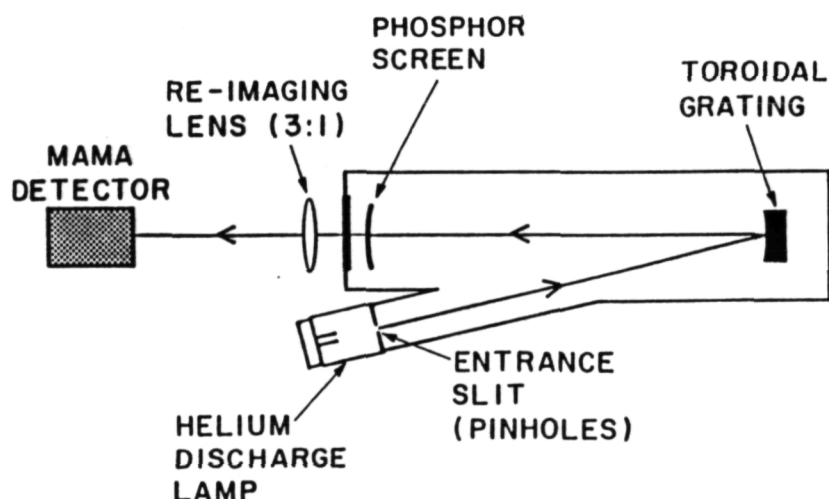

Figure 8. Schematic of the optical system for the tests of the toroidal gratings.
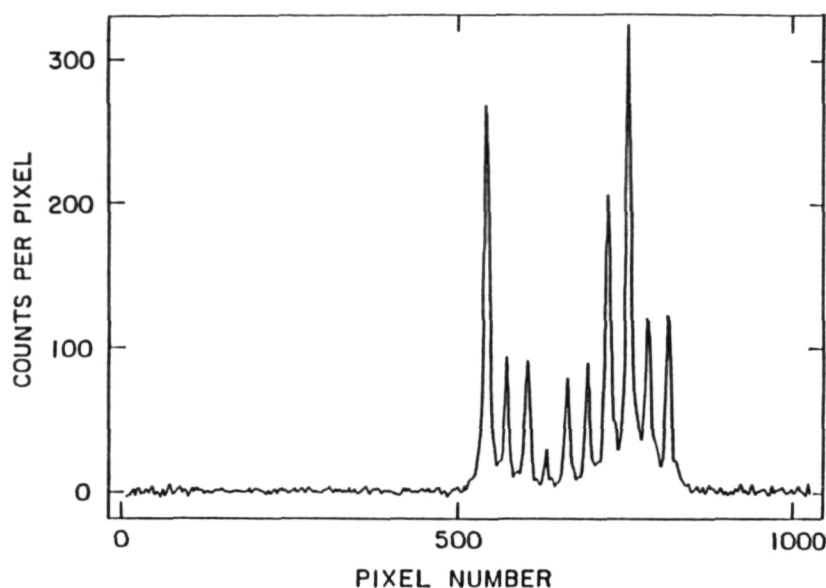
Figure 9. One dimensional image at the wavelength of the HeI resonance line at 584 Å of ten pinholes located along the spectrograph entrance slit. The different pinhole diameters result in different relative peak intensities.
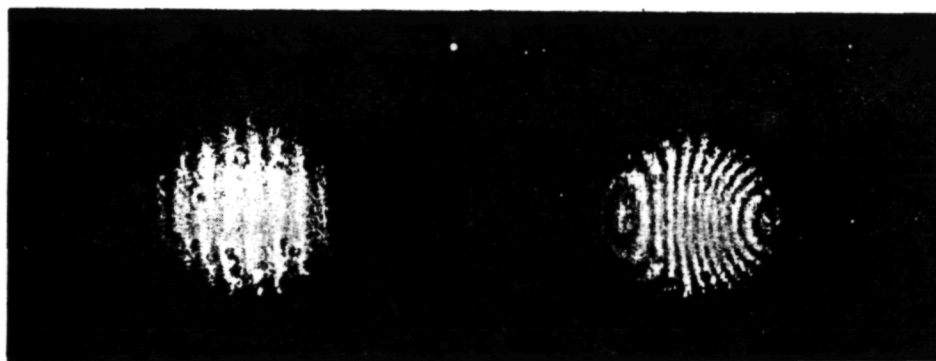

Figure 10. Fringe pattern produced by the grating: a): before deformation; b): with an approximate yz^2 deformation for coma correction.

state with the fringes quite straight and uniformely spaced. Fig. 10b shows an example of yz^2 deformation. The pattern looks remarkably good although not yet optimal (e.g. the straight fringe is not in the centre) indicating a non-optimal deformation around the y-axis; the deformation around z on the contrary seems rather good. The main toroidal deformation is not shown here for clarity.

8. CONCLUSIONS

The process of fabricating gratings by the technique of elastic deformation has been successfully tested in the case of a toroidal surface and is presently being applied to the case of coma-correcting surfaces. The use of these gratings for space experiments has been illustrated for the cases of the Ultraviolet Coronagraph on SOHO and for the spectrograph on Lyman. Tests are planned also for measuring the diffraction efficiency of such gratings.

9. REFERENCES

1. M.C.E. Huber and G. Tondello, Appl. Opt. 18, 3948 (1979).
2. H. Haber, J. Opt. Soc. Am., 40, 153 (1950).
3. J.L. Kohl, Proposal to ESA-NASA P-1795 Smithsonian Astrophysical Observatory (1988).
4. H.W. Moos, Proposal to NASA, J. Hopkins. University (1986).
5. Lyman Phase A report, ESA (1988).
6. W.C. Cash, Appl. Opt., 23, 4518 (1984).
7. G.P. Williams, Nucl. Instrum. and Meth. A246, 294 (1986).
8. M.C.E. Huber, J.G. Timothy, J.S. Morgan, G. Lemaitre, G. Tondello, E. Jannitti and P. Scarin, Accepted for publication on Appl. Opt. (1988).

HiRES: a high-resolution stigmatic extreme ultraviolet spectroheliometer for studies of the fine-scale structure of the solar chromosphere, transition region, and corona

J. Gethyn Timothy, MEMBER SPIE
Thomas E. Berger, MEMBER SPIE
Jeffrey S. Morgan
Arthur B. C. Walker, Jr., MEMBER SPIE
Stanford University
Center for Space Science and
    Astrophysics
Stanford, California 94305-4055

Surendra K. Jain
Ajay K. Saxena, MEMBER SPIE
Jagadish C. Bhattacharyya
Indian Institute of Astrophysics
Bangalore 560034, India

Martin C. E. Huber
European Space Agency
Space Science Department
ESTEC Postbus 299
NL-2200 AG Noordwijk, The Netherlands

Giuseppe Tondello
Giampiero Naletto
Università di Padova
Istituto di Elettronica
I-35100 Padova, Italy

Abstract. We describe the design of a high-resolution stigmatic extreme-ultraviolet (EUV) spectroheliometer, configured for flight on a Black Brant sounding rocket, which consists of a 45-cm Gregory telescope coupled to a spectrometer employing a single toroidal diffraction grating in a normal-incidence Rowland circle mounting and an imaging pulse-counting multi-anode microchannel array (MAMA) detector system. The toroidal diffraction grating is fabricated by a technique employing an elastically deformable submaster grating that is replicated in a spherical form and then mechanically distorted to produce the desired aspect ratio of the toroidal surface for stigmatic imaging over the selected wavelength range. The spectroheliometer will produce spatially resolved spectra of the chromosphere, transition region, and corona with an angular resolution of 0.4 arcsec or better, a spectral resolution $\lambda/\Delta\lambda$ of about 10^4 in first order, and a temporal resolution of the order of seconds. Because of the geometric fidelity of the MAMA detector system, the spectroheliometer will be able to determine Doppler shifts to a resolution of at least 2 mÅ at wavelengths near 600 Å ($\sim$1.0 km s^{-1}), depending on the level of the accumulated signal. The unique characteristics of the spectroheliometer will be used in combination with plasma-diagnostic techniques to study the temperature, density, and velocity structures of specific features in the solar outer atmosphere.

Subject terms: x-ray/EUV optics; spectroheliometer; solar EUV spectroscopy; Gregorian telescopes; toroidal gratings.

CONTENTS

1. INTRODUCTION

Our proposal to construct a high-resolution stigmatic EUV spectroheliometer (HiRES) for flight on a Black Brant sounding rocket has been accepted by NASA, the Italian Space Agency (ASI), and the Indian Institute of Astrophysics. The instrument, now under development, will make it possible to observe the solar chromosphere, transition region, and corona with spatial, spectral, and temporal resolutions of, respectively, 0.4 arcsec,

$\lambda/\Delta\lambda \sim 10^4$ (in first order), and seconds. The payload consists of a 45-cm Gregory telescope and a spectrometer that is equipped with a toroidal diffraction grating as its single reflective element. The spatially resolved spectra produced by the grating will be recorded by an imaging, pulse-counting multi-anode microchannel array (MAMA) detector. The high resolution and the access to the EUV wavelength range will permit a comprehensive investigation of small-scale coronal structures since the entire range of plasma at chromospheric, transition region, and coronal temperatures can be observed in detail and at the same time. Dynamics can also be studied, because Doppler shifts of at least 2 mÅ at wavelengths around 600 Å, corresponding to velocities of 1 km s^{-1} or less, will be observable. In addition, the HiRES instrument can be used for in-flight radiometric calibration of the coronal diagnostics spectrometer (CDS), the solar ultraviolet measurements of emitted radiation (SUMER) instrument, and the ultraviolet coronagraph spectrometer (UVCS) on the ESA/NASA Solar and Heliospheric Observatory (SOHO) spacecraft.[1] We review the scientific objectives of the investigation and describe the configuration of the HiRES payload.

2. SCIENTIFIC OBJECTIVES

The scientific objectives of the observing program are to address currently unanswered fundamental questions concerning the fine-

scale structure of the chromosphere, transition region, and corona. The unique characteristics of the spectroheliometer will be utilized in combination with plasma-diagnostic techniques to study the temperature, density, and velocity structures of specific features in the solar outer atmosphere.[2] The goal is to seek a unified understanding of the interplay between the time-dependent geometry of the magnetic field structure and the associated flows of mass and energy, the key to which lies in the smallest spatial scales that are unobservable with current EUV instruments.[3,4]

To understand the origins of the rather extreme physical conditions encountered in the solar outer atmosphere requires detailed studies of the mechanisms by which structure is imposed on the atmospheric plasma, by which energy and mass are transported between different thermal layers, and by which energy transported from one level is dissipated in another. Studies during the past decades have revealed that magnetic fields permeate the solar atmosphere at all levels, and are responsible for constraining and heating plasma in the outer atmosphere, storing energy and mass that occasionally is released explosively, and transporting heat into the chromosphere and corona from the kinetic motion reservoir in the subphotospheric convection zone. Furthermore, the magnetically moderated flows of high-energy radiation and particles provide a unique coupling between the sun, its planetary system, and structures, and events that we observe on the solar surface must be repeated on countless other stars in the galaxy. Accordingly, observations of magnetic fields and dynamic phenomena on the sun provide fundamental insights concerning not only the detailed physical state of the heliosphere and its interface with planetary magnetospheres and interstellar space but also the magnetic phenomena that occur continually on larger and, often, more energetic scales elsewhere in the universe. We can study these phenomena on the sun with a clarity that is unattainable in other astrophysical situations.[5] With these themes in mind, we have begun the development of the high-resolution EUV spectroheliometer. Observations from space over the past two decades have shown that simultaneous measurements over a wide range of excitation temperatures with very high spatial, spectral, and temporal resolutions are required for an understanding of the causes and effects of solar features such as coronal holes, loops, x-ray bright points and prominences,[6] and of dynamic events such as explosive events[7] and flares.[8] The EUV spectroheliometer, as currently configured, will be capable of observing simultaneously at excitation temperatures over the range from 3×10^4 to 2×10^6 K, with a spatial resolution of 0.4 arcsec or better, a spectral resolution in first order $\lambda/\Delta\lambda \sim 10^4$, and a temporal resolution of seconds or less. These capabilities are, we believe, adequate to start addressing the fundamental scientific questions concerning the flow of mass and energy in the outer solar atmosphere.

3. HIGH-RESOLUTION EUV SPECTROHELIOMETER

The design of the EUV spectroheliometer is based on two key technology developments that we have undertaken during the past decade, namely the fabrication of toroidal diffraction gratings using deformable optics and the fabrication of state-of-the-art, pulse-counting, imaging photoelectric detector systems. The spectroheliometer has been designed from the outset to provide complementary data to that from high-resolution x-ray, ultraviolet, and visible-light instruments [e.g., the high-resolution telescope spectrometer (HRTS)[9] and the Orbiting Solar Laboratory (OSL)[10]]. The configuration of the HiRES payload on the Black Brant sounding rocket is shown in Fig. 1, and the key

characteristics of the telescope, imaging EUV spectrometer, and EUV detector system are given in Table 1.

Two ancillary instruments are also included in the payload. These are an EUV irradiance spectrometer and an imaging infrared (IR) spectrometer. The key characteristics of these instruments are given in Table 2.

The basic configuration of the imaging EUV spectrometer mounting is shown in Fig. 2(a). In the conventional Rowland circle mounting, the vertical and horizontal foci from a spherical diffraction grating are not coincident. However, one can obtain exact stigmatic focusing at two points in the spectrum[11] by selecting the vertical radius of curvature R_V of a toroidal grating to be smaller than its horizontal radius R_h. Exact stigmatic focusing can then be obtained at two positions in the spectrum, given by

$$R_V = R_h \cos\alpha \, \cos\beta_0 . \tag{1}$$

The two stigmatic points are located symmetrically to the grating normal at the angles of diffraction $\pm \beta_0$, as shown in Fig. 2(a). An isometric display of the imaging properties of the two stigmatic points is shown in Fig. 2(b).

In a practical system where β_0 is small and there is some depth of focus (moderate speed systems with focal ratios $\sim f/15$ or greater), stigmatic focusing can be achieved between, and somewhat beyond, the two stigmatic points with a simple toroidal surface. A wavelength range of over 100 Å can be obtained with very high image quality, and a much greater wavelength range can be covered with moderate image quality with a single grating.

To evaluate this concept, we obtained a 3600-grooves mm^{-1} spherical master grating with a radius of curvature of 1 m from Hyperfine Inc. of Boulder, CO. This grating was successfully replicated onto a deformable concave blank, and several fixed toroidal gratings were replicated by using the deformable submaster grating. A series of tests of these toroidal diffraction gratings combined with the imaging MAMA detector systems have been completed, and the results have been described in the literature.[12,13]

The development of the imaging MAMA detector systems has proceeded at a fast pace in recent years under the impetus of the Hubble space telescope imaging spectrograph (STIS) and SOHO flight programs. MAMA detector systems with formats as large as 2048×2048 pixels and with pixel dimensions as small as 14×14 microns^2 have been fabricated and are now under evaluation.[14] Different anode array geometries have been developed; the latest version, the fine-fine geometry, is now the standard for all new detector formats (see Fig. 3). Anode arrays for all these detector configurations have been fabricated free of defects. The theoretical spatial resolution of 14 microns (FWHM) has been demonstrated with the (224×960)-pixel arrays fabricated for the FUSE/Lyman phase A study, and measurements made with a first-generation coarse-fine geometry (256×1024)-pixel MAMA detector system with 25-micron pixels have demonstrated the capability to determine the centroid of a spot image to an accuracy of better than 0.04 pixel, i.e., less than 1 micron.[15] The HiRES imaging EUV detector will have a format of 728×2808 pixels, pixel dimensions of 14×14 microns^2, and will be accommodated in the 40-mm format open-structure MAMA detector tube. The HiRES detector system will utilize the new custom amplifier/discriminator and decode[16] integrated circuits, now being developed as part of the STIS and SOHO
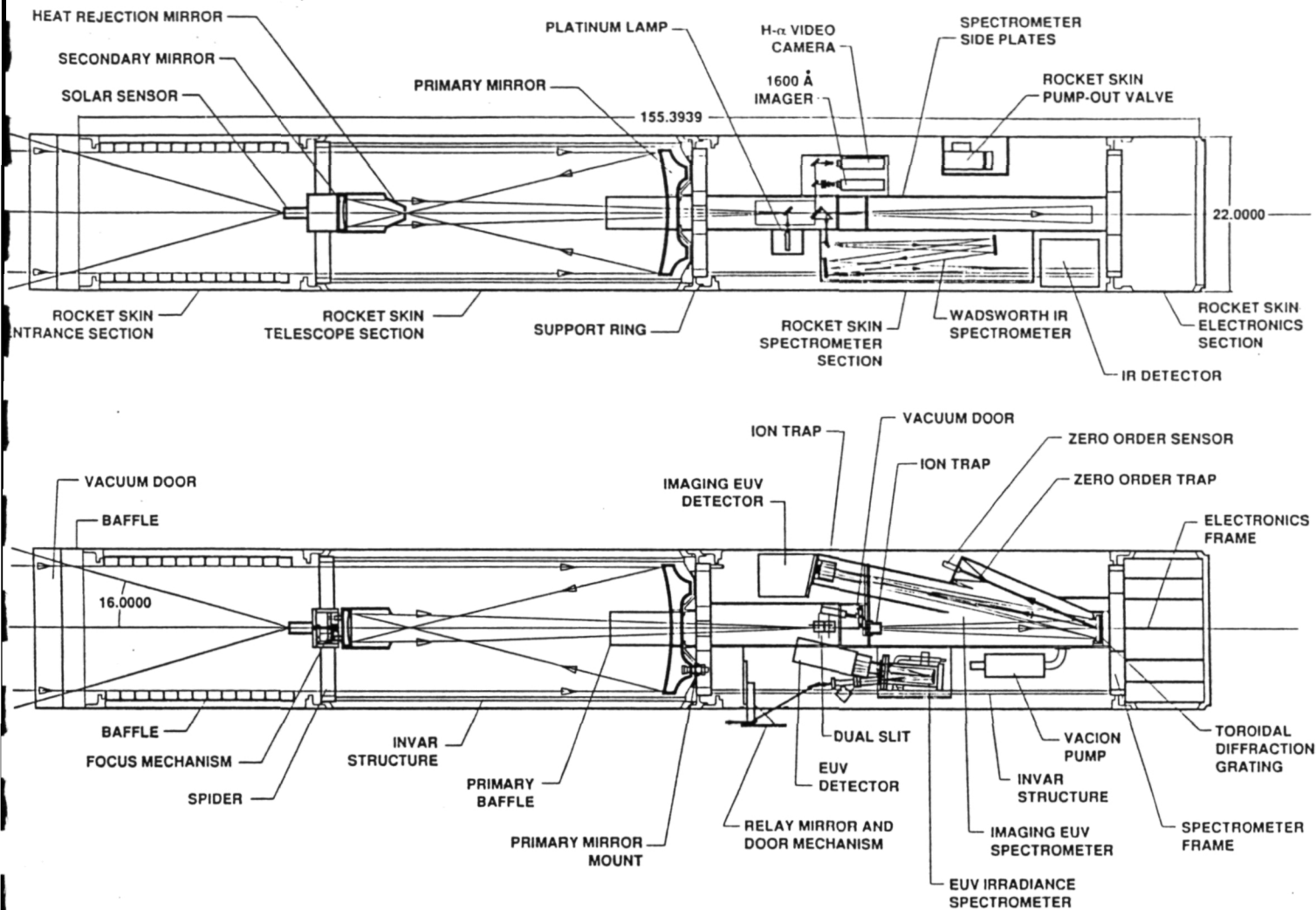
Fig. 1. Configuration of the HiRES payload in the Black Brant sounding rocket.

programs. An opaque MgF_2 photocathode, deposited on the front face of the microchannel plate, will be used for the studies at wavelengths near 600 Å in order to provide a high level of rejection of scattered H Ly α 1216 Å radiation. An opaque KBr photocathode will be used for the later studies near 1200 Å in order to provide a high detective quantum efficiency (DQE) at these wavelengths.

An additional EUV instrument included in the payload is the EUV irradiance spectrometer. This spectrometer employs a 0.25-m

TABLE 1. Characteristics of the high-resolution EUV spectroheliometer for a Black Brant sounding rocket.

TELESCOPE:

Type: f/15 Gregorian with f/2.0 primary mirror
Diameter of primary mirror: 450 mm
Focal Length: 6750 mm
Plate scale in the focal plane: 33 μm per arc sec.

SPECTROMETER:

Type: Rowland mounting with toroidal grating
Entrance slit: 14 μm by 6.2 mm
Instantaneous field-of-view: 0.4 arc sec by 3.0 arc min
Grating ruling frequency: 3600 grooves mm^{-1} (initial flights)
Grating radius-of-curvature: 1000 mm (mean)
Angle of incidence: 11.95°
Aspect ratio of toroid: 0.9782
Stigmatic wavelength range: ~120 Å from ~510 Å to ~630 Å in first order
Spectral resolution (2 detector pixels): 78 mÅ

DETECTOR:

Type: Open-structure Multi-Anode Microchannel Array (MAMA)
Format: 728 x 2808 pixels (fine-fine configuration)
Total number of amplifiers: 160
Pixel dimensions: 14 x 14 μm^2
Position sensitivity: <1 μm (signal-to-noise limited)
Photocathode material: MgF_2 or KBr

TABLE 2. Characteristics of the EUV irradiance spectrometer and the Imaging IR spectrometer.

EUV IRRADIANCE SPECTROMETER:

Type: Rowland mounting with spherical grating
Entrance slit: 10 μm by 3.0 mm
Instantaneous field-of-view: 3.8° x 3.8°
ruling frequency: 1028 grooves mm^{-1}
Grating radius-of-curvature: 0.25 m
Angle of incidence: 9.0°
Wavelength range: 280 Å to 1270 Å
Spectral resolution (2 detectors pixels): 2 Å
Detector: MAMA
Detector format: 1 x 1024 pixels (fine-fine configuration)

IMAGING IR SPECTROMETER:

Type: Wadsworth mounting with spherical grating
Entrance slit: 14 μm x 6.2 mm
Instantaneous field-of-view: 0.4 arc sec by 3.0 arc min.
Grating ruling frequency: 300 grooves mm^{-1}
Grating radius-of-curvature: 4000 mm
Angle of incidence: 18.96°
Wavelength range: 10824 Å to 10834 Å
Spectral resolution (2 detector pixels): 0.45 Å
Detector: CCD
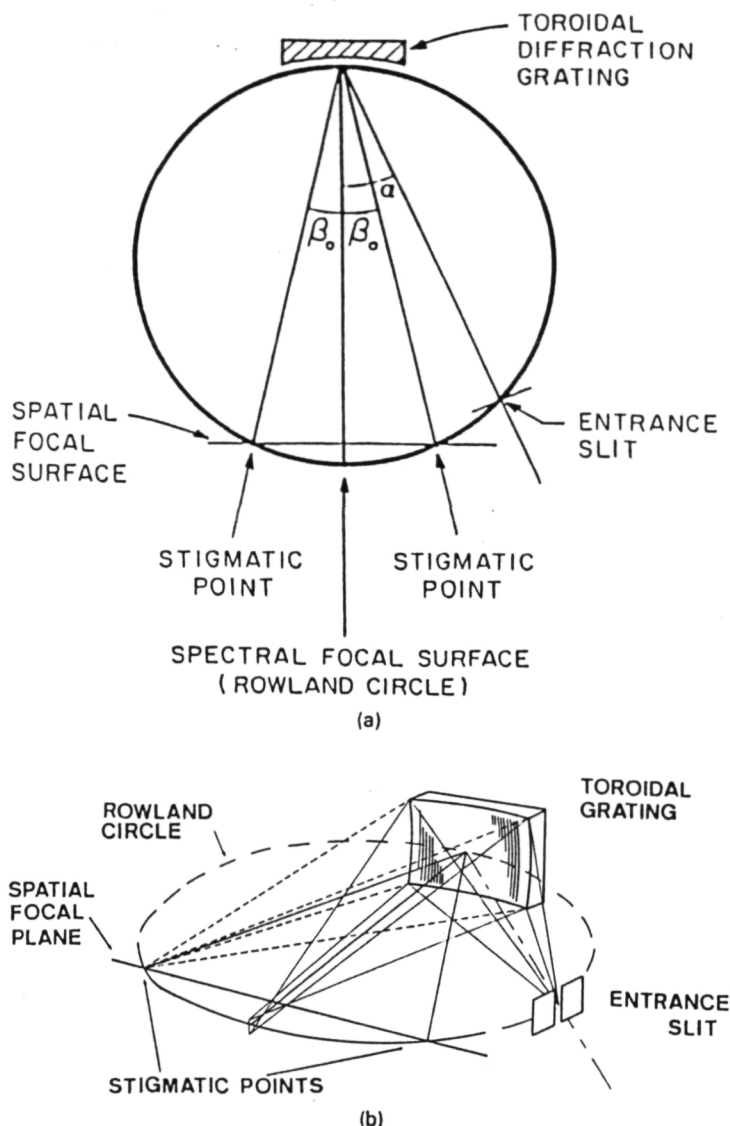Detector format: 64 x 400 pixels

(a)

(b)

Fig. 2. (a) Schematic of the imaging EUV spectrometer employing a single toroidal grating. Exact stigmatic focusing is obtained at angles of diffraction $\pm\beta_0$, which are defined by Eq. (1). Given a sufficiently small value of β_0 and some depth of focus, effective stigmatic focusing can be achieved between and somewhat beyond the two stigmatic points. (b) Isometric display of the imaging properties at the two stigmatic points $\pm\beta_0$.

radius-of-curvature concave diffraction grating, operating at an angle of incidence of 9.0 deg in a conventional Rowland circle mounting, as shown in Fig. 4. The grating ruling frequency is 1028 lines mm^{-1}, and the grating is used in the first order to provide a dispersion of 38.7 Å mm^{-1}. The entire spectrum from 1270 to 280 Å is recorded simultaneously with a (1 × 1024)-pixel MAMA detector with pixel dimensions 25 μm in width by 6.5 mm in height. The spectral resolution is approximately 2 Å (two detector pixels), and the entire spectrum is read out during flight with a temporal resolution of 1.6 s.

This instrument will be included in the payload for two reasons. First, it will provide essential data on the solar EUV irradiances. We note that no systematic measurements of the solar EUV irradiances have been made since the late 1970s.[17] Second, it will provide measurements of the EUV atmospheric extinction profiles, which will be used to correct for the effects of atmospheric absorption on the EUV spectral images. The instrument is already in hand and will be refurbished for use in the HiRES
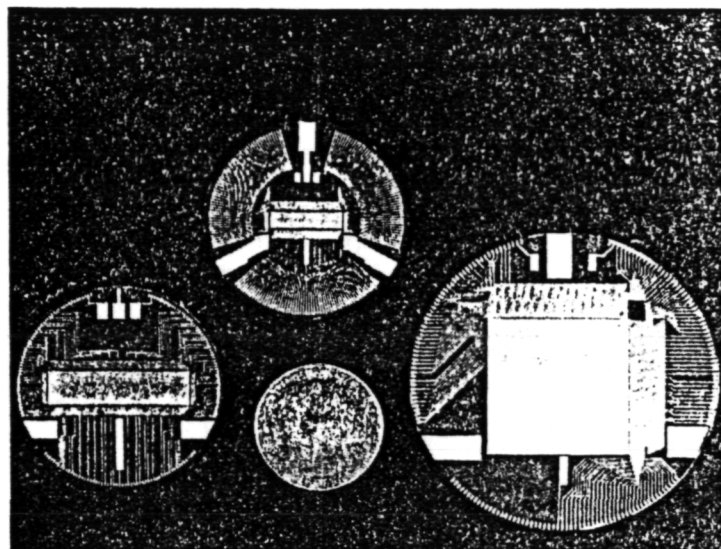

Fig. 3. Configurations of representative anode arrays for the imaging MAMA detector systems. (left) (256 × 1024)-pixel coarse-fine array with 25 × 25 microns^2 pixels; (center) (224 × 960)-pixel fine-fine array with 14 × 14 microns^2 pixels; (right) (1024 × 1024)-pixel fine-fine array with 25 × 25 microns^2 pixels.

payload. A new fine-fine geometry (1 × 1024)-pixel MAMA detector tube will be fabricated for use in the spectrometer. The detector system will also employ the new custom amplifier/discriminator and decode integrated circuits.

A third instrument that will be included in the payload is the near-IR spectrometer for imaging the He I 10,830 Å line. The purpose of this spectrometer is to record simultaneously, for the first time, high-spatial-resolution images at the He I 10,830 Å, He I 584 Å, and He II 304 Å lines. These data will be used for studies of the different line-excitation mechanisms. Based on spectral data that we have received from Dr. Jack Harvey at the National Solar Observatory (NSO), we are base-lining a Wadsworth spectrometer with a (64 × 400)-pixel imaging detector. The spectral range covered will be from about 10,824 to 10,834 Å, and the spectral resolution will be 0.45 Å (two detector pixels). This spectrometer will be mounted in tandem with the imaging EUV spectrometer; a second entrance slit, parallel to the EUV slit, will be used to capture the IR radiation and feed it to the Wadsworth optics. The very small time difference between the EUV and IR images will not impact the analyses of the scientific data.

The remaining optical instruments in the payload are the two slit-jaw monitors, namely, the Hα real-time TV camera and the 1600 Å (temperature minimum) imager. The entire HiRES payload will be evacuated before launch, and a NASA-supplied vacuum door in front of the telescope will be opened during the data-taking part of the flight. Each EUV spectrometer has an independent pumping system and a vacuum seal in front of the entrance slit. The block diagram of the payload is shown in Fig. 5.

4. PROPOSED FLIGHT PROGRAM

We foresee a number of operating modes for the HiRES payload, depending on the scientific investigation. The two primary modes will be the spectroheliogram mode and the spectral mode. In the spectroheliogram mode the SPARCS attitude control system will be used to execute a "pushbroom" scan of a region of interest on the solar disk or above the limb. At a scan rate of 0.4 arcsec/0.1 s, a region of about 3 × 3 (arcmin)^2, as shown
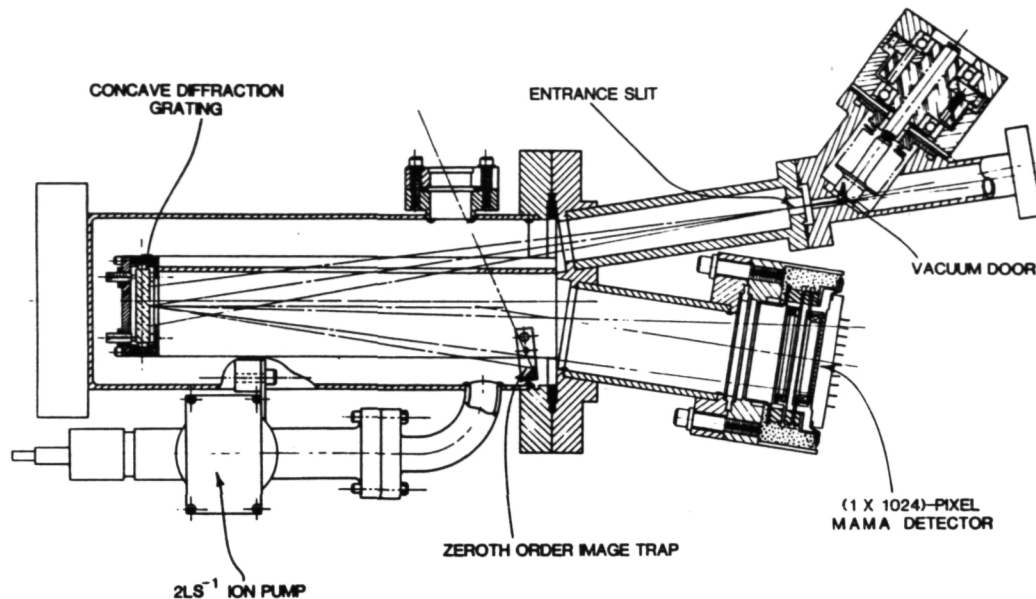
Fig. 4. Schematic of the 0.25-m EUV irradiance spectrometer.

in the EUV image[18] in Fig. 6, can be imaged in 45 s. Seven scans can be executed in the expected observing time of 300 s during a flight on the Terrier-Black Brant sounding rocket. In the spectral mode the entrance slit is placed across the region of interest, and the spatially resolved spectrum is read out with a time resolution of 0.1 s. Data selection for transmission and recording is controlled by "mask modules" in the MAMA electronics because the EUV and IR instruments are capable of producing digital data at rates in excess of 100 Mbit s^{-1}.

For the first flights we plan to observe a series of strong EUV emission lines near 600 Å. The locations of these lines on the

Rowland circle of the spectrometer and their relation to the stigmatic points are shown in Fig. 7(a). The expected output count rates for different locations on the solar disk are given in Table 3. We expect to observe some strong lines in second order in this wavelength range, particularly He II 303.78 Å and Si XI 303.41 Å, and, in centers of activity, Fe XV 284.2 Å.

The calibration of the HiRES instruments will be a major task of the instrument development program. Calibration of the EUV spectroheliometer has three components; measurement of the telescope point spread function (PSF), establishment of an absolute wavelength scale in the spectrometer, and radiometric
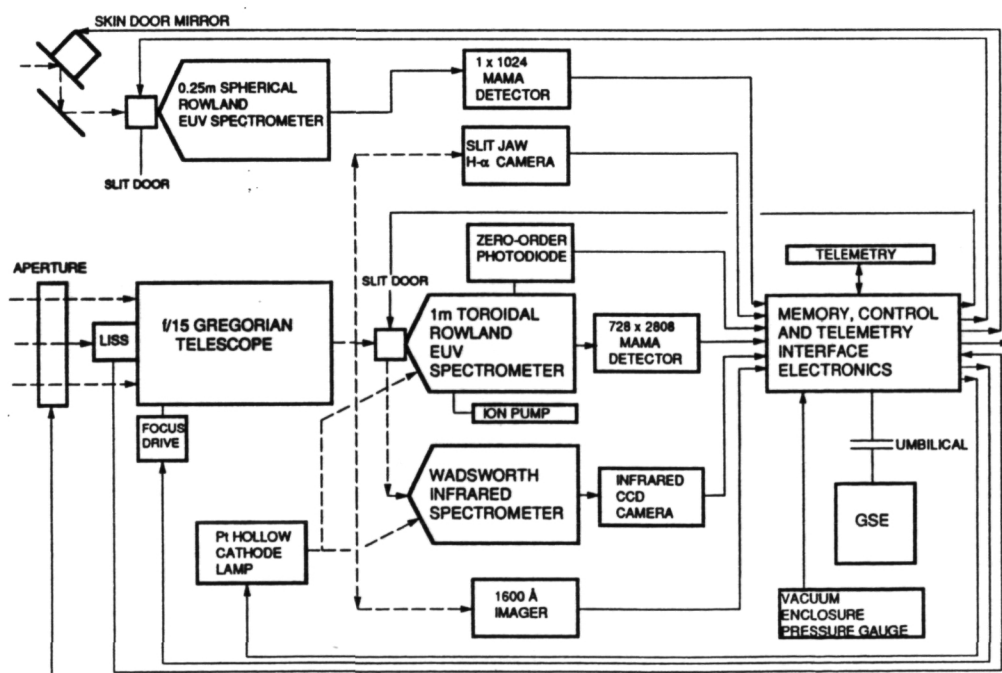
HIRES BLOCK DIAGRAM

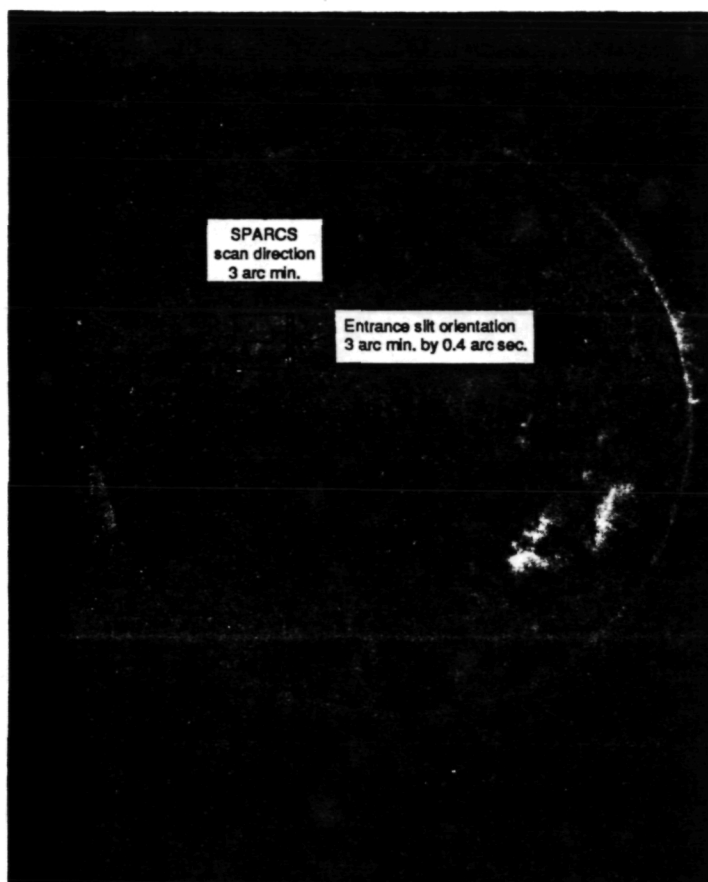**Fig. 5. Block diagram of the HiRES payload.**

Fig. 6. Spatial scan mode of the HiRES instrument shown on a 171 to 175-Å EUV image of the solar disk.

calibration of the assembled instrument. Calibrations will be carried out at the component and system levels. We plan to use the 300-m vacuum tunnel at the NASA Marshall Space Flight Center (MSFC) for the telescope PSF measurements at EUV wavelengths; the length of this tunnel is currently being increased to 1000 m for the advanced x-ray astrophysics facility (AXAF) program.

Radiometric calibration of both the imaging EUV spectrometer and the EUV irradiance spectrometer will be carried out in the laboratory using National Institutes of Standards and Technology (NIST) standard diodes and a high-current hollow-cathode light source having a calibration traceable to a storage ring as the absolute EUV standard.[19] In-flight wavelength calibration of the imaging EUV spectrometer will be accomplished by the use of a Pt-Ne hollow-cathode lamp with a MgF$_2$ window.[20] A second set of rulings, with a frequency of 1800 grooves mm^{-1},

will be located outside the primary ruled area to superimpose the emission lines at wavelengths near 1200 Å from the Pt-Ne lamp onto the imaging detector.

When the HiRES payload is used for the in-flight radiometric calibration of the CDS, SUMER, and UVCS instruments on the SOHO spacecraft, the ruling frequency of the toroidal grating will be changed from 3600 to 1800 grooves mm^{-1}. Wavelengths around 1200 Å will then be imaged in first order, and wavelengths around 600 Å will be imaged in second order. The locations of the strong solar emission lines accessible in this mode of operation and their relation to the stigmatic points on the Rowland circle are shown in Fig. 7(b).

The first flight of the HiRES payload is currently scheduled for early 1993, with reflights at approximately one-year intervals. The SOHO calibration rocket (CALROC) flights are expected to start in 1996, following the SOHO launch in late 1995.

5. ACKNOWLEDGMENTS

6. REFERENCES

1. V. Domingo and A. I. Poland, "SOHO—an observatory to study the solar interior and the solar atmosphere," in *The SOHO Mission*, ESA SP. 1104, pp. 7–12, February (1989).
2. M. C. E. Huber and G. L. Withbroe, "Contributions to solar physics from extreme-ultraviolet observations," in *Future Solar Optical Observations: Needs and Constraints*, G. Godoli, G. Noci, and A. Righini, eds., pp. 146–173, Tip. Baccini and Chiappi, Florence, Italy (1978).
3. E. N. Parker, "The future of solar physics," *Solar Physics*, 100, 599 (1985).
4. G. A. Doschek, "What's needed in the UV and EUV," in *Theoretical Problems in High Resolution Solar Physics II*, G. Athay and D. S. Spicer, eds., pp. 37–54, NASA Conference Publication 2483 (1987).
5. J. L. Linsky, "Nonradiative activity across the H-R diagram: which types of stars are solar-like?" *Solar Physics*, 100, 333 (1985).
6. G. W. Pneuman and F. Q. Orrall, "Structure, dynamics and heating of the solar atmosphere," in *Physics of the Sun*, vol. II, P. A. Sturrock, ed., pp. 71–134, Reidel, Boston (1986).
7. K. P. Dere, J.-D. F. Bartoe, and G. E. Brueckner, "Explosive events in the solar transition zone," *Solar Physics* 123, 41 (1989).
8. B. M. Haisch, "An overview of solar and stellar flare research," *Solar Physics* 121, 3 (1989).
9. G. E. Brueckner and J.-D. F. Bartoe, "Observations of high-energy jets in the corona above the quiet sun, the heating of the corona, and the acceleration of the solar wind," *Astrophys. J.*, 272, 329 (1983).
10. A. Title, "An overview of the orbiting solar laboratory," in *High Spatial Resolution Solar Observations*, Proc. Tenth Sacramento Peak Summer Workshop, O. v. d. Lühe, ed., pp. 35–50, National Solar Observatory, Sacramento Peak (1989).
11. H. Haber, "The torus grating," *J. Opt. Soc. Am.*, 40, 153 (1950).
12. M. C. E. Huber, J. G. Timothy, J. S. Morgan, G. Lemaître, G. Tondello, E. Jannitti, and P. Scarin, "Imaging extreme ultraviolet spectrometer employing a single toroidal diffraction grating: the initial evaluation," *Appl. Opt.* 27, 3503 (1988).
13. J. S. Morgan, J. G. Timothy, D. C. Slater, M. C. E. Huber, G. Tondello, E. Jannitti, G. Naletto, P. Nicolosi, and G. Lemaître, "A high-efficiency extreme ultraviolet spectrometer," in *Extreme Ultraviolet Astronomy*, R. F. Malina and S. Boyer, eds., Pergamon Press, pp. 380–389 (1991).
14. J. G. Timothy, J. S. Morgan, D. C. Slater, D. B. Kasle, R. L. Bybee, and H. E. Culver, "MAMA detector systems: a status report," *SPIE Ultraviolet Technol.* III 1158, 104 (1989).
15. J. S. Morgan, D. C. Slater, J. G. Timothy, and E. B. Jenkins, "Centroid position measurements and subpixel sensitivity variations with the MAMA detector," *Appl. Opt.* 28, 1178 (1989).

TABLE 3. Expected count rates from the EUV spectroheliometer.

ION	λ(Å)	T(K)	INTENSITY[a] (erg cm^{-2}s^{-1}sr^{-1}) Quiet Region	INTENSITY[a] Coronal Hole	INTENSITY[a] Active Region	OUTPUT COUNT RATE[b] (pixel^{-1}s^{-1}) Quiet Region	OUTPUT COUNT RATE[b] Coronal Hole	OUTPUT COUNT RATE[b] Active Region
He I	584.3	3.2×10^4	550	250	7200	189	87	2478
He I	537.3	3.2×10^4	71	34	830	22	11	271
O III	599.6	1.3×10^5	31	28	74	11	10	26
O V	629.7	2.5×10^5	330	290	1300	130	109	484
Ca X	574.0	7.0×10^5	7.8	3.1	46	3	1	15
Mg X	625.2	1.8×10^6	51	2.6	470	19	1	177
Si XII	521.1	2.2×10^6	25	-	720	8	-	224

a. From J. E. Vernazza and E. M. Reeves, *Astrophys. J. Suppl.* vol. 37, p. 485, 1978.
b. Assumes effective telescope collection area of 75 cm^2; grating efficiency 0.10; detector efficiency 0.4 counts photon^{-1} and a pixel size of 0.4 x 0.4 arc sec^2.
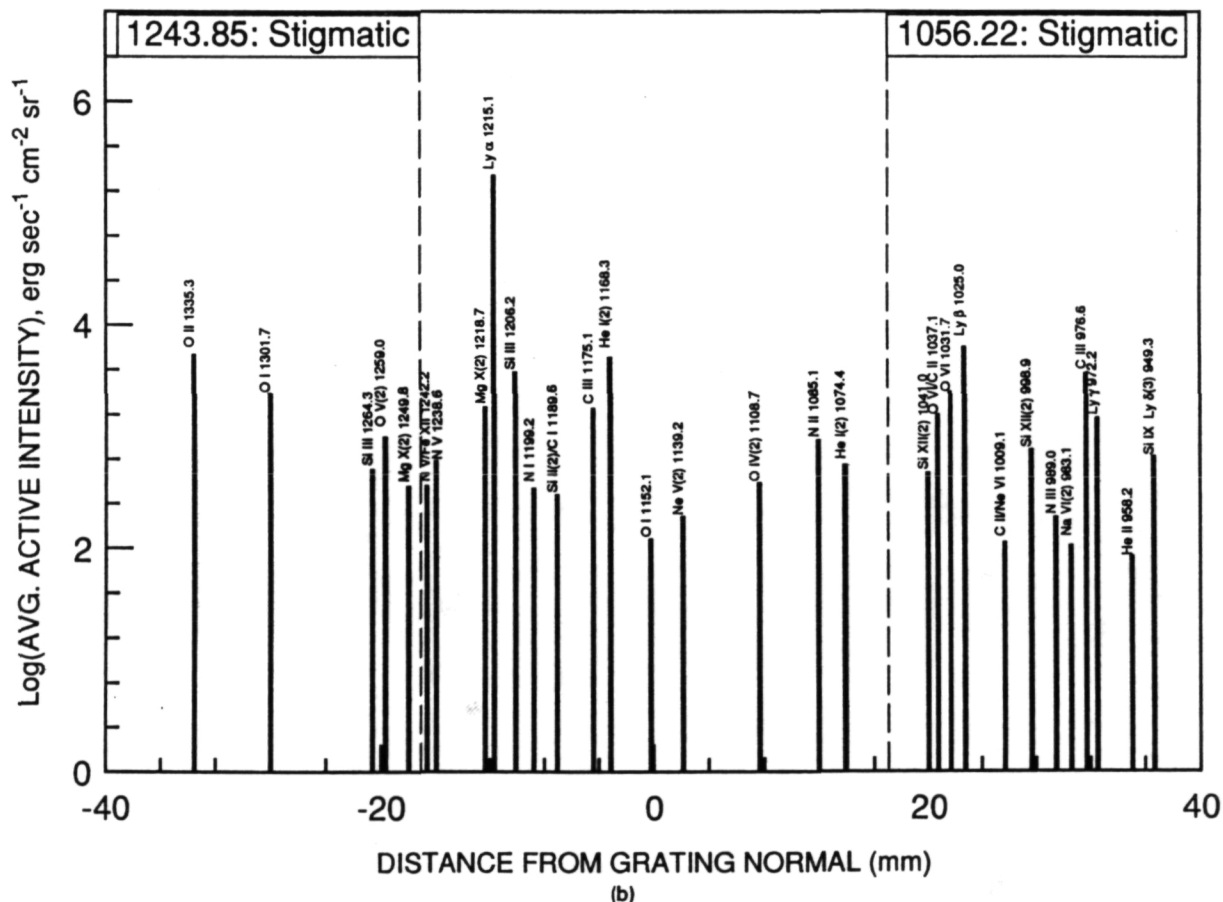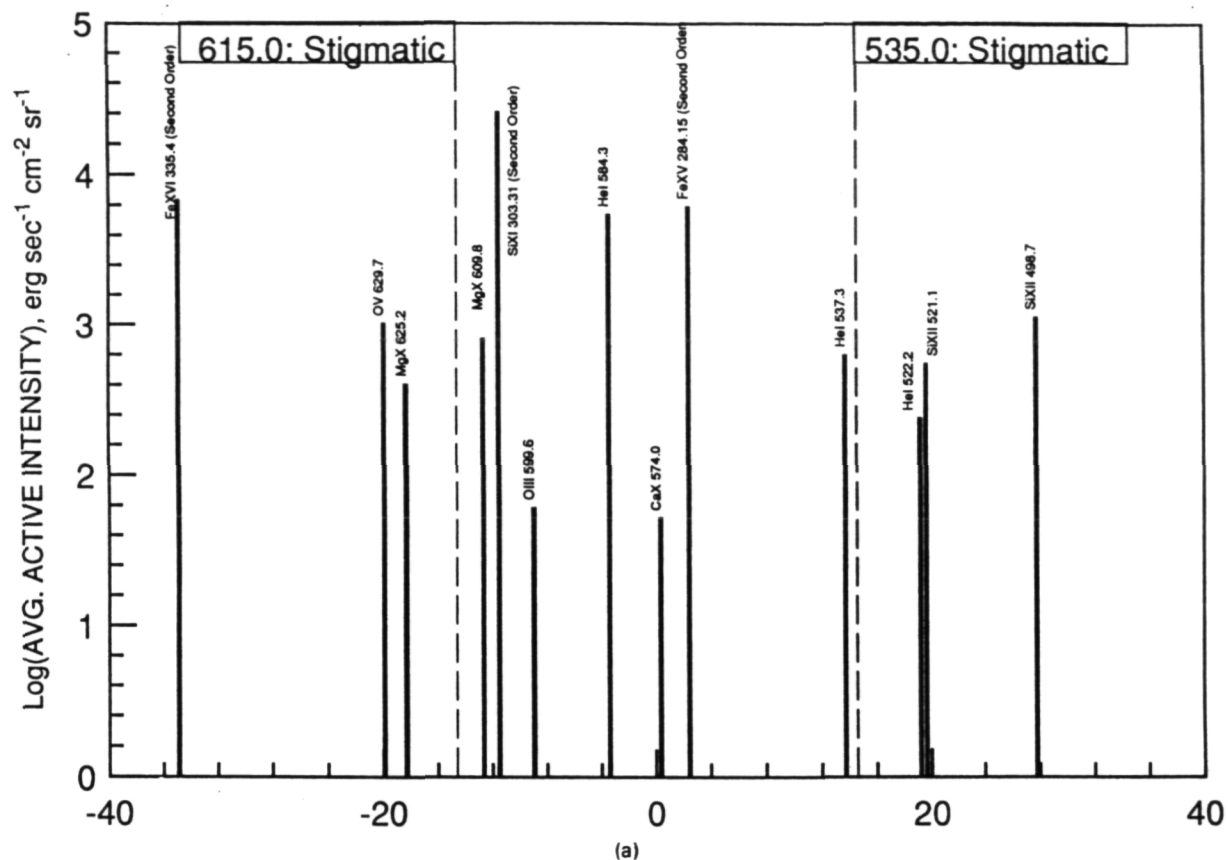
(a)

(b)

DISTANCE FROM GRATING NORMAL (mm)

Fig. 7. Locations of strong solar emission lines on the Rowland circle of the toroidal grating spectrometer. Angle of incidence = 11.947 deg, R_h = 1011.1 mm, and R_v = 989.1 mm. (a) grating ruling density 3600 grooves mm^{-1}; (b) grating ruling density 1800 grooves mm^{-1}.

16. D. B. Kasle, "High resolution decoding chips and single-chip decoders for multi-anode microchannel arrays," *SPIE Ultraviolet Technol.* III 1158, 311 (1989).
17. M. C. E. Huber, P. L. Smith, W. H. Parkinson, M. Kühne, and M. Kock, "Absolute extreme-ultraviolet solar spectral irradiance monitor (AESSIM)," *Adv. Space Res.* 8, 84 (1989).
18. A. B. C. Walker, Jr., J. F. Lindblom, R. B. Hoover, and T. W. Barbee, Jr., "Soft x-ray/XUV images of the solar corona with a normal incidence multilayer telescope," *Science* 241, 1781 (1988).
19. K. Danzmann, M. Günther, J. Fischer, M. Kock, and M. Kühne, "High current hollow cathode as a radiometric transfer standard source for the extreme vacuum ultraviolet," *Appl. Opt.* 27, 4947 (1988).
20. D. M. Hassler, G. J. Rottman, and F. Q. Orrall, "Absolute velocity measurements in the solar transition region and corona," *Adv. Space Res.* (1990).

J. Gethyn Timothy received the B.Sc. degree in physics at University College London, England, in 1964 with honors and the Ph.D. degree in Space Physics at the University in 1971. Since 1984 he has held the position of professor (research) of applied physics in the Center for Space Science and Astrophysics at Stanford University. Timothy is co-inventor of the MAMA detector system and is currently the principal investigator on five NASA contracts and grants in the fields of advanced astrophysics instrumentation development and solar and stellar space observations. He is author or coauthor of over 100 papers published in the scientific literature.

Thomas Edward Berger received his BS degree in engineering physics from the University of California at Berkeley in 1985. From 1985 to 1988 he was employed by Lockheed as a flight science analyst on the propulsion system of the ATF aircraft. In 1989 he received his MS degree in mechanical engineering from Stanford University, where he is currently working toward his Ph.D. degree. Berger's current research is in the design and implementation of EUV spectroscopic instruments for astrophysical and plasma research applications; he has been involved in the HiRES program since March 1990.

Jeffrey S. Morgan: Biography and photograph not available.

Arthur B.C. Walker, Jr.: Biography appears with the paper "Multi-Spectral Solar Telescope Array II: soft x-ray/EUV reflectivity of the multilayer mirrors" in this issue.

S. K. Jain obtained his doctorate degree in experimental cosmic ray physics from Punjab University, Chandigarh, India. His interests include instrumentation and observations in optical astronomy. His present work involves polarimetric studies of star-forming regions, young stellar systems, and post-AGB stars and protoplanetary nebulae. Currently, he is working on solar astronomy and the development of payload for high-resolution studies of the sun in the extreme ultraviolet region of the spectrum. Dr. Jain is a member of the Astronomical Society of India and the International Astronomical Union.

A. K. Saxena obtained his M.Sc. and Ph.D. degrees in physics from Lucknow University, India, in 1968 and 1977, respectively. His early research activities were mainly directed toward developing new polarization techniques for the study of refractive index fields. From 1974 to 1977 he worked on instrumentation for high-resolution spectroscopy observation of the sun and stars, and during the February 1980 total solar eclipse he performed a high-resolution spectroscopic study of the solar corona using multislit spectrography. He has developed a new polarization interferometer technique using a simple device (Babinet compensator) for the precise quantitative evaluation of optical surfaces. Dr. Saxena is presently the head of the Optics Division of the Indian Institute of Astrophysics. He is a member of SPIE, the International Astronomical Union, the Astronomical Society of India, and the Indian Vacuum Society, and is a fellow of the Optical Society of India. He was selected for inclusion in the first edition of Marquis's International Who's Who in Optical Science and Engineering.

J. C. Bhattacharyya obtained his M.Sc. in radio physics and electronics in 1951 and D.Phil. (Sci) in 1971 from Calcutta University, India. Before joining the Indian Institute of Astrophysics in 1964, he worked at the India Meteorological Department in the Instruments Division. At the Institute, he channeled his efforts into designing and building up instruments for the study of solar and solar system objects. He was the director of the Institute from 1982 through 1990. At present, he is continuing his instrumentation programs at the Institute as an Emeritus Scientist.

Martin C. E. Huber is head of the European Space Agency's (ESA) Space Science Department. He has been working in molecular and atomic spectroscopy, mainly in applications to astrophysics. He also is involved in providing instrumentation for solar EUV observations [OSO-6 and Skylab, launched 1969 and 1973, respectively, and the forthcoming Solar and Heliospheric Observatory (SOHO) mission.] Dr. Huber is also a professor at the Swiss Federal Institute of Technology Zürich (ETHZ) and is the treasurer of the newly founded European Astronomical Society (EAS).

Giuseppe Tondello is a professor of quantum electronics on the faculty of electronic engineering, University of Padova, Italy. He has worked on spectroscopy of laser-produced plasmas in the extreme ultraviolet and soft x-ray and on spectroscopic instrumentation both for laboratory and astrophysical application. Presently, he is coinvestigator of the Ultraviolet Coronograph Spectrometer of the SOHO mission and is involved in other solar and stellar space projects.

Giampiero Naletto works in collaboration with prof. G. Tondello at the University of Padova (Italy). Their principal research activity is based on the development of instrumentation for EUV-XUV optics. Naletto has participated in the configuration definition of various spectroscopic space instruments and, in particular, has studied the performances of toroidal and coma-corrected gratings as single element spectrometers. Another activity in which he is presently involved is the study of some new configurations for synchrotron radiation monochromators operating in the soft x-ray optical region.

Design and Test of a High-Resolution EUV Spectroheliometer

Thomas E. Berger, J. Gethyn Timothy, Arthur B. C. Walker Jr., Helen Kirby and Jeffrey S. Morgan

Center for Space Science and Astrophysics, Stanford University, ERL 314
Stanford, CA 94305-4055, USA

Surendra K. Jain, Ajay K. Saxena and Jagadish C. Bhattacharyya

Indian Institute of Astrophysics
Bangalore 560034, India

Martin C. E. Huber

Space Science Department, European Space Agency
ESTEC Postbus 299, NL-2200 AG Noordwijk, The Netherlands

and

Giuseppe Tondello and Giampiero Naletto

Istituto di Elettronica, Università di Padova
I-35100 Padova, Italy

ABSTRACT

The High-Resolution EUV Spectroheliometer (HiRES) is a sounding rocket instrument designed to obtain very high spatial, spectral and temporal resolution images of the solar outer atmosphere. The main components of the instrument are a 45-cm Gregorian telescope feeding a 1-m normal-incidence stigmatic EUV spectrometer with an imaging Multi-Anode Microchannel Array (MAMA) detector system together with a 1-m Wadsworth IR spectrometer with an imaging CCD detector system. The stigmatic EUV spectrometer utilizes a single toroidal diffraction grating which is fabricated by a recently developed method employing an elastically deformable substrate. An additional 0.25-m normal-incidence spectrometer with a MAMA detector system is included in order to record atmospheric extinction data over the 280 to 1270 Å wavelength range. This paper summarizes the expected performance of the telescope and 1-m EUV spectrometer system including the effects of vibrational misalignments and despaces due to the sounding rocket flight environment. Finite element analyses of the telescope primary mirror mounting concepts are presented and discussed. In addition, results of ray tracing and laboratory spectrograph measurements from the toroidal grating test program are presented and discussed.

1. INTRODUCTION

The conceptual design of the HiRES instrument as well as the primary scientific objectives were outlined in the previous year's proceedings.[1] In brief, the instrument is designed to observe the solar chromosphere, transition region, and corona with spatial resolution of 0.4 arcsec, spectral resolution ($\lambda/\Delta\lambda$) of at least 10^4, and temporal resolution on the order of seconds in the wavelength range from about 500 to 650 Å. These observations will allow dynamic studies of the fine scale structure of the solar outer

atmosphere within a temperature range from 3×10^4 to 2×10^6 K with a Doppler line-shift velocimetry sensitivity of approximately 1 km s^{-1} at 600 Å. A unique feature of the instrument is its ability to produce stigmatic images in the EUV wavelength range of interest through the use of a toroidal diffraction grating. The toroidal grating itself is produced by a recently developed method using a deformable substrate replication method as described by Huber, Tondello and others.[2,3,4,5] The use of an advanced Multi-Anode Microchannel Array (MAMA) detector will enable the images to be transmitted, recorded, and pro-
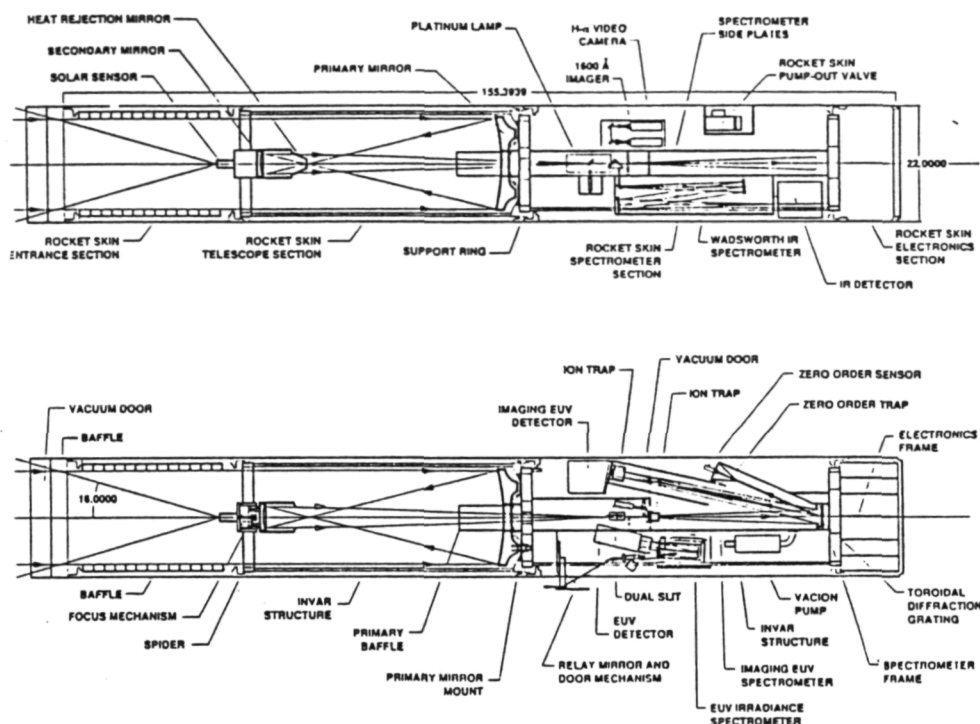
PRECEDING PAGE BLANK NOT FILMED

Fig. 1. Conceptual layout of the HiRES Payload.

cessed electronically, thus, greatly increasing the temporal resolution, inscene dynamic range, and photometric accuracy. The development of large-format, flight-qualified MAMA detectors has continued under the impetus of the SOHO, STIS and *Lyman*/FUSE flight programs.[6,7,8] In addition, a recent sounding rocket flight by Dr. Andrew Smith (NASA Goddard Space Flight Center) using a 256 x 1024-pixel MAMA detector successfully imaged the irregular galaxy NGC 4449 in the far ultraviolet, providing valuable experience with MAMA detectors in the sounding rocket environment.[9]

The HiRES instrument consists of a Gregorian telescope which is focussed onto a multi-purpose entrance slit complex. The entrance slit is etched in a reflective substrate in order to allow real time monitoring of the telescope targeting by a CCD camera and also to measure the temperature minimum irradiance at 1600 Å through a separate filtered camera. Two slits feed respectively a 1-m toroidal grating spectrometer for the stigmatic observations

Table 1. HiRES Classical Gregorian Specifications

Primary Mirror		Secondary Mirror		System	
Diameter	450 mm	Diameter	112 mm	Mirror Separation	1093 mm
F-Number	1.944	Magnification	-7.716	Focal Length	6750 mm
Radius of Curvature	1750 mm	Radius of Curvature	385.5822 mm	F-Number	15
Conic Constant	-1	Conic Constant	-0.593658	Back Focal Length	587 mm
Center Hole Diameter	75 mm	Obscuration	25%	Overall Length	1680 mm
Substrate Material	Zerodur[a]	Substrate Material	Zerodur	Plate Scale	33 μm (arcsec)$^{-1}$
Coating	Iridium	Coating	Iridium	Total Field of View	3x3 arcmin[b]
				Metering Structure	Invar

[a] Density 2.52 gm cm^{-3}: Primary mirror weight = 29.4 kg
[b] Limited by Lyot stop at primary focus

Table 2. HiRES EUV Spectrometer Characteristics			
1-M TOROIDAL GRATING SPECTROMETER		**0.25-M EUV IRRADIANCE SPECTROMETER**	
Mounting	Rowland Circle	Mounting	Rowland Circle
Entrance Slit	14 μm x 6.2 mm	Grating Type	Spherical
Field of View	0.4 arcsec. x 3.0 arcmin.	Entrance Slit	10 μm x 3.0 mm
Grating Ruling Frequency	3600 lines/mm	Field of View	3.8° x 3.8°
Grating Mean Radius of Curvature	1000 mm	Grating Ruling Frequency	1028 lines/mm
Angle of Incidence	11.947°	Grating Radius of Curvature	250 mm
Aspect Ratio of Toroid	0.9782	Angle of Incidence	9.0°
Horizontal Radius of Curvature	1011.1 mm	Wavelength Range	280 Å to 1270 Å[a]
Vertical Radius of Curvature	989.1 mm	Spectral Resolution (2 pixels)	2 Å
Stigmatic Wavelength Range	510 Å to 630 Å[a]	Substrate Material	Zerodur
Spectral Resolution (2 pixels)	0.078 Å	Coating	Gold
Substrate Material	Zerodur		
Coating	Osmium		

[a] Wavelength ranges in 1st order

in the EUV and a 1-m Wadsworth spectrometer for detailed line shape studies of the He I 10830 Å absorption feature. The toroidal grating spectrometer employs a (728 x 2808)-pixel MAMA detector; the Wadsworth spectrometer will use a CCD detector. In addition, the payload includes an ISTC (formerly Westinghouse) platinum hollow-cathode lamp[10] for on-board calibration of the EUV spectrometer, as well as a separate 0.25-m spherical grating spectrometer with a (1 x 1024)-pixel MAMA detector for atmospheric extinction measurements in the 280 to 1270 Å range. A conceptual layout of the payload is shown in Fig. 1. The telescope specifications are given in Table 1, the characteristics of the spectrometers are summarized in Table 2 and the MAMA detector characteristics are summarized in Table 3.

This paper reviews the results of ray-tracing analyses of the telescope and the telescope/toroidal grating combination. This is followed by a discussion of the tilt and despace tolerances on the optical system which must be maintained in order to achieve and maintain the 0.4 arcsec resolution in the sounding rocket environment. Results from finite element analyses of the telescope primary mirror are presented and used to introduce a proposed primary mirror mounting method. Test results from the laboratory toroidal grating work are also presented and compared with ray-tracing predictions of the imaging performance.

2. EUV ALIGNED SYSTEM ANALYSIS

In order to ascertain the image quality of the telescope and the complete telescope-toroidal grating combination, ray tracing studies were carried out using the *CODE V* computer program from Optical Research Associates, Pasadena, California. These studies investigated image aberrations in a system assumed to have perfectly figured

Table 3. HiRES MAMA Detector Characteristics	
TOROIDAL GRATING SPECTROMETER DETECTOR	
Type	Open Structure
Format	728 x 2808 pixels (fine-fine)
Total No of Amplifiers	160
Pixel Dimensions	14 x 14 μm
Position Sensitivity	< 1 μm
Photocathode Material	MgF_2 or KBr
IRRADIANCE SPECTROMETER DETECTOR	
Type	Open Structure
Format	1 x 1024 pixels (fine-fine)
Total number of Amplifiers	64
Pixel Dimensions	25 x 25 μm
Photocathode Material	bare MCP

elements and did not take into account effects due to scattering, intermediate slope errors, figure errors, or reflectivity characteristics of the coatings. The effects of misalignment are discussed in the following section.

The telescope type selected for the HiRES mission is a classical Gregorian. The Gregorian type is chosen because it allows a stop to be placed at the primary focal point which limits the field-of-view and can be mirrored in order to shield the secondary mirror and its associated structure from out-of-field radiation. The rejection of heat from the secondary mirror is necessary in order to avoid excessive thermal expansion of the structure and also to reduce the effects of UV photopolymerization of contaminants on the mirror surface. The basic characteristics of the telescope are summarized in Table 1. Normally, the field limiting aberration of the classical Gregorian is tangential coma.
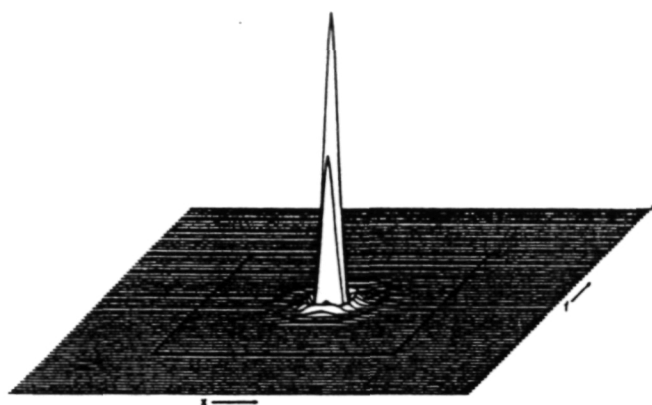
Fig. 2. Telescope on-axis Point Spread Function (PSF). The solid square drawn around the PSF is 14 µm in size which corresponds to a single detector pixel.

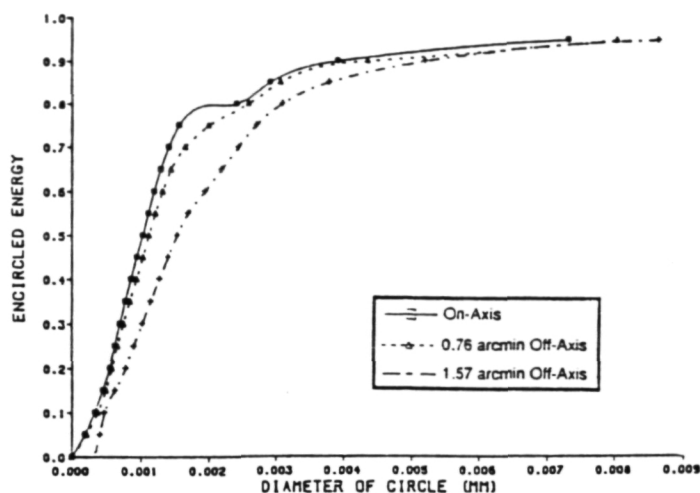
Fig. 4. Telescope Encircled Energy plot. The 80% encirclement values for the three field angles shown are 2.4 µm (0.073 arcsec), 2.59 µm (0.079 arcsec, and 3.1 µm (0.094 arsec), respectively.

Fig. 3. Telescope Spot Diagrams for three field angles: On-Axis (*bottom*), 0.76 arcmin (0.0127 deg.) field angle (*middle*), and 1.57 arcmin (0.0260 deg.) field angle (*top*). The scale bar represents 5 µm.

This can be eliminated by employing an aplanatic design with an ellipsoidal primary mirror. However, due to the limited field of view, coma from the telescope (and all other off-axis aberrations as well) will be small and will not limit the resolution of the instrument. A fortunate benefit of using a classical Gregorian rather than an aplanat is that the paraboidal primary of the classical type is relatively easy to grind, polish and test.

Fig. 2 shows the on-axis point spread function (PSF) at the spectrometer entrance slit (telescope focal plane). For comparison, a 14 x 14 µm^2 square, representing a single detector pixel is drawn around the PSF. Fig. 3 shows the spot diagrams for three positions along the spectrometer entrance slit. From bottom to top, the field positions are on-axis (0 arcmin field angle), ± 1.5 mm along the slit (0.76 arcmin field angle), and ± 3.1mm along the slit (1.57 arcmin field angle), respectively. Fig. 4 presents the encircled energy curve for the same field angles as shown in the spot diagrams in Fig. 3. This figure reveals that for the on-axis image, 80 percent of the energy is contained within a 2.4 µm (0.073 arcsec) circle and for the maximum field-angle image points at 1.57 arcmin, 80 percent of the energy is within a 3.1 µm (0.10 arcsec) circle. Thus, the f/15 classical Gregorian is capable of achieving a 0.1 arcsec resolution over the entire field of interest. The telescope performance is not diffraction-limited since for an obscuration of 25%, the first Airy diameter of a perfect aperture image is
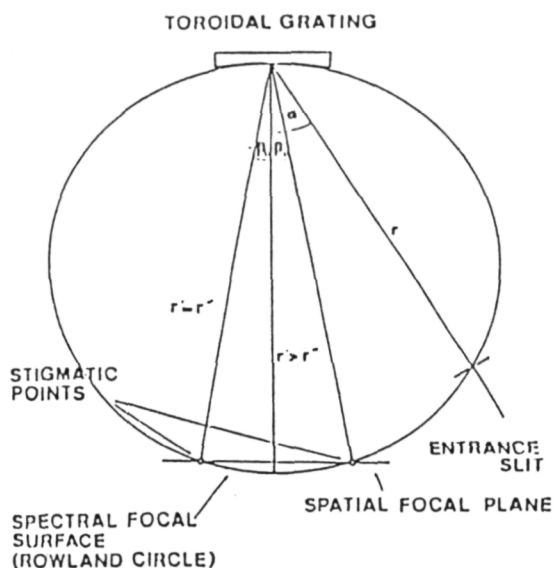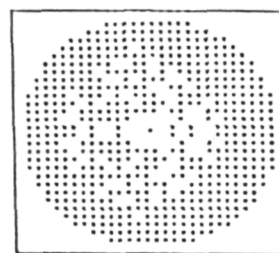
TOROIDAL GRATING

STIGMATIC
POINTS

ENTRANCE
SLIT

SPATIAL FOCAL PLANE

SPECTRAL FOCAL
SURFACE
(ROWLAND CIRCLE)

Close. Gregorian Telescope

25.00 mm

Toroidal Grating Footprint

Fig. 5. Layout of spectrograph employing a single toroidal grating. Exact stigmatic focusing occurs at angles of diffraction $\pm \beta_0$ which are defined by Eqn. (1). For small values of β_0 and a sufficient depth of focus, the images are effectively stigmatic between and somewhat beyond the two stigmatic points.

approximately 1 μm. However, the spot size is well within the resolution requirements of the instrument.

From the spectrometer entrance slit, the telescope image diverges to the diffraction grating. The grating both diffracts and reimages the slit with the tangential (also called the *spatial* , *vertical*, or *secondary*) focus occuring on a parabolic curve in the equatorial plane of the grating and the sagittal (also called the *spectral* or *horizontal*) focus occuring on the Rowland circle.[11] For a spherical diffraction grating, the focus curves do not intersect and all images are astigmatic; for a toroidal grating, the vertical radius of curvature, R_v, is decreased relative to the horizontal radius, R_h, and the curves then intersect at two points located symmetrically about the grating normal as shown in Fig. 5. For a given angle of incidence, α, the relation between the radii of curvature and the stigmatic points located at angles $\pm \beta_0$ is given by

$$R_v = R_h \cos\alpha \cos\beta_0 \qquad (1)$$

For the HiRES toroidal grating, the stigmatic points are located at $\beta_0 = \pm 0.8250°$ from the grating normal corresponding to 615 and 535 Å. Imaging the stigmatic points

Fig. 6. Ray footprint of the telescope image on the toroidal grating. The grating extent of 70 x 70 mm^2 is shown by the solid rectangle. The clipping is due to the input ray grid. The obscuration of the telescope secondary mirror is evident in the missing rays in the central portion of the footprint. The scale bar represents 25 mm.

this close to the normal has two advantages. First, the parabolic secondary focal curve is very shallow near the normal and is approximated by a straight line within the resolution tolerance of the system thus allowing a planar detector face to be used without degradation in image quality. Second, the distance between the secondary curve and the Rowland circle is small so that the residual astigmatism between and somewhat beyond the stigmatic points is within the aberrational tolerance of the system.

A *CODE V* ray tracing model of the telescope/toroidal grating combination was constructed in order to investigate the image quality of the complete optical system. Fig. 6 shows the ray footprint from the telescope on the toroidal grating . The footprint is limited to approximately the central 61 mm of the 70 mm grating showing that the grating is slightly underfilled in the present system. In Fig. 7, spot diagrams are shown for the 535 Å stigmatic point for the same three field angles examined in Fig. 3. The results for the 615 Å stigmatic point are essentially identical to the 535 Å results. Fig. 7 reveals that the meridional plane image quality of the telescope-toroidal grating system is excellent with an RMS spot size of approximately 0.1 arc-sec; the image is characterized by a circular core with resid-
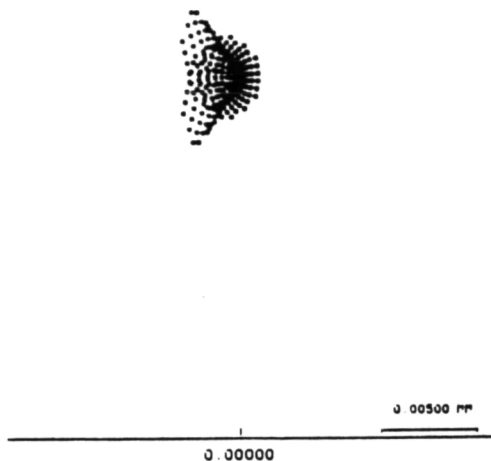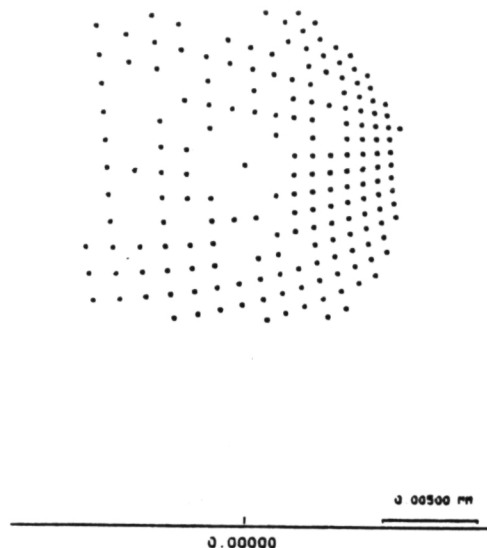
Figure 7a.

Figure 7c.

```
0 00500 mm
0.00000
```

Fig. 7a. Spot diagram for the 535 Å stigmatic point in the meridional plane. The scale bar represents 5 µm. Residual comatic aberration is evident on an otherwise circular image

Fig. 7b. Spot diagram for the 535 Å stigmatic point 0.76 armin. off the meridional plane. The scale bar represents 5 µm. The image reveals obscuration effects from the telescope secondary mirror as well as the increased coma.

Fig. 7c. Spot diagram for the 535 Å stigmatic point 1.57 arcmin off the meridional plane. The scale bar represents 10 µm. The image is basically identical to the image in Fig. 7b except for a large-scale factor increase.

Figure 7b.

ual comatic flare. However, the off-plane image quality is further degraded by coma and the resulting RMS spot size is increased. In particular, the RMS spot size for the 0.76 arcmin field angle is 0.51 arcsec and the RMS spot size for the 1.57 arcmin field angle is 1.04 arcsec. It is also evident that the obscuration of the secondary mirror results in a central void for the off-plane field angles. Fig. 8 presents the same spot diagrams at the secondary focal curve for the 575 Å radiation which is imaged on the grating normal. It can be seen that the meridional image quality is still excel-
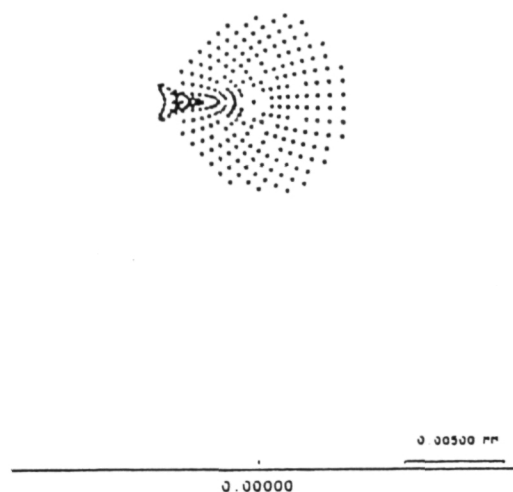
Fig. 8a. Spot Diagram for the 575 Å image on the grating normal. The scale bar represents 5 μm. The main image core is the circle of least confusion for this astigmatic point. The spot size is still well within the 14 micron pixel size and shows decreased comatic aberration relative to the stigmatic points due to imaging on the grating normal.
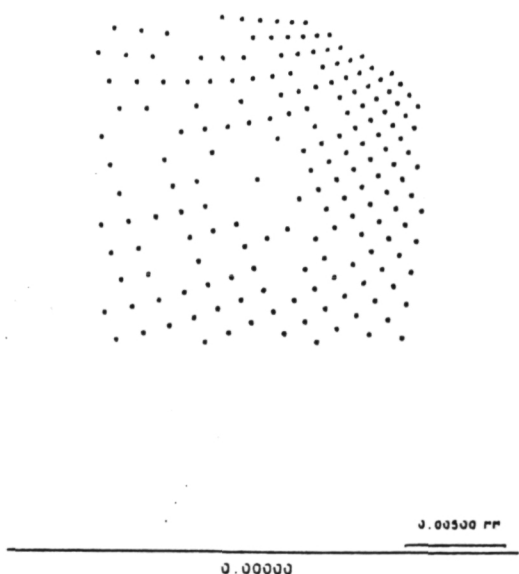
Fig. 8c. Spot diagram for the 575 Å image 1.57 arcmin off the meridional plane. The scale bar represents 10 μm. This image is very similar to the image in Fig. 7c and again demonstrates the uniformity of off-plane imaging.

lent with a nearly symmetric core and small residual coma; the RMS spot size is 0.186 arcsec. Off-plane image quality is nearly identical to that of the stigmatic points with a 0.51 arcsec RMS spot size at 0.76 arcmin and a 0.9874 arcsec spot size at 1.57 arcmin. Fig. 9 plots the encircled energy on the detector plane at 575 Å for the three field angles

Fig. 8b. Spot diagram for the 575 Å image 0.76 arcmin off the meridional plane. The scale bar represents 5 μm. This image is nearly identical to the image in Fig. 7b showing that the off-plane image quality is very uniform.
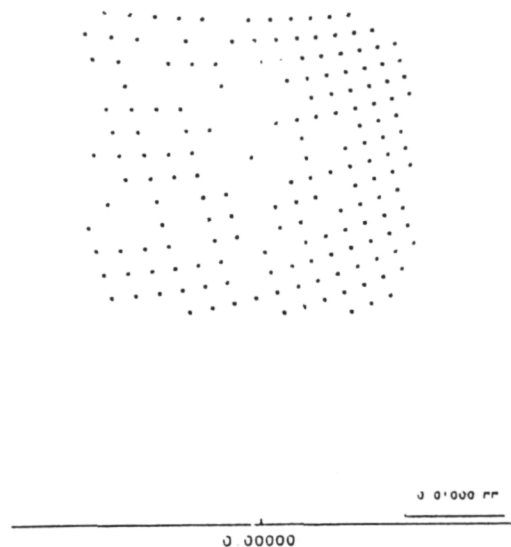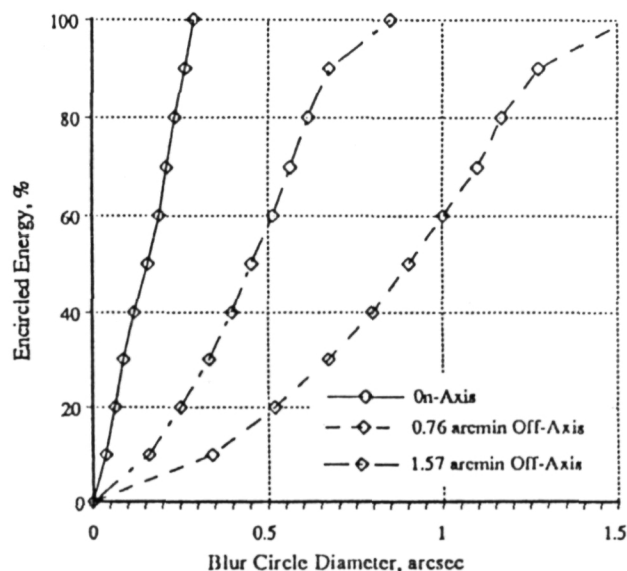
Fig. 9. Geometric Encircled energy on the detector plane. The on-axis (in the meridional plane) image demonstrates 0.3 arcsec resolution. 60% of 0.76 arcmin field angle energy is contained within 0.5 arcsec, while 20% of the 1.57 arcmin field angle energy is contained within 0.5 arcsec.
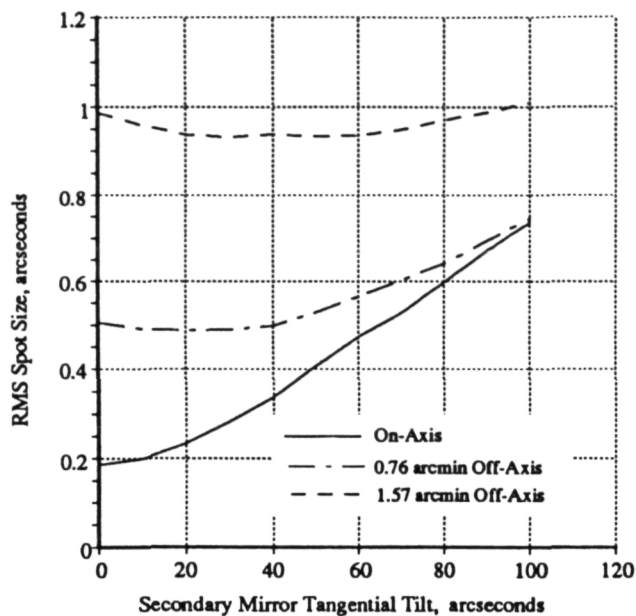
Fig. 10. RMS spot size vs. secondary mirror tilt. The three field angles discussed in the text are plotted: (——) on-axis; (— - —) 0.76 arcmin off-axis; (— — —) 1.57 arcmin off-axis.

plotted in Figs. 7 and 8. It is evident that the pure-toroidal grating does not provide the desired image characteristics for the off-plane points. The performance of coma-corrected toroidal gratings is currently under investigation[2] and is discussed in section 5.

3. EFFECTS OF ALIGNMENT AND DESPACE ERRORS

The results given above assume a perfectly aligned optical system. Since the payload is to be initially flown on a sounding rocket, it is anticipated that static and dynamic loads of flight will result in some degree of misalignment and despace among the components. In Fig. 10, RMS spot size of the image on the detector plane for the 575 Å (grating normal) radiation is plotted against secondary mirror tilt in the tangential plane. The 575 Å wavelength is studied because as shown in the preceding section it suffers the greatest in-plane aberration for wavelengths between the stigmatic points and therefore will be the most sensitive to alignment errors. From Fig. 10, it can be seen that a secondary tilt of approximately 50 arcsec results in a blur size of 0.4 arcsec for the on-axis rays and in order to maintain a blur size of 0.5 arcsec or below for these rays, the maximum allowable tilt is 65 arcsec. The effect of tangential secondary tilt on the off-axis images is seen to

Fig. 11. Spot diagram for 50 arsec of tangential tilt on the secondary mirror. The bottom spot corresponds to the on-axis field point, the middle spot to the 0.76 arcmin field angle, and the top spot to the 1.57 arcmin field angle. The scale bar represents 28 μm (2 pixels).
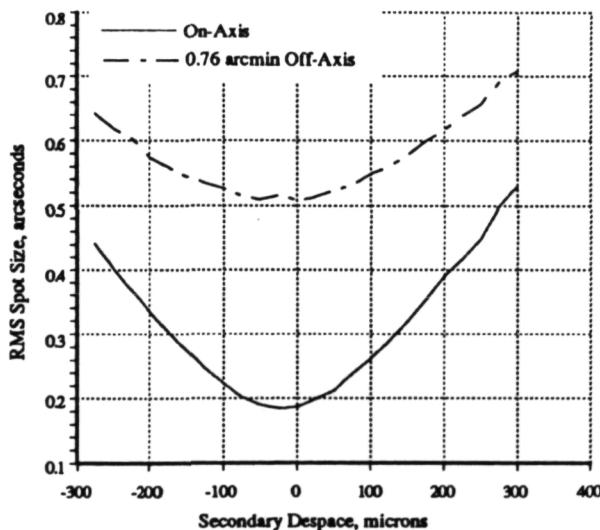

Fig. 12. RMS spot size vs. secondary mirror despace. Negative values of despace correspond to movement of the secondary away from the primary mirror. The optimum detector plane focus occurs for a secondary mirror position which is negatively despaced from the primary approximately 25 mm. This is due to a reduction in effective field angle at the diffraction grating with a resulting reduction in coma.

increase resolution within a certain angular range. This is due to the decrease in effective field angle at the diffraction grating for the off-axis points. The 0.76 arcmin field angle rays give an approximately constant spot size over a 40 arc-sec range. For the 1.57 arcmin field angle (± 3.1 mm off-center in the slit), Fig. 9 verifies that the spot size does not increase with tilts less than 100 arcsec. The spot diagram for 50 arcsec of tangential secondary mirror tilt is shown in Fig. 11. From this diagram and the preceding analysis it is evident that no more than 40 arcsec of tilt can tolerated in the tangential direction. Sagittal tilt tolerance is somewhat less restricted since the only requirement is that the tele-scope focal spot fit within the spectrometer entrance slit. For instance, a sagittal tilt of 1.57 arcmin would center the top spot shown in Fig. 3 onto the entrance slit (although this diagram shows tangential extent, the telescope is rota-tionally symmetric); since the RMS spot size of this image is 1.84 μm, it is well within the slit boundaries.

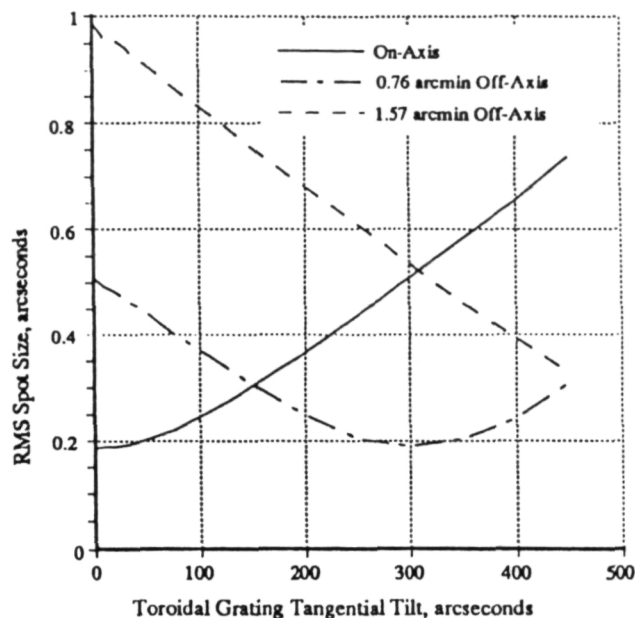The effects of secondary mirror despace errors are sum-

Fig. 14. RMS spot size vs. grating tangential tilt for the image points on and above the meridional plane. The off-plane image size is reduced significantly from that of the untilted grating. However, loss of symmetry results in degradation of the images points below the meridional plane.

marized in Fig. 12 for the on-axis and 0.76 arcmin off-axis images at 575 Å. The asymmetry in the curves toward neg-ative despace (secondary moved *away* from primary) is evidence of the fact that by increasing the length of the sec-ondary-grating distance, effective field angle at the grating is decreased and a concominant decrease in comatic aberra-tion leads to an improved spatial focus at the detector plane. This has the effect of degrading the telescope image on the slit jaw which is used for active monitoring of the pointing of the instrument, but the depth of focus of the telescope will be sufficient to allow this degradation and still maintain a high contrast slit-jaw image. Further inves-tigation in system optimization is currently being carried out. In order to maintain less than 0.5 arcsec resolution for the on axis image, Fig. 12 shows that a despace tolerance of ± 300 μm is required on the secondary mirror. This same tolerance will hold the off-axis image to within 0.7 arcsec resolution. Fig. 13 shows a spot diagram for the two field angles discussed above at a despace of -275 μm. It is evi-dent that the dominant despace aberration is astigmatism with both fields progressing toward vertical line images. Because despace errors due to the combined effects of ther-mal expansion and vibration are anticipated to be on the order of several hundred μm, the analysis above shows that active focussing of the secondary mirror in the axial direc-tion is beneficial to obtaining the resolution goals of the

Fig. 13. Spot Diagrams on the detector plane for -275 micron secondary mirror despace. The on-axis image (*bottom*) exhibits the onset of astigmatism and the resultant vertical line image shape. The 0.76 arcmin off-axis image (*middle*) and the 1.57 arcmin off-axis image (*top*) exhibit rotated astigmatic line shapes. The scale bar represents 28 μm (2 pixels).
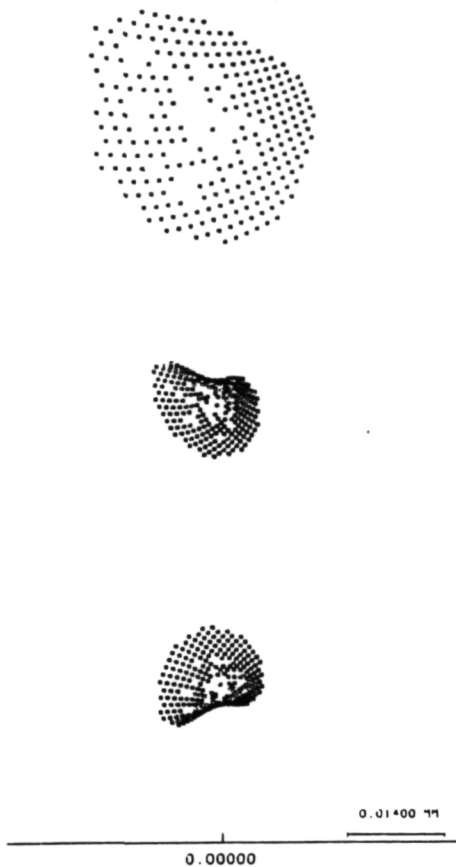
Fig. 15. Spot diagrams on and above the meridional plane for 150 arcsec of tangential grating tilt. Field angles of 0 arcsec (*bottom*), 0.76 arcmin (*middle*), and 1.57 arcmin (*top*) are shown. The scale bar represents 14 μm (1 pixel).

Fig. 16. Spot diagrams on and below the meridional plane for 150 arcsec of tangential grating tilt. Field angles of 0 arcsec (*bottom*), -0.76 arcsec (*middle*), and -1.57 arcsec (*top*) are shown. The scale bar represents 14 μm (1 pixel).

instrument.

Sensitivity of the image quality to grating tilt in the tangential plane is summarized in Fig. 14 at a wavelength of 575 Å. The on-axis image degrades in the same manner shown in Fig. 10, but exhibits a greatly reduced sensitivity to tilt of the grating relative to tilt of the telescope secondary mirror. The off-axis image quality is again improved due to decreased effective field angle however the effect is greatly enhanced over that of tilt in the secondary. For an RMS spot size below 0.5 arcsec for the on-axis image, the maximum allowable grating tangential grating tilt is approximately 300 arcsec. Fig. 15 shows the spot diagram for a grating tangential tilt of 150 arcsec which gives approximately equal RMS spot sizes of 0.304 arcsec at both the on-axis and 0.76 arcmin field angle. The scale bar represents 14 μm, or one pixel width. The 1.57 arcmin field angle RMS spot size for this condition is 0.753 arcsec in diameter which reveals that by compromising the on-axis
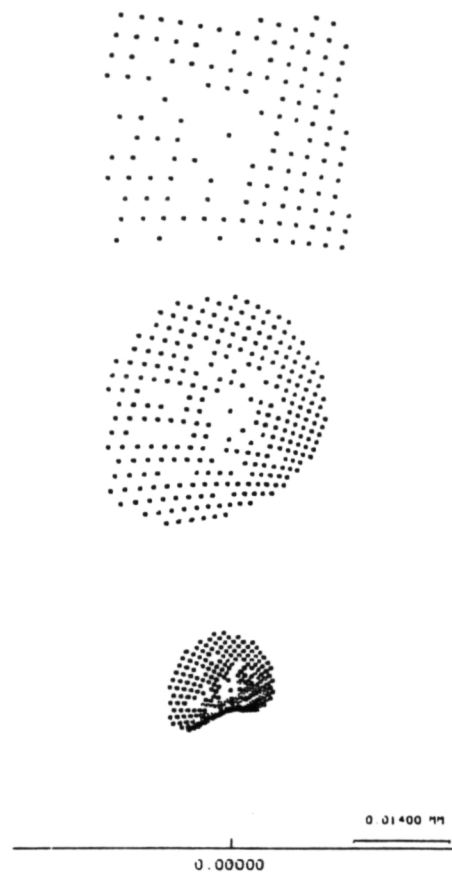
Table 4. HiRES Optical Element Alignment Tolerances	
Secondary Tilt	40 arcsec
Secondary Axial Despace	300 μm
Diffraction Grating Tilt	300 arcsec

image quality by rotating the grating in the tangential plane, a more uniform spatial response can be obtained from the system above the meridional plane. The resultant loss of tangential symmetry does however degrade the image below the meridional plane as shown in Fig. 16.

Table 4 summarizes the tolerances discussed in the preceding paragraphs. Although investigation of primary mirror and combined misalignments are not included, these
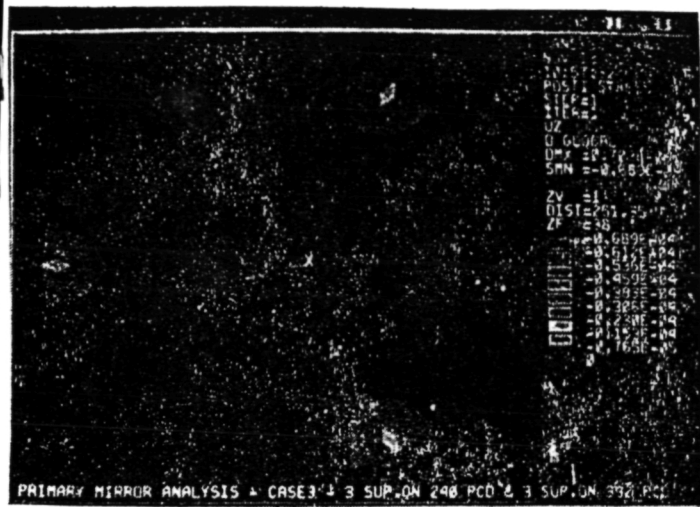
Fig. 17a. Deflection plot for a six-point mirror support system under 1-g static load. The maximum deflection of 0.07 μm occurs at the edges corresponding to the inner support pins.

Fig. 17b. Deflection plot for a 20 mm wide annular mirror support system under 1-g static load. The maximum deflection of 0.007 μm occurs uniformly around the outer edge of the mirror.

tolerances should be sufficient to maintain image quality in these cases as well. These tolerances are not excessive by modern machining and optical mounting standards and we therefore conclude that the HiRES instrument should be capable of 0.4 arcsec imaging in the sounding rocket environment given sufficient protection against vibration and thermal expansions. The following section discusses the optical mounting method which we intend to employ in order to provide this protection.

4. OPTICAL MOUNTING DESIGN

The launching static acceleration of a Terrier boosted Black Brant sounding rocket is 12.7 g while the overall RMS vibrational acceleration levels can reach 20 g. Given the tolerances derived in the preceding section, these conditions require a very well engineered mounting system for the optical elements of the instrument. The mountings must also limit motions due to thermal expansions of the payload structure and optical elements. Of particular concern is the primary mirror due to its large mass (29.4 kg) which is mainly a result of its uniform thickness construction. Although initial plans called for deep profiling of the rear substrate contour in order reduce the mass ("lightweighting" the mirror), this was later shown to be a possible source of excessive bending flex, especially at the thinner edges of the mirror. Consequently, the current design is a monolithic Zerodur substrate which has excellent thermal and bending stress resistance.

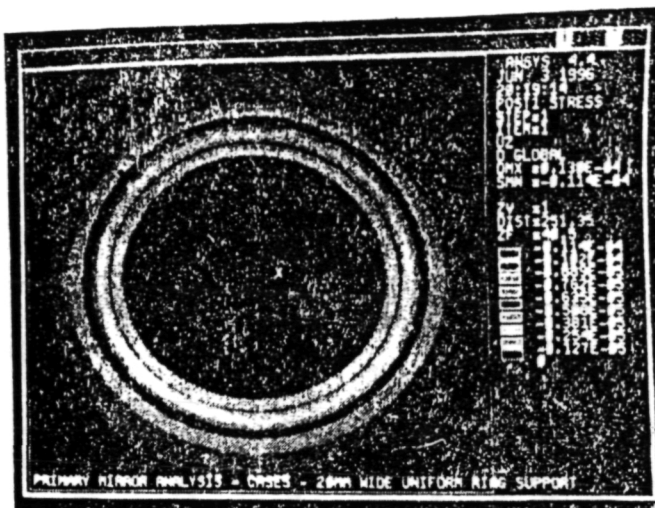A finite element model of the primary mirror is currently undergoing testing in India using the *ANSYS* program

in order to analyze possible mounting designs for the primary mirror. In Fig. 17 we show the results of static 1 g loading of two basic mounting designs: a six-point pin mount consisting of three inner and three outer diameter pins, and a uniform 20 mm wide support ring mount . As expected, the six point mount exhibits non-uniform deflections which are greatest at the edges of the mirror corresponding to the inner pins. The maximum deflection of this configuration is 0.07 μm. The annular ring mount shows a uniform deflection pattern with significantly decreased distortion over the entire mirror. The maximum deflection measured for this mount is 0.007 μm. Further analysis of this mounting method reveals that as the support ring is widened, overall deflection of the mirror is reduced. In all cases, maximum deflection occurrs at the edges of the mirror and this suggests that an annular, outer diameter support method may provide the smallest overall static deflection values.

Vibrational damping of the primary mirror and all other optical elements will be accomplished through the use of Dow Corning 93-500 Space Grade Encapsulant (Sylgard). This silicon-based encapsulant has extremely low vacuum outgassing rates, a low thermal conductivity of 8.36 x10^-5 Joules cm^-1 (deg C)^-1 sec^-1, and a Shore A hardness of 46. The edges of the optical elements will be completely potted in Sylgard, which is contained by an aluminum cell. The containment cells for the primary and secondary mirrors are then connected to the metering structure, aligned, and then rigidly fastened providing a robust base structure for the optical elements. This method of mirror mounting was used with success on the HRTS solar sounding rocket
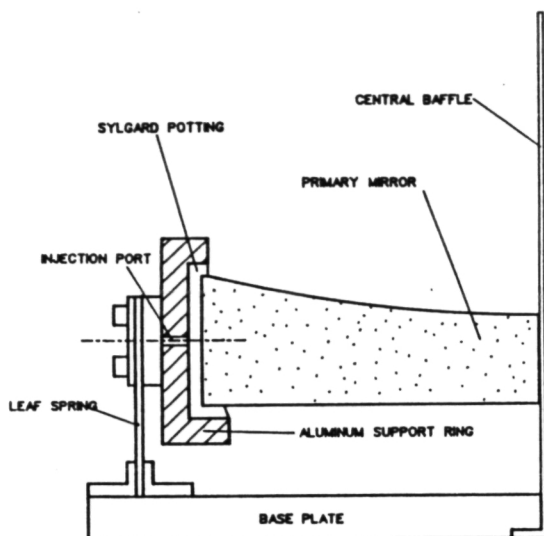
Fig. 18. Preliminary primary mirror support design. The Sylgard encapsulant provides both thermal and vibrational isolation of the mirror from the surrounding structure.

instrument.[12] Fig. 18 presents the proposed primary mirror design which incorporates the outer-diameter support method with the Sylgard potting-cell mounting method.

5. TOROIDAL GRATING TEST RESULTS

Laboratory testing of both toroidal and coma corrected toroidal gratings is currently underway at the University of Padua and Stanford. The toroidal gratings are tested under hollow cathode lamp illumination using the spectrometer shown in Fig. 19. A set of ten pinholes 25 μm in diameter and 250 μm apart is placed along the spectrometer entrance slit for image testing. The image is recorded on either an intensified CCD detector following a down-converting tetraphenyl butadine phosphor deposited on a fiber-optic faceplate or by an open-structure 360 x 1024-pixel MAMA detector directly attached to the spectrometer vacuum chamber.

Images of ten pinholes recorded at the He I 584 Å wavelength by the intensified CCD detector are shown in Fig. 20 for gas pressures in the light source of 5 and 30 mbar, respectively. For this particular grating, it is found
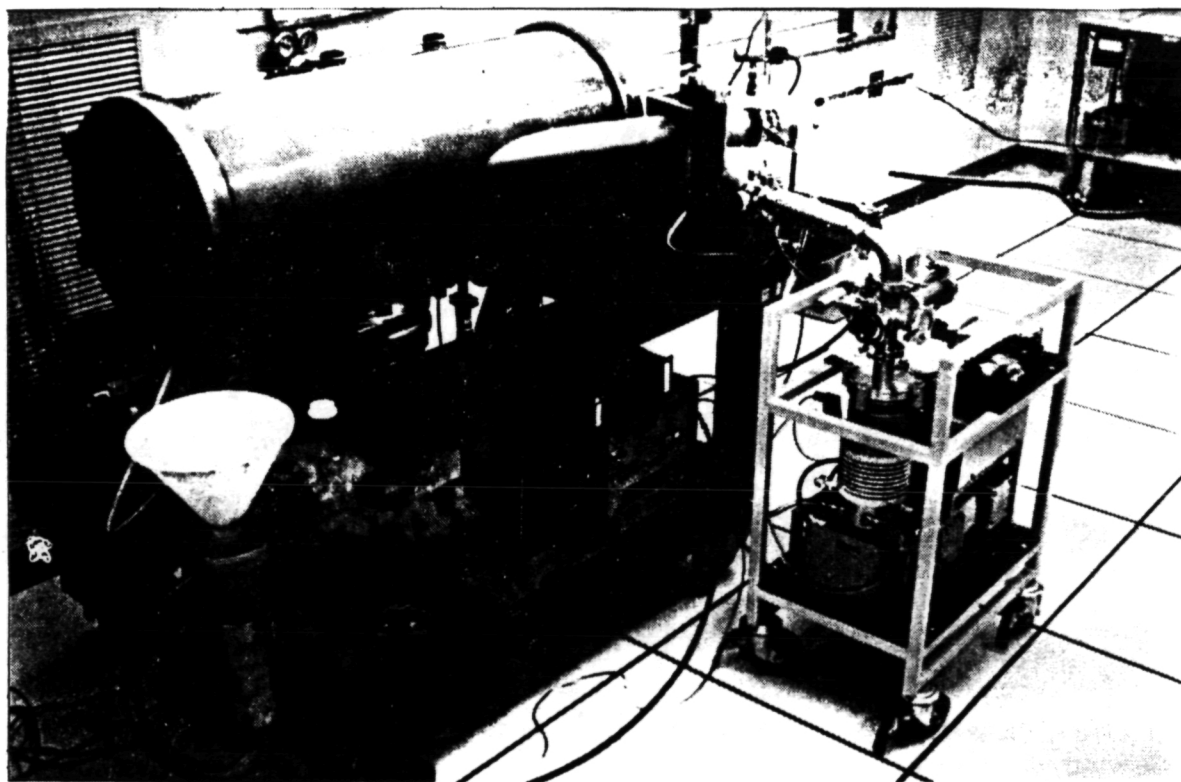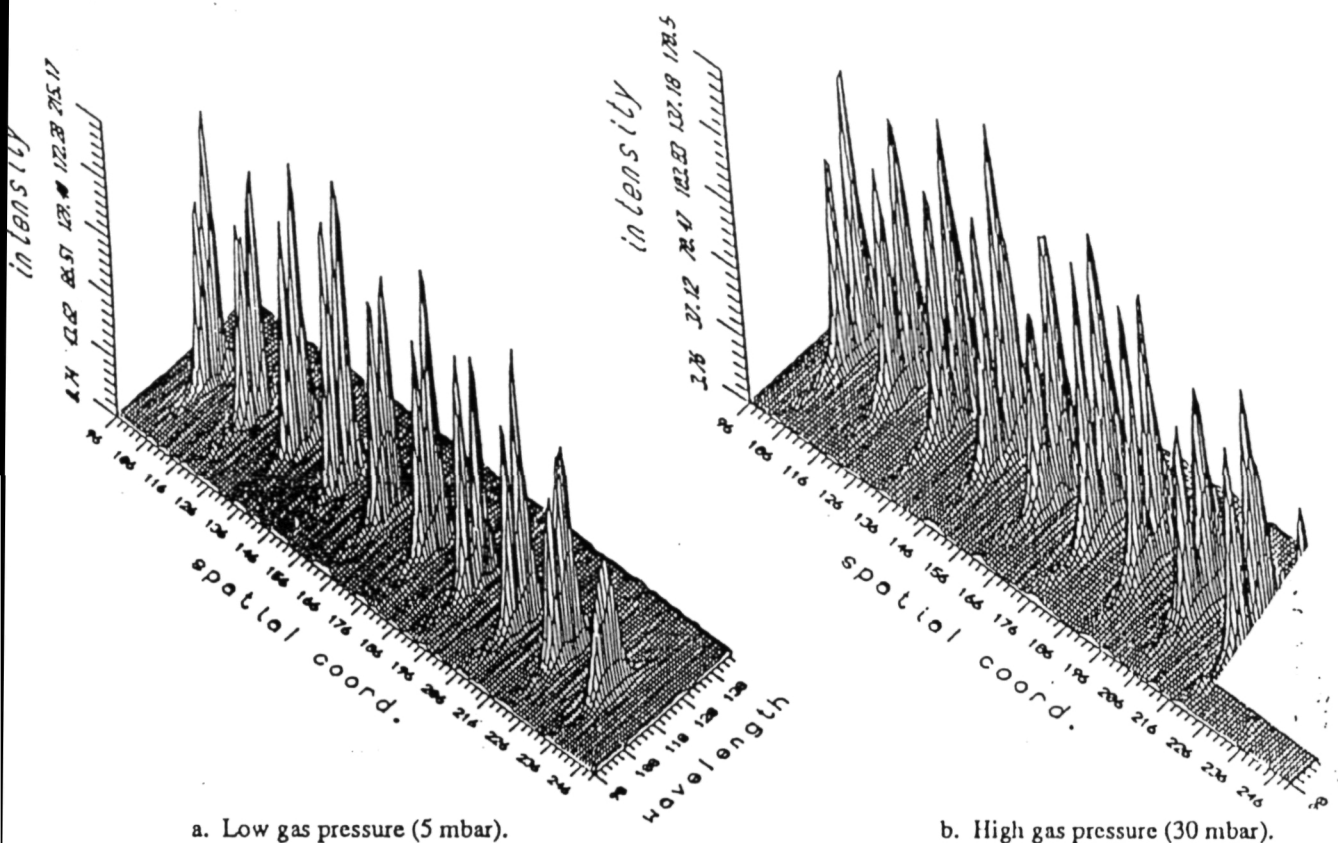

Fig. 19. The 1-m vacuum spectrograph at Stanford. The additional vacuum system in the cart on the right is used to differentially pump the hollow cathode lamp attached to the arm of the spectrograph. A similar version is in use at the University of Padua, Italy.

a. Low gas pressure (5 mbar).   b. High gas pressure (30 mbar).

Fig. 20. Images of ten 25 μm diameter pinholes in the He I 584 Å resonance line. The point spread function of the detector and the effects of finite size pinholes have been deconvolved from the image.

that the stigmatic condition is satisfied for an angle of incidence of 11.62° and $\beta_0 = 0.51°$ at 584 Å yielding an aspect ratio of $R_v/R_h = 0.9795$ very close to the desired value of 0.9782. With the measured instrument function deconvolved from the image, the spectral images of a singel pinhole at 5 and 30 mbar gas pressure appear as shown in Fig. 21. These images demonstrate the ability of the toroidal grating to provide high resolution simultaneously in the spatial and spectral dimensions. The residual coma evident in these images is much smaller than predicted by the ray tracing data shown in section 2. This is because the data shown here are for the toroidal grating alone and do include the effects of telescope image quality or off-axis pointing. Earlier ray tracing studies carried out on the grating alone[5] are in good agreement with these test results.

Testing of an N f/8 toroidal diffraction grating is now taking place at the University of Padua. The initial results have been reported elsewhere[2] and will shortly be compared with those from a coma-corrected f/8 toroidal grating. Future plans for grating testing include the further characterization of the f/15 toroidal grating in conjunction with the 360 x1024-pixel MAMA detector and characterization of an 1800 grooves mm[1] toroidal grating at Stanford. Development of the coma-correcting deformation technique is ongoing, as well as continued testing of the resulting gratings at Padua.

6. ACKNOWLEDGMENTS

C-2

a. Low gas pressure (5 mbar).

b. High gas pressure (30 mbar).

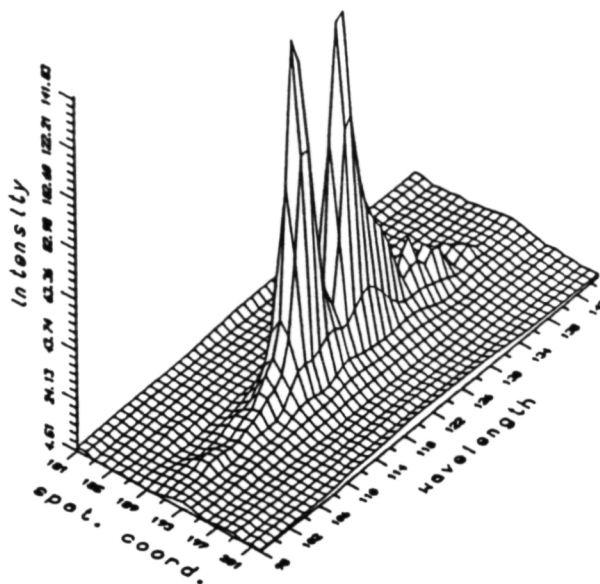**Fig. 21.** Images of a single 25 μm diameter pinhole in the He I 584 Å resonance line. The image demonstrates the spectral and spatial resolution capabilities of the toroidal grating in the EUV

The development of the toroidal gratings has been supported in part by the Ministero Pubblica Istruzione, in part by the Schweizerischer Nationalfonds, and in part by NASA grant NAGW-540. Development of the EUV MAMA detectors is being supported by NASA Contracts NAS5-29389 and NAS5-30387. Development of the HiRES payload is being supported in part by ASI, in part by the Indian Institute of Astrophysics, and inpart by NASA grant NAG5-664.

7. REFERENCES

1. J.G. Timothy *et al.*, "HiRES: A High Resolution Stigmatic EUV Spectroheliometer for Studies of the Fine Structure of the Solar Chromosphere, Transition Region and Corona", *Proc. SPIE X-Ray/EUV Optics for Astronomy, Microscopy, Polarimetry, and Projection Lithography*, vol. 1343, pp. 350-358, 1990.

2. M.C.E. Huber *et al.*, "The Fabrication of toroidal and coma-corrected toroidal diffraction gratings from spherical master gratings using elastically-deformable substrates: a progress report", *Proc. SPIE Space Astronomical Telescopes and Instruments*, vol. 1494, 1991.

3. M.C.E. Huber *et al.*, "Imaging extreme ultraviolet spectrometer employing a single toroidal diffraction grating: the initial evaluation", *Applied Optics*, vol. 27, no.16, pp. 3503-3510, 1988.

4. M.C.E. Huber *et al.*, "Evaluation of toroidal gratings in the EUV", *Proc. SPIE X-Ray Instrumentation in Astronomy II*, Vol. 982, pp. 372-379, 1988.

5. M.C.E. Huber and G. Tondello, "Stigmatic performance of an EUV spectrograph with a single toroidal diffraction grating", *Applied Optics*, vol. 18, no. 23, pp. 3948-3953, 1979.

6. J.G. Timothy, "Imaging pulse-counting detector systems for space ultraviolet astrophysics missions", *Proc.*

SPIE Space Astronomical Telescopes and Instruments, vol. **1494**, 1991.

7. D.C. Slater *et al.*, "Imaging MAMA Detector Systems", *Proc. SPIE Electron Image Tubes and Image Intensifiers*, Vol. **1243** , pp. 35-49, 1990.

8. J.G. Timothy *et al.*, "MAMA Detector Systems: A Status Report", *Proc. SPIE Ultraviolet technology III*, vol. **1158**, pp. 104-117, 1989.

9. Personal Communication.

10. G.H. Mount *et al.*, "Compact far ultraviolet emission source with rich spectral emission 1150-3100 Å", *Applied Optics*, vol. **16**, no. 3, pp. 591-595, 1977.

11. H. Haber, "The Torus Grating", *J. Opt. Soc. Am.*, vol. **40**, no. 3, pp. 153-165, 1950.

12. J. - D.F. Bartoe, Ph.D. Thesis, No. 4602, Georgetown University, 1976, Xerox University Microfilms, Ann Arbor, Michigan 48108.

To Be Published In

The Tenth International Colloquium of UV and X-ray Spectroscopy of Astrophysical and Laboratory Plasmas

Berkeley, California -- February 1992

An Imaging Extreme Ultraviolet Spectrometer

Paolo Bergamini[1], Thomas E. Berger[1], Giorgio Giaretta[1], Martin C.E. Huber[2], Giampiero Naletto[3], J. Gethyn Timothy[1] and Giuseppe Tondello[3]

[1]Centre for Space Science and Astrophysics, Stanford University, ERL 315A Stanford, California 94305-4055 USA
[2]Space Science Department, ESTEC, Postbus 299, 2200AG Noordwijk, The Nethelands
[3]Istituto di Elettronica, Universita' di Padova Via Gradenigo n.6/A, I-35100 Padova, Italy

ABSTRACT

A laboratory extreme ultraviolet (EUV) imaging spectrometer has been fabricated and tested. This instrument is used to test and to characterize toroidal gratings like those which will be employed in the high-resolution spectroheliometer (HiRES) configured for flight on a sounding rocket. The imaging spectrometer will be used also for characterization and calibration of Multi Anode Microchannel Array (MAMA) detectors foreseen on the ESA/NASA Solar Heliospheric Observatory (SOHO) satellite. The spectrometer employs a concave toroidal grating illuminated at normal incidence in a 1 meter Rowland circle mounting: high efficiency is achieved because the grating is the only reflecting surface. The grating is able to produce stigmatic images over a wavelength range of about 100 Å or 200 Å centered respectively around 600 Å or 1200 Å. The source, used to illuminate sets of micron sized pinholes arranged along the spectrometer entrance slit, is a dc hollow cathode lamp: a low-pressure spark-discharge tube operating with noble gases and able to produce sharp spectral lines. The spectra are detected by mean of a MAMA detector which yields high-resolution imaging with great efficiency at EUV wavelengths. The results of the initial imaging tests and the measurements carried out are presented and discussed

1 THE SPECTROMETER

A concave toroidal diffraction grating illuminated in near normal incidence can produce exact stigmatic images in two points of the Rowland circle if the torus vertical and horizontal curvature raddii satisfy the following condition:

$$R_v = R_h \sin \alpha \sin \beta_0 \qquad (1)$$

where α and β_0 are respectively the incidence and diffraction angles (Haber 1950).The two stigmatic points are located symmetrically to the grating normal at $\pm\beta_0$ on the plain that contains the Rowland circle whose diameter is R_h. In systems where β_0 is small there is some depth of focus that enable stigmatic focusing between, and somewhat beyond the two stigmatic points. With a single toroid (moderate speed system with focal ratio $\sim$ f/15) a wavelength range of over 100 Å in the EUV can be obtained with high image quality (Huber and Tondello 1979). The gratings we use have been fabricated using a replica technique with deformable submaster obtained from ruled spherical master (Huber

et al.. 1981). The concave toroidal grating is replicated on a fixed zerodur substrate from the submaster deformed to the appropriate aspect ratio. An osmium coating enhances the EUV reflectivity. The characteristics of the gratings we tested are listed in table 1.

DESIRED CHARACTERISTICS OF THE F/15 TOROIDAL GRATINGS		
Horizontal radius of curvature R_h	1011.1 mm	
Vertical radius of curvature R_v	989.1 mm	
Aspect ratio R_h / R_v	0.9782	
Angle of incidence α	11.947°	
Ruled area	70 x 70 mm^2	
Ruling frequency	3600 grooves mm^{-1}	1800 grooves mm^{-1}
Wavelength at stigmatic points ($\pm\beta_0 = 0.825°$)	535 Å, 615 Å	1070 Å, 1230 Å
Wavelength on grating normal ($\beta = 0$)	575 Å	1150 Å

TABLE 1.

The spectrometer has the entrance slit, the detector and the grating located on a 1-m Rowland circle. The grating is mounted on a plateform that can be moved radially and tangentially for fine focal and spectral adjustments. The source is a DC hollow cathode lamp, a low-pressure spark-discharge tube operated with noble gases. The gas pressure in the lamp (ranging between a few tenths of a torr to a few torr depending on the gas) is maintained against the main chamber vacuum pressure (2-3 x 10^{-7} torr) by a differential pumping system. A set of 10 pinholes (25 μm diameter and 500 μm despaced) in an aluminum foil are located along the entrance slit. We have used the spectrometer with three different toroidal gratings that have the same aspect ratio but different ruling frequency: 3600 mm^{-1} on the first and 1800 mm^{-1} on the second and third. An open-structure MAMA detector is mounted on the output flange of the spectrometer. It is a pulse-counting imaging detector that employs an high gain curved-channel microchannel plate and a readout anode array to produce a format of 1024 x 360 pixels with pixel dimension of 25 x 25 μm^2.

2 TESTS AND RESULTS

The first grating we have mounted and aligned in the spectrometer is the 3600 mm^{-1}. The image of the spectrum produced by the hollow cathode lamp running with a mixture of Helium and Neon (20-80 %) is displayed in the figure (Fig. 1). The source discharge current was 150 mA, the gas pressure 1 torr and the integration time 1000 seconds. The grating's excellent imaging properties are visible in the sharp images of the ten pinholes in every spectral component. Over the whole field of view the pinhole size is no more than 3 pixels FWHM, in both the spectral and spatial direction.

Fig. 1 - Image of the Helium-Neon spectrum obtained with the 3600 mm^{-1} grating. The upper part of the image is fainter because an attenuating mesh is placed in front of the detector microchannel plate. The attenuator transmission coefficient is 10%.
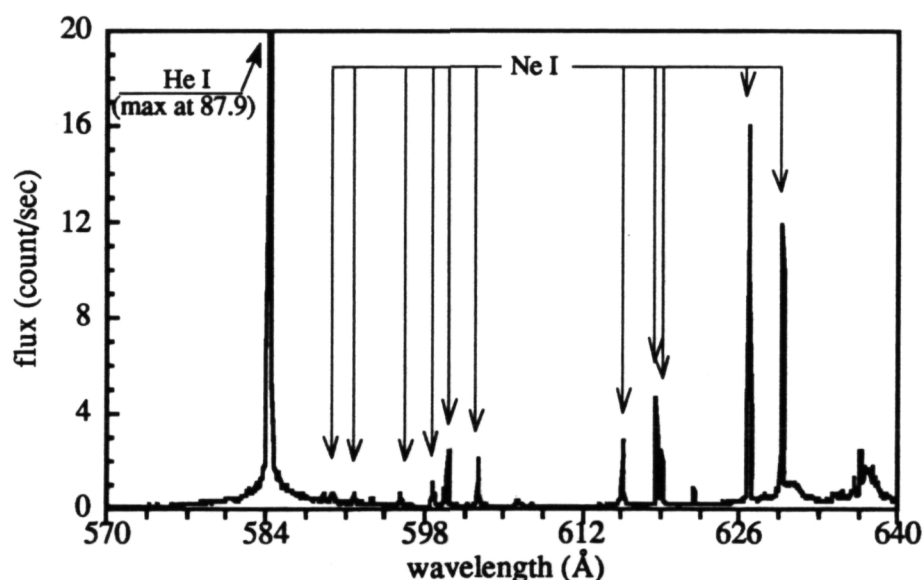
Fig. 2 - Helium-Neon spectrum obtained with the 3600 mm^{-1} grating.

The spectrum in Fig. 2 represent the spectral profile of a single pinhole across the whole detector. The major feature is the first resonance line of He I. Through the identification of the spectral position of 13 lines of Ne I, it was possible to determine the system's linear dispersion scale (0.0693 Å/pixel). The standard deviation of residual of the measured coordinates to the linear least-squares fit result to be 0.27 pixel.

We tested in the spectrometer two 1800 mm^{-1} gratings fabricated from the same ruled master. The first one was tested using pure Argon in the discharge lamp. In the recorded

spectrum, several lines of Ar II, both in 1st and 2nd order, appear beside the principal resonance lines of Ar I (1048.22 Å, 1066.66 Å). The fact that the lamp cathode is copper made explains the presence of the Cu II lines.

The test on the second 1800 mm^{-1} was performed employing the Helium-Neon mixture. Resonance lines, both from the gas and from the cathode material of the spark-discharge lamp, appear also in the spectrum obtained with this grating. The former spectrum covers the second half of the 1800 mm^{-1} grating stigmatic range (1120-1270 Å) while the Argon spectrum (990-1130 Å) covers the first half.
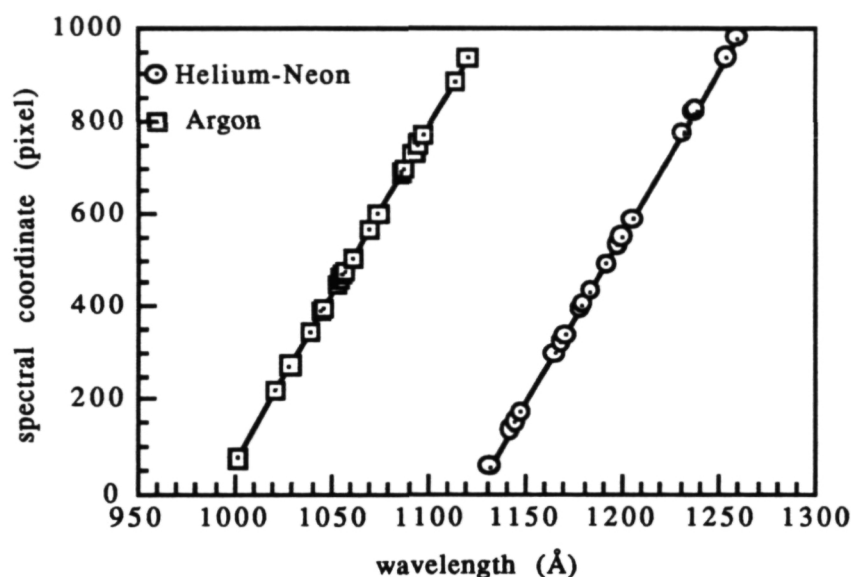
Fig. 3

In Fig. 3 the coordinate of identified lines of the spectra obtained with the two 1800 mm^{-1} are plotted with the linear least-squares fit to the data. For both the gratings the resulting linear dispersion scale is 0.1385 Å pixel^{-1} and the peak to peak departures of data from the fitted linear dispersion scale is within 1.8 pixels.

REFERENCES

Berger, T. E., *et al*, 1991, *Proc. SPIE Multilayer and Grazing Incidence X-Ray/EUV Optics*, **1546**, 446.

Haber, H. 1950, *Appl. Opt.*, **40**, 153.

Huber, M. C. E., and Tondello, G. 1979, *Appl. Opt.*, **18**, 3948.

Huber, M. C. E., Janniti, E., Lemaitre, G., and Tondello, G. 1981, *Appl. Opt.*, **20**, 2139.

To Be Published In

The Tenth International Colloquium of UV and X-ray Spectroscopy of Astrophysical and Laboratory Plasmas

Berkeley, California -- February 1992

HiRES: High Resolution Extreme Ultraviolet Spectroheliometer

Thomas Berger[1], Paolo Bergamini[1], Helen Kirby[1], J. Gethyn Timothy[1], Arthur B.C. Walker[1], Jagadish C. Bhattacharyya[2], Surendra K. Jain[2], Ajay K. Saxena[2], Martin C.E. Huber[3], Giampiero Naletto[4], Guiseppe Tondello[4]

[1]Center for Space Science and Astrophysics, Stanford University
[2]Indian Institute of Astrophysics
[3]Space Science Department, European Space Agency
[4]Istituto di Elettronica, University of Padua

ABSTRACT

The HiRES sounding rocket payload is designed to obtain very high spatial, spectral, and temporal resolution images of the solar chromospheric and coronal plasmas in the extreme ultraviolet (EUV) wavelength range from 500 to 650 Å. The instrument consists of a 450 mm f/15 Gregorian telescope feeding a 1-m normal incidence stigmatic spectrometer. The stigmatic spectrometer utilizes a toroidal diffraction grating formed by a unique elastic substrate deformation technique in order to achieve simultaneous spatial and spectral focusing at two points on the detector plane. Spatial resolution on the order of 0.4 arcsecond across a 3 x 3 arcmin^2 field of view is obtained. Temporal resolution of the order of milliseconds is achieved by the use of an advanced imaging Multi-Anode Microchannel Array (MAMA) detector. A hydrogen-alpha 6562.8 Å camera and a 0.25-m EUV solar irradiance spectrometer are also included in the payload.

1 INTRODUCTION

Recent high resolution sounding rocket instruments such as the High Resolution Telescope and Spectrograph (HRTS) in near-ultraviolet wavelengths [Brueckner, 1983] and the Multi-Spectral Solar Telescope Array (MSSTA) [Walker, 1988] and the Normal Incidence X-ray Telescope (NIXT) [Golub, 1990] in the soft x-ray regime have pushed the spatial resolution of solar observations towards the sub-arcsecond level and revealed coherent small scale structures in all wavelengths imaged. The improvements offered by these instruments in both spatial and spectral resolution have provided a better understanding of the structure of the chromosphere and corona and the role of the time-dependent magnetic field in the dynamics of these regions. The HiRES instrument will fill a gap in the wavelength coverage of high resolution observations by adding sub-arcsecond imaging and radiometric data in the extreme ultraviolet wavelength range between 500 and 650 Å.

Resolution values for the HiRES instrument are as follows:

- Spatial resolution: 0.4 arcseconds
- Spectral resolution: $\lambda/\Delta\lambda = 10,000$ (0.078 Å)
- Temporal resolution: 10^{-3} sec (depending on signal levels)

Stigmatic points are located at 535 Å and 615 Å with near stigmatic imaging in between and slightly beyond these wavelengths. The MAMA detector has a nominal 360 by 1024 25 micron pixel format with integrated decode circuitry capable of centroiding the photon events to within 0.1 pixel resulting in a spectral shift sensitivity of approximately 2 mÅ (~1 km per second Doppler shifts at 600 Å). The MAMA detector uses a single curved-channel microchannel plate (MCP) for high geometric fidelity and minimal ion feedback. The spectrometer is calibrated in flight by a sealed platinum hollow cathode lamp.

The HiRES payload includes two ancillary instruments. The first is a hydrogen Balmer-alpha (6562.8 Å) CCD camera that performs real-time monitoring of instrument pointing and target selection. The second is a 0.25 meter spherical grating objectiveless spectrometer for full Sun irradiance measurements in the wavelength range of 280 Å to 1270 Å. Provision for later inclusion of a Wadsworth infrared spectrometer for simultaneous helium 10830 Å observations is built into the HiRES instrument.

Table 1 lists the dominant solar spectral emission lines in the HiRES EUV wavelength range.

Table 1 - Major Solar Emission Lines Visible to HiRES

ION	λ Å	TEMP (K)	ACTIVE INTENSITY (erg cm^{-2}s^{-1}sr^{-1})	COUNT RATE (Pixel^{-1} sec^{-1})	QUIET INTENSITY (erg cm^{-2}s^{-1}sr^{-1})	COUNT RATE (Pixel^{-1} sec^{-1})
Si XII	499.0	2.0×10^6	1284	363	66	19
He I	515.6	3.2×10^4	199	56	26	7
Si XII	521.1	2.0×10^6	720	213	33	10
He I	522.2	3.2×10^4	329	98	44	13
He I	537.3	3.2×10^4	834	253	109	33
Al XI	550.0	NA	169	48	9	3
O IV	553.7	1.6×10^5	487	138	246	70
Fe XV	568.3*	4.0×10^6	4733	76	NA	NA
He I	584.3	3.2×10^4	7200	2388	828	275
O III	599.6	1.0×10^5	74	25	43	15
Si XI	606.6*	1.6×10^6	16955	292	3049	52
He II	607.6*	8.0×10^4	91752	1582	10998	190
Mg X	609.8	1.0×10^6	943	327	136	47
Mg X	625.2	1.0×10^6	470	167	49	17
O V	629.7	2.5×10^5	1334	465	510	178

* Observed wavelength in second order. Intensity values from [Vernazza, 1978]

2 INSTRUMENT DESCRIPTION

The HiRES instrument design is based on two key technologies: the fabrication of replicated toroidal diffraction gratings using deformable master substrates [Huber 1979, 1991] and the Multi-Anode Microchannel Array (MAMA) detector [Timothy 1989, 1991a]. A single toroidal grating produces stigmatic images which allows high-resolution imaging in the EUV by eliminating the reflectivity losses associated with multi-optic spectrometer designs. The deformable substrate fabrication method results in a significant saving of manufacturing and testing time as compared to the traditional grinding and polishing technique. The MAMA detector system to be used on the HiRES instrument is of the same design that is currently being developed for use on the ESA/NASA Solar and Heliospheric Observatory (SOHO) satellite. MAMA detectors are also being developed for the Space Telescope Imaging Spectrograph (STIS) and the Far Ultraviolet Spectroscopic Explorer (FUSE/*Lyman*) mission. The MAMA detector gives the HiRES instrument the ability to image faint, multi-spectral EUV solar features with radiometric accuracy; to image with extremely high temporal resolution; and to transmit and store the data electronically.

The instrument platform is a 22" diameter Black Brant sounding rocket. The primary elements of the instrument are a 450 mm f/15 Gregorian telescope, a 1 meter toroidal grating spectrograph, and the MAMA detector. Figure 1 shows a layout of the HiRES payload.
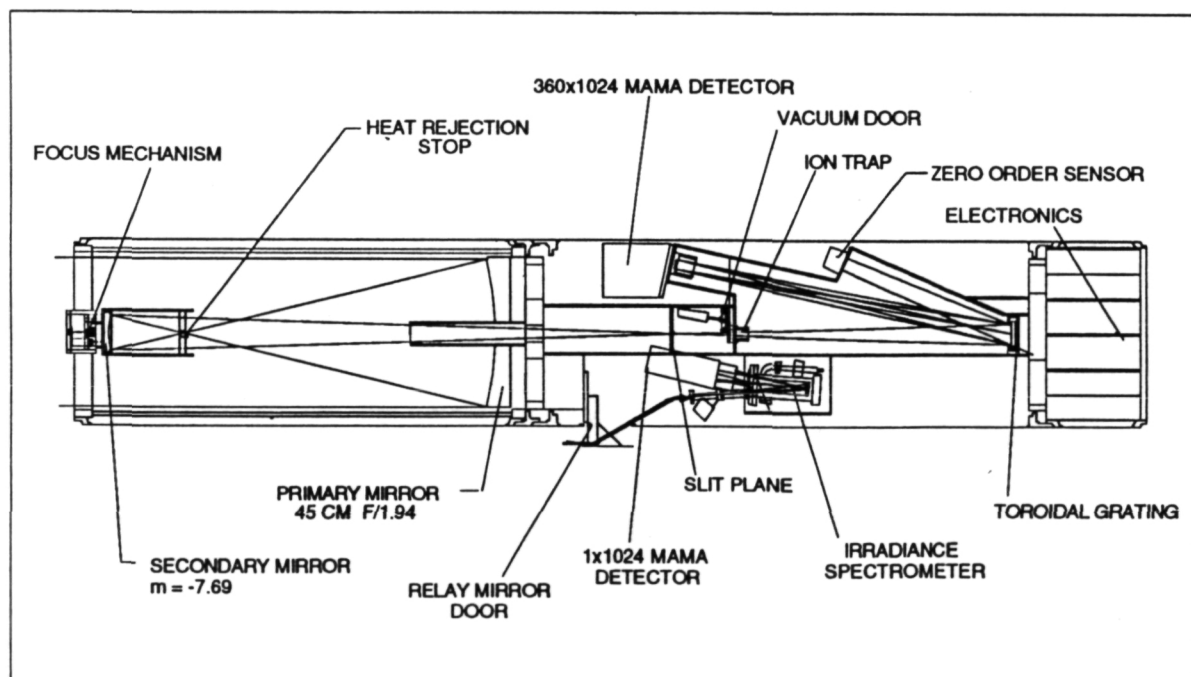

Figure 1 - Conceptual Layout of the HiRES payload

The HiRES instrument has two observing modes: a stationary slit mode in which the field of view is limited to the 0.4 arcsecond by 3 arcminute slit extent, and a spatial scan mode in which the sounding rocket control system is used to scan the slit across the field of view. In the stationary slit mode, the instrument collects high time resolution slit images analogous to the HRTS images. These observations are ideal for high time resolution studies of very small scale transient events such as microflares. The scan mode builds two-dimensional images perpendicular to the slit axis by scanning the slit across areas of interest on the Sun. Figure 2 is a scaled diagram of the HiRES scan mode field of view on the Sun. Each emission line in the HiRES spectral range is built into a composite image with temporal resolution limited by the scan time of 45 seconds. These images are useful for studying the morphology of the solar coronal plasmas in the distinct temperatures ranges of the ions listed in Table 1. More detailed descriptions of the HiRES instrument exist elsewhere in the literature [Timothy, 1991b; Berger, 1991].
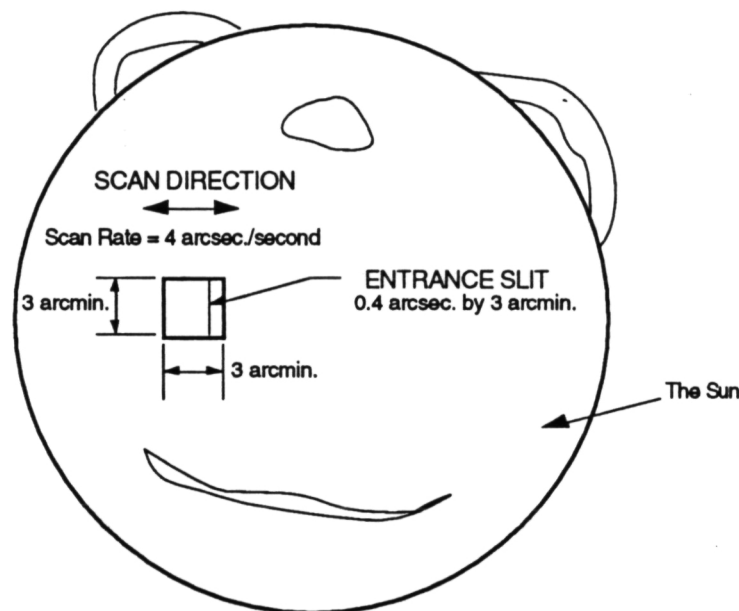

Figure 2 - Typical HiRES Image Scan

3 REFERENCES

Berger, T.E., *et al.*, 1991, *Proc. SPIE*, **1546**, 446.
Brueckner, G. and J.-D.F. Bartoe, 1983, *Ap. J.*, **272**, no. 1, 329.
Golub, L. , *et al.*, 1990, *Nature*, **344**, 842.
Huber, M.C.E. and G. Tondello, 1979, *Applied Optics*, **18**, no. 23, 3948.
Huber , M.C.E., *et al.*, 1991, *Proc. SPIE*, **1494**, 472.
Timothy, J.G., *et al.*, 1989, *Proc. SPIE*, **1158**, 104.
Timothy, J.G., *et al.*, 1991a, *Proc. SPIE*, **1494**, 394.
Timothy, J.G., *et al.*, 1991b, *Optical Eng.*, **30**, no. 8, 1142.
Vernazza, J.E. and E.M. Reeves, 1978, *Ap. J. Supp.*, **37**, 485.
Walker, A.B.C., *et al.*, 1988, *Science*, **241**, 1781.